Magnetic Field Determination for Run 1 of the Fermilab Muon $g-2$ Experiment

Rachel Osofsky

A dissertation
submitted in partial fulfillment of the
requirements for the degree of

Doctor of Philosophy

University of Washington

2019

Reading Committee:

Alejandro García, Chair

David Hertzog

Subhadeep Gupta

Program Authorized to Offer Degree:
Physics

University of Washington

Abstract

Magnetic Field Determination for Run 1 of the Fermilab Muon $g-2$ Experiment

Rachel Osofsky

Chair of the Supervisory Committee:
Professor Alejandro García
Physics

The muon $g-2$ experiment at Fermilab aims to measure the anomalous magnetic moment of the muon, a_μ, to a precision of 140 parts per billion (ppb). The measurement will shed light on the current $>3\sigma$ deviation between Standard Model calculations and the previous measurement made at Brookhaven National Laboratory, either resolving the discrepancy or confirming it to $>5\sigma$. In the muon $g-2$ experiment, muons are stored in a magnetic storage ring and their decays are observed. In order to reach the precision goal, the magnetic field experienced by the muons must be known with an uncertainty of 70 ppb or less. To this end, the magnetic field was shimmed to unprecedented homogeneity. Two measurement systems are used to track the evolution of the magnetic field. This dissertation describes the motivations for the $g-2$ experiment, gives a brief overview of the experimental principles, introduces the magnetic field measurement hardware, describes the magnetic field shimming process, and presents an analysis of the magnetic field tracking for data collected in spring 2018 during run 1 of the Fermilab muon $g-2$ experiment.

TABLE OF CONTENTS

LIST OF FIGURES

LIST OF TABLES

ACKNOWLEDGMENTS

Many people have contributed to making me both the person and the scientist I am today, and to the work reported on in this dissertation. First, I would like to thank my advisor and close mentors at the University of Washington: Alejandro García, Erik Swanson, and Martin Fertl. The start my graduate research career would not have been as positive as it was without the presence of Matthias Smith, who patiently worked with me and answered all of my many questions. I would also like to thank the remainder of the UW $g-2$ group, who were always available for conversations and to answer questions. I will look back fondly on the friendships we've formed over the hundreds of hours we've spent together.

Throughout my graduate career, I made many long trips to work on site at Fermilab. Brendan Kiburg acted as my onsite mentor. Without his guidance, the work reported herein would have suffered. I am immensely grateful for all of the time he spent with me, talking through problems both big and small, and offering advice and support. I would also like to thank the remaining members of the Bloch interpolation team: Jason Bono, Jimin George, and Saskia Charity. These three collaborators learned the intricate details of my analysis and helped carry out many systematic studies. None of my analysis would have been possible without the analysis framework that David Flay helped me build. All of these people have become personal friends who have enhanced my life.

The entire Fermilab muon $g-2$ collaboration has welcomed me with open arms, allowing me to make important contributions to the success of the experiment, in addition to teaching me more than I probably even realize. The past six years would not have been nearly as enjoyable without this group of people in my life.

I would like to thank Alaina Green, Tong Wan, and Sarah Carter for being the best

housemates I could have asked for, as well as the rest of my friends for all of their support during my graduate school career. Finally, I would like to thank my family, without whose love and support I would not be where I am today.

DEDICATION

To my mom, Suzy Silverstein.

Chapter 1

INTRODUCTION

Physicists strive to understand the world around us. In particular, the standard model of particle physics is a theory which describes the elementary particles which make up our universe, in addition to the four known fundamental forces. To test the validity of the standard model, experimental measurements are compared to theoretical calculations. One of the most stringent tests involves the comparison of the experimentally measured and theoretically calculated values of the anomalous magnetic moment of the muon, $a_\mu \equiv \frac{g_\mu - 2}{2}$.

Measuring the muon's anomalous magnetic moment requires precision measurements of both a spin precession frequency and a magnetic field. This document describes the E989 Muon $g-2$ Experiment at Fermilab, with a particular emphasis on the magnetic field measurement. The work described in this dissertation concentrates on areas in which the author has made significant contributions, with references to work on other parts of the experiment provided throughout for the interested reader.

Chapter 1 provides an introduction to magnetic moments, spin precession, and muons. It also presents previous muon $g-2$ measurements and provides an introduction to the theoretical calculations of a_μ. Chapter 2 presents the E989 experimental principles, while chapter 3 provides details on the magnetic field measurement hardware. Chapter 4 discusses the process of making the magnetic field homogeneous, while chapter 5 details the measurement of radial and longitudinal magnetic field components. Finally, chapter 6 discusses magnetic field tracking while chapter 7 provides conclusions and an outlook for the future.

1.1 Magnetic Moments and Spin Precession

The magnetic moment of a particle characterizes how it interacts with external magnetic fields. Borrowing the notation and introduction to the topic from [1], the basic laws of magnetostatics read

$$\begin{aligned} \vec{\nabla} \times \vec{B} &= \mu_0 \vec{J} \\ \vec{\nabla} \cdot \vec{B} &= 0, \end{aligned} \tag{1.1}$$

where $\vec{B}$ is a magnetic field, μ_0 is the permeability of free space, and $\vec{J}$ is a current density. One way to solve these equations is to note that with the divergence of $\vec{B}$ disappearing everywhere, the magnetic field can be described as the curl of a vector potential, $\vec{B} = \vec{\nabla} \times \vec{A}\,(\vec{x})$. The general form of the vector potential can be written as [1]

$$\vec{A}\,(\vec{x}) = \frac{\mu_0}{4\pi} \int \frac{\vec{J}\,(\vec{x})}{|\vec{x} - \vec{x}'|} d^3x'. \tag{1.2}$$

With $\vec{J}$ a localized, divergenceless current distribution, [1] shows that the vector potential of Eq. 1.2 can be approximated by

$$\vec{A}\,(\vec{x}) = \frac{\mu_0}{4\pi} \frac{\vec{\mu} \times \vec{x}}{|\vec{x}|^3}, \tag{1.3}$$

where $\vec{\mu}$ is known as the magnetic moment. Far away from a localized current distribution, the observed magnetic field can be calculated as that produced by the vector potential of a magnetic dipole, Eq. 1.3, with the magnetic moment related to the current distribution as

$$\vec{\mu} = \frac{1}{2} \int \vec{x}' \times \vec{J}\,(\vec{x}')\, d^3x'. \tag{1.4}$$

For a current distribution created by a collection of charged particles with total charge Q and total mass M, the magnetic moment can be written as

$$\vec{\mu} = \frac{Q}{2M} \vec{L}, \tag{1.5}$$

where $\vec{L}$ is the total orbital angular momentum of the group of charged particles [1].

While a magnetic dipole creates a magnetic field, it also experiences a force when placed in an external magnetic field:

$$\vec{F} = \vec{\nabla}\left(\vec{\mu}\cdot\vec{B}\right). \tag{1.6}$$

Interpreting this force as the negative gradient of a potential energy, a magnetic dipole in the presence of an external magnetic field has a potential energy given by [1]

$$U = -\vec{\mu}\cdot\vec{B}. \tag{1.7}$$

To minimize potential energy, magnetic dipole moments tend to align with an external magnetic field, a property which is exploited for the magnetic field measurement of the $g-2$ experiment.

In addition to alignment in an external magnetic field, particles with spin will also precess in a magnetic field. Borrowing the notation and introduction to spin precession from [2], the spin and magnetic moment of a particle are related as

$$\vec{\mu} = \gamma\vec{S}, \tag{1.8}$$

where γ is known as the gyromagnetic ratio. The Hamiltonian of such a particle in an external magnetic field is given by

$$H = -\gamma\vec{S}\cdot\vec{B}. \tag{1.9}$$

Information about the time evolution of such a system (with $t_0 = 0$) is given by the time evolution operator [2]

$$\mathscr{U}(t) = exp\left(\frac{i\gamma S_z B t}{\hbar}\right), \tag{1.10}$$

where the magnetic field has been arbitrarily chosen to point in the $\hat{z}$ direction. This can be interpreted as the rotation of the spin about the axis of the external magnetic field at a frequency given by

$$\omega = \gamma B. \tag{1.11}$$

The rotation of a spin about an external magnetic field is known as spin precession, and this phenomenon is the basis of both of the precision measurements carried out in the E989 experiment.

Reality however is not so simple. Experimental observations show that Eq. 1.5 does not accurately describe the behavior of the simplest spin-1/2 particles, such as protons, electrons, and muons. Instead, a dimensionless scaling factor, known as the g-factor, must be included

$$\vec{\mu} = \pm g \frac{e}{2m} \vec{S}, \tag{1.12}$$

where e and m are the elementary charge and particle mass. The electron and muon g-factors are both approximately 2, while the proton g-factor is approximately 5.6 [3].

In 1925, Uhlenbeck and Goudsmit proposed the idea of particle spin to explain the fine structure observed in the anomalous Zeeman effect [4]. In 1926, they concluded that the g-factor for spin is twice that for orbital angular momentum [5]. In 1928, Paul Dirac published *The Quantum Theory of the Electron* in which he introduced a relativistic wave equation for the electron [6]. In discussing the effects of an external magnetic field on an electron, he derived $g_e = 2$, explaining the previous experimental observations. Later experiments showed that $g_p \approx 5.6$ and that the neutron has a large magnetic moment, leading to the convention of breaking the magnetic moment into 2 pieces:

$$\begin{aligned} \mu &= (1+a)\frac{q\hbar}{2m} \\ a &= \frac{g-2}{2}, \end{aligned} \tag{1.13}$$

where a is known as the anomalous magnetic moment. The first term is predicted by the Dirac equation and is therefore known as the Dirac moment [7].

The anomalous magnetic moment of a particle is a property which can both be calculated with high precision using the standard model and can also be measured with comparably high precision for certain particles. a_e, the anomalous magnetic moment of the electron, has been measured to 0.28 parts per trillion [8]. The anomalous magnetic moment of the muon, a_μ, has most recently been measured at Brookhaven National Laboratory by the E821

collaboration [9] to 540 parts per billion (ppb), and is currently being re-measured at Fermi National Accelerator Laboratory (Fermilab) by the E989 collaboration with a precision goal of 140 ppb [10].

1.2 A Brief Introduction to Muons

One of three known charged leptons, muons are typically thought of as heavy electrons. With the same charge and spin, the largest differences between muons and electrons are that muons are approximately 200 times more massive and have a much shorter lifetime ($\sim 2.197 \times 10^{-6}$ seconds, as compared to $> 6.6 \times 10^{28}$ years [11]).

The dominant decay channels for pions and muons are given by:

$$\begin{aligned} \pi^+ &\to \mu^+ \nu_\mu \\ \pi^- &\to \mu^- \bar{\nu}_\mu \\ \mu^+ &\to e^+ \nu_e \bar{\nu}_\mu \\ \mu^- &\to e^- \bar{\nu}_e \nu_\mu. \end{aligned} \tag{1.14}$$

Muon beams are typically produced via pion decay, with pion decay leading to a muon with a branching fraction of 99.9877%. Muons then decay to electrons/positrons with a nearly 100% branching fraction [11].

1.2.1 Pion Decay

From Eq. 1.14, pion decay leads to the production of a muon and a muon neutrino, with very high likelihood. The next most likely decay channel produces an electron and an electron neutrino. Charged pions have zero spin, so due to spin and momentum conservation, the resultant muon and neutrino must therefore be emitted with opposite spin and momentum.

In positive pion decay, which produces a positively charged muon and a muon neutrino, the neutrino is left-handed. Conservation of angular momentum implies that the muon has the same handedness. In this decay, both particles have their spin and momentum in opposite directions. In negative pion decay, the antineutrino and negatively charged muon

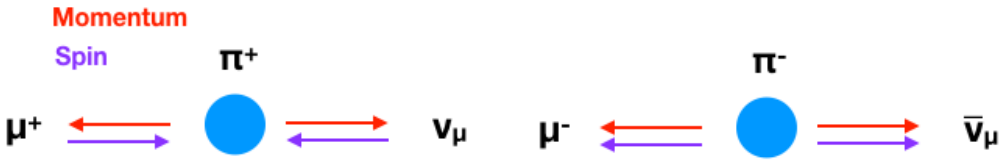

Figure 1.1 – Pion decay is governed by the weak interaction, with the decay producing a muon and muon neutrino with a greater than 99% branching fraction. In positive pion decay, the produced particles both have their spin (purple) and momentum (red) in opposite directions. In negative pion decay, the produced muon and muon antineutrino have spin and momentum in the same direction.

are both right-handed, with each having their spin and momentum in the same direction [12]. Fig. 1.1 summarizes the momentum and spin directions in both positive and negative pion decay. The $g-2$ experiment uses a polarized, positive muon beam, where here polarization refers to spin being in the opposite direction as the momentum vector.

1.2.2 Muon Decay

The three-body muon decay is more complicated than the two-body pion decay. With a nearly 100% branching fraction, positive muon decay produces a positron and two neutrinos[1], with the decay being self-analyzing: the parity-violating correlation between the spin and momentum of the produced decay particles provides information on the muon spin orientation at the time of decay [13].

In muon decay, the produced positron can be emitted with an energy up to half of the muon rest mass energy, depending on the energy imparted to the neutrinos. When the neutrino and antineutrino are produced with momenta in the same direction, antiparallel to the positron direction, the positron is emitted with the maximum possible energy,

[1]Negative muon decay produces an electron and two neutrinos.

$E_{max} = m_\mu c^2/2$=52.8 MeV/c^2. In this situation, the neutrino-antineutrino pair carries no total angular momentum. Conservation of angular momentum then requires that the positron's angular momentum be equal to that of the muon. The positron is preferentially emitted right-handed, with a larger probability of its momentum being parallel to the muon spin in the muon rest frame[2]. In the case where the neutrino and antineutrino are produced with momenta in opposite directions, the pair carries a net angular momentum of 1, while the low energy positron is preferentially produced with momentum anti-parallel to that of the muon spin [13].

In the muon rest frame the differential decay distribution is given by

$$\frac{dP(y,\theta^*)}{dyd\Omega} = (1/2\pi)n^*(y)\,(1-\alpha^*(y)cos\theta^*)\,, \tag{1.15}$$

where an asterisk represents the muon rest frame, $y = E^*/E_{max}$ is the normalized electron energy (E_{max} =52.8 MeV/c^2), and θ^* is the angle of the decay electron with respect to the muon spin. $n^*(y)$ is the number distribution, given by Eq. 1.16, while $\alpha^*(y)$ is known as the asymmetry function and is given by Eq. 1.17 [14]:

$$n^*(y) = y^2(3-2y) \tag{1.16}$$

$$\alpha^*(y) = \frac{q}{e}\frac{2y-1}{3-2y}. \tag{1.17}$$

The asymmetry function encodes the strength of the correlation between the electron momentum and muon spin as a function of electron energy. Electrons with $y < 0.5$ are preferentially emitted along the negative muon spin direction (negative asymmetry), while electrons with $y > 0.5$ are preferentially emitted in the opposite direction (increasing, positive asymmetry). The number distribution also increases with increasing energy. The asymmetry and number distributions are shown in Fig. 1.2a. The distributions boosted into the lab frame ($n^* \to N$ and $\alpha^* \to A$) are shown in Fig. 1.2b at the muon momentum of 3.094 GeV/c used in

[2]In negative muon decay, the electron is preferentially emitted left-handed, with its momentum anti-parallel to the muon spin.

the $g-2$ experiment. The boosted product NA^2 is inversely proportional to the statistical uncertainty of the $g-2$ anomalous precession frequency measurement [9].

1.3 Previous $(g-2)_\mu$ Measurements

The Fermilab $g-2$ experiment builds upon other experiments which measured the anomalous magnetic moment of the muon. More specifically, it builds upon three experiments undertaken at CERN, and one at Brookhaven national laboratory (the E821 muon $g-2$ experiment). Details of the previous experiments can be found in [9, 15], with a short summary provided here.

The first muon $g-2$ experiment at CERN ran from 1958-1962 and provided the result

$$a_\mu = (1162 \pm 5) \times 10^{-6} \tag{1.18}$$

with a 0.4% uncertainty. The result agreed with theoretical calculations at the time, within experimental errors, and was taken as evidence that the muon behaved just like a heavy electron, providing little insight into new physics [15].

The next generation experiment, the CERN II experiment, ran from 1962-1968. It represents the first use of a magnetic storage ring in a muon $g-2$ experiment. In a magnetic storage ring, the cyclotron and spin frequencies, ω_c and ω_s respectively, precess at different rates for particles with $g \neq 2$, as shown in Fig. 1.3. The frequencies are given by

$$\begin{aligned} \vec{\omega}_c &= -\frac{q\vec{B}}{m\gamma} \\ \vec{\omega}_s &= \frac{gq\vec{B}}{2m} - (1-\gamma)\frac{q\vec{B}}{\gamma m}, \end{aligned} \tag{1.19}$$

where $\vec{B}$ is the magnetic field and γ is the Lorentz factor. Their difference, the anomalous precession frequency, is given by

$$\vec{\omega}_a = \vec{\omega}_a - \vec{\omega}_c = -\left(\frac{g-2}{2}\right)\frac{q\vec{B}}{m} = -a_\mu \frac{q\vec{B}}{m}, \tag{1.20}$$

allowing a_μ to be extracted if the magnetic field is well known [9]. Note however that if $g = 2$, the anomalous precession frequency would be zero. This measurement principle is sensitive to differences of g from 2, as opposed to measuring g itself.

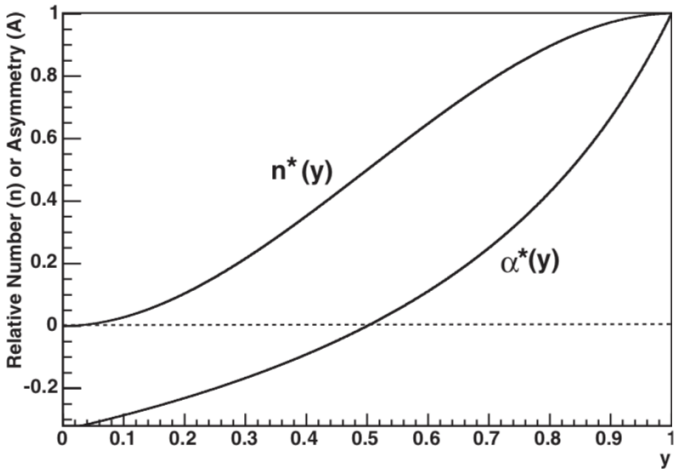

(a) Muon rest frame.

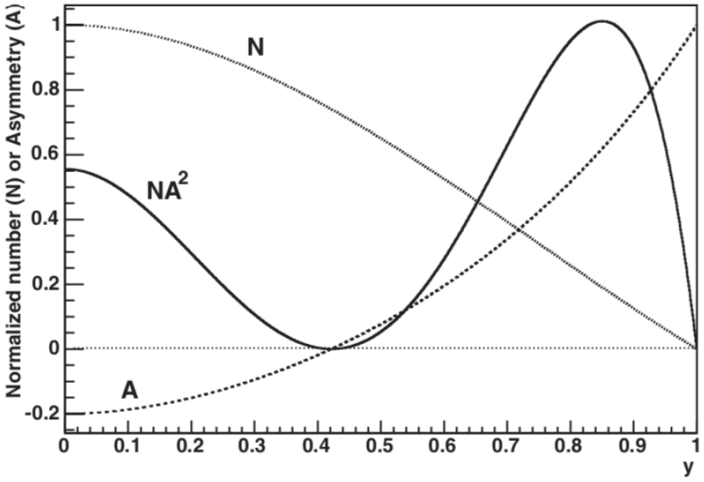

(b) Boosted lab frame.

Figure 1.2 – The number distribution and asymmetry function of electrons produced by muon decay are shown as function of the normalized electron energy, $y = E/E_{max}$, in both the muon rest frame and the boosted lab frame. The boosted product NA^2 is inversely proportional to the statistical uncertainty of the $g - 2$ anomalous precession frequency measurement. Image credit: [9]

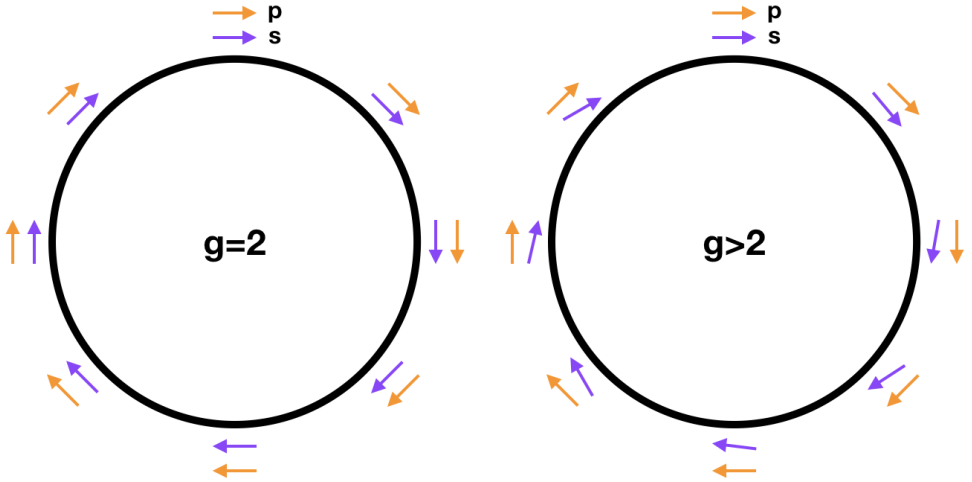

Figure 1.3 – In a magnetic storage ring, the cyclotron (orange) and spin (purple) precession frequencies of muons precess at different rates for particles with $g \neq 2$. By measuring the difference of these frequencies, the anomalous precession frequency, the anomalous magnetic moment can be extracted.

The CERN II experiment gave the result

$$a_\mu = (116616 \pm 31) \times 10^{-8} \tag{1.21}$$

with a 270 ppm precision. The biggest sources of uncertainty were the magnetic field distribution and the radial distribution of stored muons. This result again agreed with theoretical calculations of a_μ within experimental uncertainty [15].

By 1969, many experiments had shown that the muon obeys Fermi-Dirac statistics, but pure quantum effects were not as well understood. In particular, experiments measuring the Lamb shift in atomic Hydrogen disagreed with theory. As the theoretical predictions improved, the difference between experimental and theoretical values for a_μ started to grow, prompting a third CERN experiment [15].

The magnetic storage ring of the second experiment inspired the third experiment, but the idea was improved in many ways. The new storage ring used a ring magnet with a

uniform magnetic field. Vertical focusing was provided by electric quadrupoles, whose electric field was seen by muons as a motional magnetic field that could affect the spin precession frequency [15]. With both electric and magnetic fields present, the anomalous precession frequency becomes

$$\vec{\omega}_a = -\frac{q}{m}\left[a_\mu \vec{B} - \left(a_\mu - \frac{1}{\gamma^2 - 1}\right)\frac{\vec{\beta}\times\vec{E}}{c}\right], \tag{1.22}$$

which can be compared to Eq. 1.20. Using the "magic momentum" of 3.094 GeV/c, or $\gamma \approx 29.3$, the coefficient of the electric field term vanishes, separating the functions of the fields: the magnetic field determines the muon spin precession while the electric field provides vertical focusing, necessary to keep the muon beam stored within the magnet [9, 10]. The CERN III experiment achieved a result of

$$a_\mu = 1165923(8.4) \times 10^{-9} \tag{1.23}$$

with a precision of 7 ppm, which was, again, in good agreement with theory[15, 16].

After completion of the third CERN experiment, theoretical efforts to calculate a_μ continued. In 1984, theorists began pressing for an improved measurement, the Brookhaven National Laboratory (BNL) E821 experiment. Like the CERN III experiment, the BNL experiment used a magnetic storage ring with a uniform magnetic field and electric focusing. The decays of magic momentum muons were measured.

The other experimental principles of the BNL experiment are very similar to those of the Fermilab experiment, and will be discussed in Ch. 2. The final BNL result, calculated using nearly equal amounts of positive and negative muon data, is

$$a_\mu(\text{exp}) = \frac{1}{2}(g_\mu - 2) = 11659208.0(6.3) \times 10^{-10}, \tag{1.24}$$

a 540 ppb measurement [9]. A comparison of this measurement with the most up-to-date theoretical calculations is presented in Sec. 1.5.

1.4 $(g-2)_\mu$ in the Standard Model

Standard model calculations of the anomalous magnetic moment of the muon get contributions from three sources:

$$a_\mu^{SM} = a_\mu^{QED} + a_\mu^{EW} + a_\mu^{Had}. \tag{1.25}$$

These represent contributions from quantum electrodynamics, electroweak interactions, and hadronic interactions. The hadronic contribution is further split into contributions from both hadronic vacuum polarization and hadronic light-by-light scattering [17, 18]:

$$a_\mu^{Had} = a_\mu^{Had,VP} + a_\mu^{Had,LbL}. \tag{1.26}$$

Each contribution to the standard model value comes with its own uncertainty. Calculations of the contributions and uncertainties from each of these components are discussed in the following sections.

1.4.1 Quantum Electrodynamics Contributions

The quantum electrodynamics contribution to a_μ^{SM} comes from Feynman diagrams involving photons and leptons. It can be expressed as a perturbative expansion in α, the fine structure constant [19]:

$$a_\mu^{QED} = \sum_{n=1}^{\infty} \left(\frac{\alpha}{\pi}\right)^n a_\mu^{(2n)}. \tag{1.27}$$

The first order term is the Schwinger term, with $a_\mu^{(2)} = \frac{1}{2}$ leading to $\frac{\alpha}{2\pi}$. Higher order contributions, up to $a_\mu^{(10)}$, have been calculated by Aoyama et al. [19, 20]. They calculated the contributions from over 10,000 Feynman diagrams, a small selection of which are shown in Fig. 1.4.

In order to calculate a value of a_μ^{QED}, a value for α must be chosen. Aoyama et al. [19] provide two values, one using α as derived from measurements and theoretical calculations of a_e, the anomalous magnetic moment of the electron, and another using α as obtained from

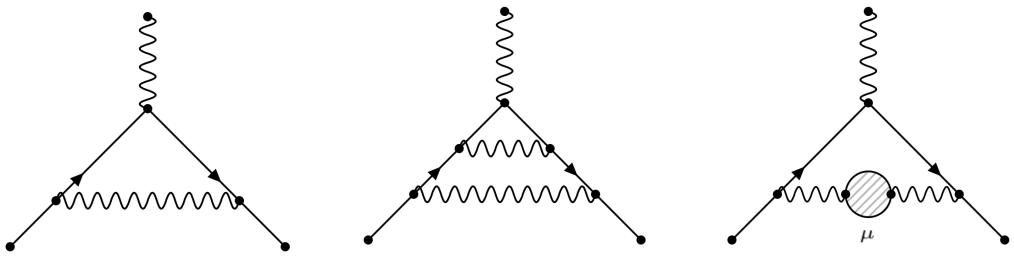

(a) One loop QED diagram. (b) Two loop QED diagrams.

Figure 1.4 – QED contributions to a_μ^{SM} come from Feynman diagrams containing photons and leptons. Pictured are the one loop diagram contribution (the Schwinger term) and example two-loop diagrams.

measurements of the recoil velocity of Rb atoms [21]:

$$\begin{aligned} \alpha^{-1}(a_e) &= 137.0359991736(0.25\,\text{ppb}) \\ \alpha^{-1}(\text{Rb}) &= 137.035999049(0.66\,\text{ppb}). \end{aligned} \tag{1.28}$$

Parker et al. [22] have also measured α using the recoil of cesium atoms in a matter-wave interferometer:

$$\alpha^{-1}(\text{Cs}) = 137.035999046(0.20\,\text{ppb}). \tag{1.29}$$

Because theoretical calculations of a_e and a_μ are highly correlated, it is preferable to use the value derived from either the Rb or Cs measurements. Aoyama et al. report a QED contribution of

$$a_\mu(QED, Rb) = (11658471.8951 \pm 0.008) \times 10^{-10}, \tag{1.30}$$

where the main sources of uncertainty are the lepton mass ratios, the eighth-order contribution, the tenth-order contribution, and the value of α [19]. This term accounts for over 99% of a_μ^{SM}, with a negligible contribution to the overall uncertainty.

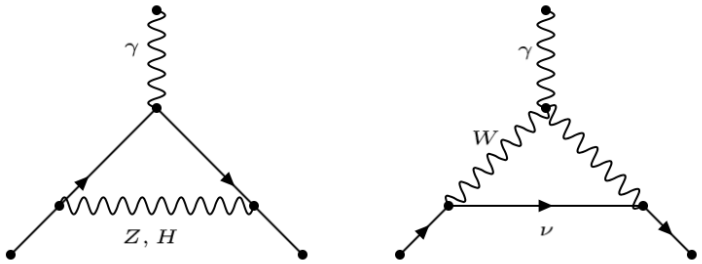

Figure 1.5 – The leading order electroweak Feynman diagrams which contribute to a_μ^{SM}. The diagrams involve W/Z bosons and the Higgs particle.

1.4.2 Electroweak Contributions

Electroweak contributions to a_μ^{SM} come from Feynman diagrams which include a W or Z boson, or a Higgs particle. The electroweak contributions have been calculated through second order [23, 24], with the leading order Feynman diagrams shown in Fig. 1.5. The first diagram has an identical structure to the Schwinger diagram, with the only difference being that the photon is replaced by a Z boson or a Higgs particle. The other diagram represents the conversion of a muon to a W boson, with the emission and subsequent recapture of a neutrino. With the Higgs mass having been measured at the LHC, the reported contribution to a_μ^{SM} from electroweak terms is [23]

$$a_\mu(EW) = (15.36 \pm 0.10) \times 10^{-10}. \tag{1.31}$$

This is a 1.3 ppm contribution to a_μ^{SM}. The uncertainty of the electroweak contribution, while approximately 13 times larger than the QED uncertainty, is still negligible when compared to the achievable experimental uncertainty on the measurement of a_μ.

1.4.3 Hadronic Contributions

Hadronic contributions to a_μ^{SM} come from Feynman diagrams including particles sensitive to the strong interaction, such as quarks. While the overall contribution to a_μ^{SM} from these dia-

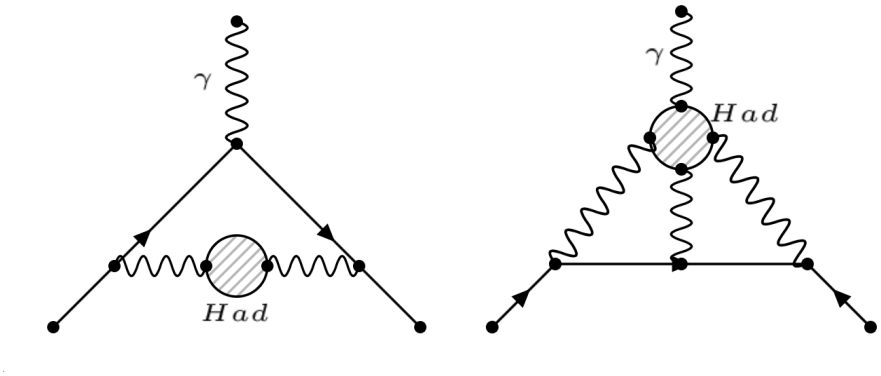

(a) Vacuum polarization diagram. (b) Light-by-light scattering diagram.

Figure 1.6 – The lowest order hadronic vacuum polarization and hadronic light-by-light scattering Feynman diagrams which contribute to a_μ^{SM}.

grams is small (as are all contributions other than those from QED diagrams), the uncertainty on the hadronic contributions dominates the uncertainty of the standard model prediction. Unlike the QED and EW contributions, hadronic contributions can not be calculated using perturbative expansions, but rather must be calculated using dispersion integrals and experimentally measured cross sections [17, 18, 25]. The hadronic contributions are split into two categories, vacuum polarization contributions and light-by-light scattering contributions.

Hadronic Vacuum Polarization Contributions

Fig. 1.6a shows the lowest order diagram which contributes to the hadronic vacuum polarization term of a_μ^{SM}. The diagram looks identical to some QED diagrams, but it is a hadron which undergoes pair production and subsequent annihilation, as opposed to a lepton.

The calculation of hadronic vacuum polarization contributions uses experimentally measured cross sections

$$\sigma^0_{had,\gamma}(s) \equiv \sigma^0 \left(e^+e^- \to \gamma^* \to \text{hadrons} + \gamma\right), \tag{1.32}$$

where the superscript 0 denotes the bare cross section (no vacuum polarization effects) and

the subscript γ denotes the inclusion of effects from final state photon radiation. The lowest order vacuum polarization contribution can be obtained from

$$a_\mu^{Had,LO,VP} = \frac{\alpha^2}{3\pi^2}\int_{m_\pi^2}^{\infty}\frac{ds}{s}R(s)K_\mu(s), \tag{1.33}$$

where $K(s)$ is a kernel function and $R(s)$ is the hadronic R-ratio given by

$$R(s) = \frac{\sigma^0_{had,\gamma}(s)}{4\pi\alpha^2/(3s)}. \tag{1.34}$$

The next to leading order term can be calculated similarly, using dispersion integrals and kernel functions [17, 18, 26].

The cross section data used to calculate the hadronic R-ratio comes from a range of experiments which measure cross sections for various particles. Fig. 1.7 shows the contributions to the hadronic R-ratio. Combination of the different data sets must be carefully undertaken. Two groups have recently completed independent analyses of $a_\mu^{Had,VP}$, with details given in KNT19 [18] (an update to the results reported in KNT18 [17]) and DHMZ19 [25].

The reported leading order contributions from hadronic vacuum polarization are

$$\begin{aligned} a_\mu^{Had,VP,KNT19} &= (692.78 \pm 2.42)\times 10^{-10} \\ a_\mu^{Had,VP,DHMZ19} &= (693.9 \pm 4.0)\times 10^{-10}, \end{aligned} \tag{1.35}$$

with the dominant contributions coming from $\pi^+\pi^-$ cross section data. These values represent only a 60 ppm contribution to a_μ^{SM}, but account for the largest fraction of the total standard model uncertainty. New $\pi^+\pi^-$ cross section measurements by BaBar, CMD-3, SND, and possibly BELLE-2, in addition to new measurements of R-ratio data by BESIII and experiments at Novosibirsk (SND, CMD-3, KEDR), will help to reduce these uncertainties [17]. The $g-2$ theory community additionally plans to release a white paper in December 2019 with updates on the hadronic contributions to a_μ^{SM}.

Hadronic Light-by-Light Scattering Contributions

The simplest hadronic light-by-light scattering Feynman diagram is shown in Fig. 1.6b, and involves the interaction of a propagating muon with 3 photons. These photons interact with

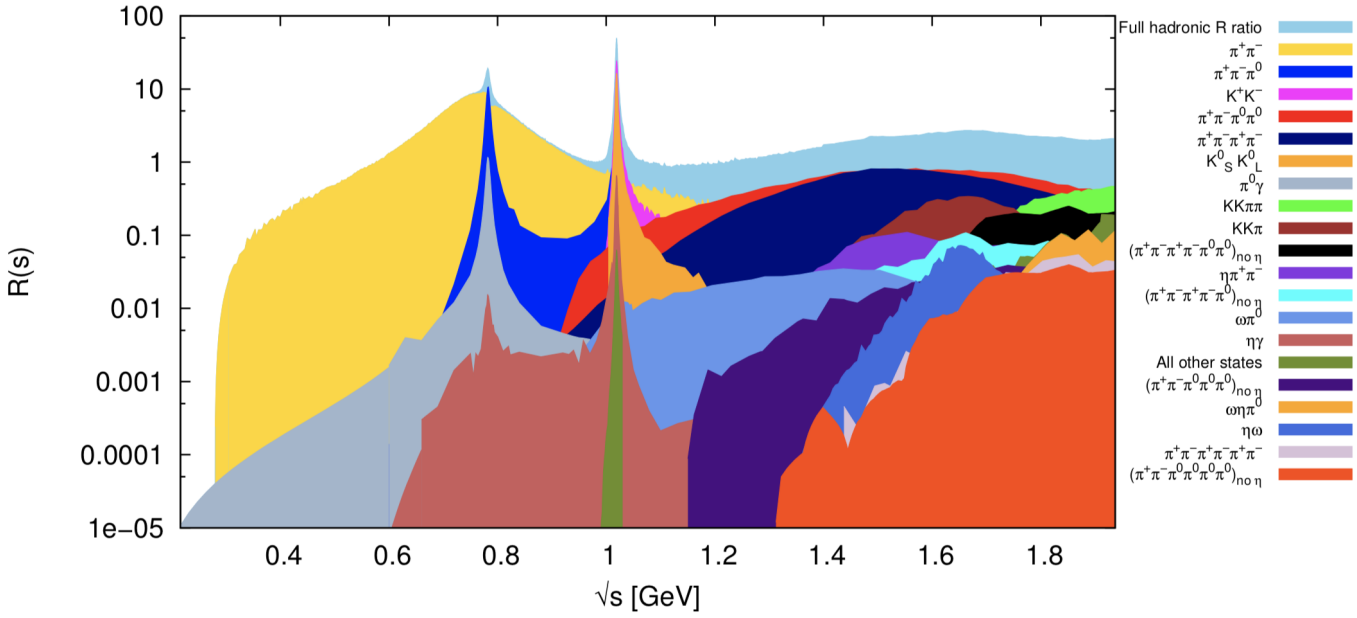

Figure 1.7 – Many e^+e^- cross section measurements contribute to the hadronic R-ratio. The contributions are pictured, with the final states listed on the right-hand side. The R-ratio is an important input in calculating the hadronic vacuum polarization contribution to a_μ^{SM}. Image credit: [17]

hadronic matter, which in turn interacts with an external photon. Similar to the vacuum polarization diagrams, the contribution from light-by-light diagrams can not be calculated perturbatively. Instead, various model-dependent approaches have been used, including models based on chiral perturbation theory estimates, perturbative quantum chromodynamics, and meson exchanges [17, 26]. Theorists are also working on data-driven and model independent calculations of $a_\mu^{Had,LbL}$, with details of one such calculation given in [27].

The commonly accepted value for $a_\mu^{Had,LbL}$ is known as the "Glasgow consensus"[3] [28]. Recent works have re-evaluated this value after it was noted that the contribution from axial exchanges was overestimated due to an incorrect assumption about the symmetry of form factors for the axial meson contribution under the exchange of two photon momenta [29]. KNT19 [18] reports a value for the hadronic light-by-light contribution of

$$a_\mu^{Had,LbL} = (9.34 \pm 2.92) \times 10^{-10}, \tag{1.36}$$

a contribution approximately 74 times smaller than that of $a_\mu^{Had,VP}$ (Eq. 1.35), but with a similarly sized uncertainty.

1.5 Current Status of Theory vs. Experiment

The relative contributions to a_μ^{SM} from all of the terms in Eq. 1.25, in addition to their contributions to the overall uncertainty, are pictured in Fig. 1.8. The standard model value is almost entirely comprised of the QED contributions, while the uncertainty is dominated by the hadronic terms.

Combining all terms, KNT19 [18] report a value for a_μ^{SM} of

$$a_\mu^{SM} = (11659181.08 \pm 3.78) \times 10^{-10}. \tag{1.37}$$

This value represents from just one analysis of the standard model contributions. Fig. 1.9 shows a comparison of various analyses, all in agreement with one another. This value can

[3]The December 2019 white paper is expected to provide an updated value.

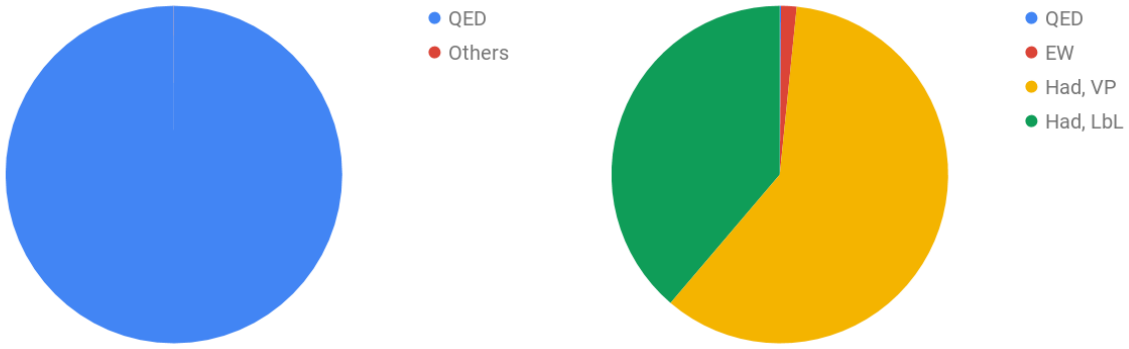

(a) a_μ^{SM} contributions.

(b) a_μ^{SM} uncertainties.

Figure 1.8 – The relative sizes and associated uncertainties of the contributions to a_μ^{SM}. While the standard model value is dominated by QED contributions, the largest uncertainties come from hadronic contributions.

be compared to the final E821 experimental result, leading to a discrepancy of

$$\Delta a_\mu = (28.02 \pm 7.37) \times 10^{-10}, \tag{1.38}$$

or 3.8σ. Should the Fermilab experiment achieve the 140 ppb uncertainty goal and measure the same central value as the E821 result, this discrepancy would increase to approximately 7σ, evidence of physics beyond the standard model [18]. A second, independent experimental measurement of a_μ will be made at the Japan Proton Accelerator Research Complex [30]. This measurement will use a very different experimental set up from the Brookhaven or Fermilab experiments and will provide a necessary cross check of the other measurements.

1.5.1 New Theoretical Contributions

New physics models which could account for the observed discrepancy between a_μ^{SM} and a_μ^{exp} have been the focus of a lot of work and discussion in the theory community. These include such models as supersymmetry, dark photons, and radiative mass corrections. The size of

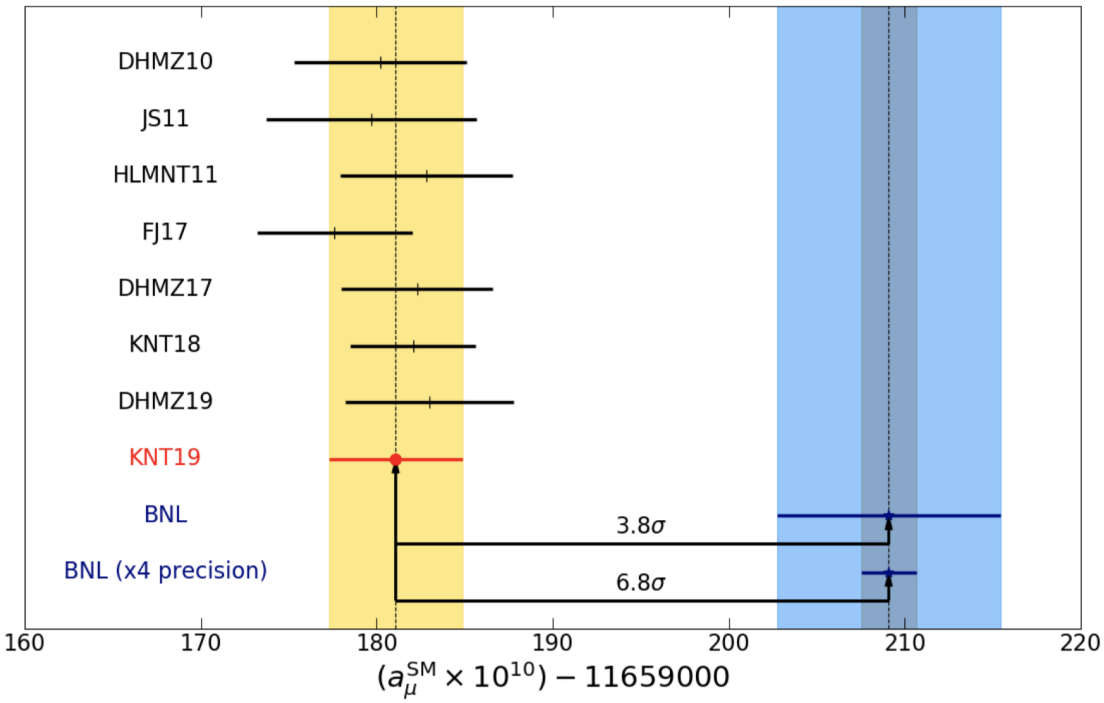

Figure 1.9 – A comparison of different analyses of a_μ^{SM}. All analyses are in agreement with one another. Using the KNT19 [18] result, a 3.8σ deviation exists between standard model calculations and the Brookhaven measurement of a_μ. If the Fermilab experiment achieves its precision goal and measures the same central value as the Brookhaven experiment, this deviation will increase to 6.8σ. Image credit: [18]

the contribution from new physics goes as

$$\Delta a_l^{\text{New Physics}} \simeq m_l^2/\Lambda^2, \tag{1.39}$$

where l represents the lepton flavor and Λ approximates the scale of the new physics [31]. This relationship shows that comparison of experimental and theoretical values of a_μ is approximately 43,000 times more sensitive to new physics than a similar comparison for a_e. The current size of the discrepancy puts constraints on the allowed parameter space that any new physics models must occupy.

One popular model to explain the discrepancy is supersymmetric (SUSY) contributions to a_μ^{SM}. In this model, smuon-neutralino and sneutrino-chargino loops must be accounted for. Depending on the SUSY masses, mixing, and other involved parameters, the possible contributions from supersymmetry can span a broad range of parameter space [31]. While many such models have been postulated, experiments at the LHC can explore much of the parameter space relevant to the $g-2$ discrepancy. Much of the parameter space has already been excluded, however small allowed regions still remain [32].

Another popular class of models are radiative muon mass models. These models were first proposed to explain why lepton masses are so much smaller than boson masses. The basic idea is that leptons begin with zero mass and only gain mass through quantum loop effects, due to new particles. The same source of chiral symmetry breaking which gives the muon mass would also contribute to a_μ^{SM}. The contribution would likely go as

$$a_\mu(\text{New Physics}) \simeq C\frac{m_\mu^2}{M^2}, \tag{1.40}$$

with M a mass associated with the new physics and C a model-dependent number of $\mathcal{O}(1)$ [31].

Finally, the proposed dark photon could also explain the $g-2$ discrepancy. In this model, there is an extra U(1) force carrier which couples to the standard model via kinetic mixing, with the dark photon needing to be relatively light to explain the observed discrepancy. The mixing parameter ϵ which governs the coupling of the dark photon to the electromagnetic

charge can have a value within a large parameter space [33]. In their 2015 publication, the NA48/2 collaboration reported that the entire parameter space of visible decay channels for the dark photon[4] which could resolve the muon $g-2$ discrepancy has been excluded [34]. The invisible decay channels have also been excluded by the NA64 and BaBar collaborations [35, 36]. The possibility of inelastic dark matter which undergoes semi-visible decays, ie decays where there are both visible and invisible particles present in the end state, was first proposed in 2001 [37]. New papers report that the relevant parameter spaces of such models have evaded experimental detection and could still explain the muon $g-2$ discrepancy [38, 39].

While many models have been proposed to explain the longstanding discrepancy between experimental measurements and standard model calculations of the anomalous magnetic moment of the muon, none have been verified. As the Fermilab E989 collaboration works towards an even more precise experimental measurement, the theoretical community continues to try to explain the discrepancy. The remaining final few years of data collection and analysis will be an exciting period, likely leading to either a reduced, inconsequential discrepancy or the discovery that the standard model can not accurately calculate the anomalous magnetic moment of the muon.

[4]In this context, a "visible" decay channel refers to one in which the decay particles are standard model leptons.

Chapter 2

THE FERMILAB MUON $g-2$ EXPERIMENT

2.1 Measurement Overview

The Fermilab E989 muon $g-2$ collaboration aims to measure the anomalous magnetic moment of the muon to 140 ppb, a fourfold improvement over the most recent measurement by the E821 collaboration at Brookhaven National Laboratory [10]. The basic measurement principle of both experiments builds upon the principles of the CERN II and III experiments (Sec. 1.3). Both experiments use a magnetic storage ring, but unlike the CERN experiments, a polarized muon beam is injected into the storage ring. The storage ring's highly uniform magnetic field provides radial containment while electric quadrupoles are used for vertical containment. A magnetic kicker deflects the muon beam onto a storage orbit with the proper radius. The momentum and spin vectors of the muons precess at different rates, leading to an anomalous precession frequency given by Eq. 1.22. The anomalous precession frequency is measured by calorimeters, while the magnetic field in the muon storage region is measured using pulsed nuclear magnetic resonance probes [9, 10]. Details about each of these systems will be provided in subsequent sections and chapters.

The anomalous magnetic moment of the muon can be extracted from these two measurements using the relationship of Eq. 1.20, which is reproduced here:

$$\vec{\omega}_a = -a_\mu \frac{q\vec{B}}{m}. \tag{2.1}$$

In order to extract a_μ with the desired precision, all terms must be known to a similar precision. The magnetic field can be rewritten in terms of the Larmor precession frequency of free protons ω_p and the proton's magnetic dipole moment μ_p as

$$B = \frac{\hbar\omega_p}{2\mu_p}. \tag{2.2}$$

The elementary charge can be written in terms of the electron mass m_e, the electron dipole magnetic moment μ_e, and the electron g-factor g_e as

$$e = \frac{4 m_e \mu_e}{\hbar g_e}. \tag{2.3}$$

Inserting Eqs. 2.2 and 2.3 into Eq. 2.1 yields

$$a_\mu = \frac{g_e}{2} \frac{\omega_a}{\omega_p} \frac{m_\mu}{m_e} \frac{\mu_p}{\mu_e}. \tag{2.4}$$

In practice, due to nonuniformities of the magnetic field and the muon beam distribution, ω_p is replaced by $\widetilde{\omega_p}$, the Larmor precession frequency of free protons weighted by the spatially averaged distribution of muons in the magnetic storage ring. The final equation used by the E989 collaboration for extracting a value of a_μ from measurements of the muon anomalous precession frequency and the magnetic field is

$$a_\mu = \frac{g_e}{2} \frac{\omega_a}{\widetilde{\omega_p}} \frac{m_\mu}{m_e} \frac{\mu_p}{\mu_e}. \tag{2.5}$$

The values of g_e, m_μ/m_e, and μ_p/μ_e are known to high precision from other experiments, while both ω_a and $\widetilde{\omega_p}$ are measured in the Fermilab experiment [10].

The Fermilab experiment uses the same magnetic storage ring as was used in the Brookhaven experiment, but the kickers, electric quadrupoles, calorimeters, and nuclear magnetic resonance probes were all redesigned and built new. The increased precision goal requires a large number of muons, which would be difficult to achieve in a timely manner at Brookhaven National Laboratory. The decision was made to move the experiment to Fermilab, a move which took place during the summer of 2013. Fermilab is able to provide a muon beam for typically 6-9 months per year, with an 11.4 Hz repetition rate for fills into the storage ring. This is in comparison to 10-12 weeks of available beam time with a 4.4 Hz repetition rate at Brookhaven [10].

2.2 Magnetic Storage Ring

The largest hardware component of the Fermilab experiment is a 7.11 m radius magnetic storage ring, shown in place in the MC1 experimental hall at Fermilab in Fig. 2.1. Several

Parameter	Value
Design magnetic field	1.45 T
Design current	5200 A
Equilibrium orbit radius	7112 mm
Muon storage radius	45 mm
Cold mass	6.2 metric tons
Helium-cooled lead resistance	6 μΩ
Yoke height	157 cm
Yoke width	139 cm
Pole width	56 cm
Iron mass	682 metric tons
Nominal gap between poles	18 cm

Table 2.1 – Magnetic storage ring parameters. Table reproduced from [10].

important magnet parameters are listed in Tab. 2.1, while a cross-sectional view of the storage ring is shown in Fig. 2.2. The cross section has C-shape to facilitate detecting decay positrons in the storage ring interior.

Due to its size and weight (>7 m radius, 682 metric tons), the storage ring is split into many smaller pieces. The outermost part of the storage ring, the yoke, is split into twelve 30° segments. Each yoke contains six pole pieces (each of which is 10° wide), 24 wedge shims, and other components discussed in Ch. 4. Four continuous superconducting coils operating at approximately 5200 A are used to produce a 1.45 T magnetic field [41].

A muon beam is injected into the storage ring vacuum chambers through a channel known as the inflector (Sec. 2.4). At the time-dilated muon lifetime of 64.4 μs, muons traverse the storage ring circumference hundreds of times on average before decaying. They orbit at the center of the opening of the C-shaped magnet in a region where the transverse magnetic field

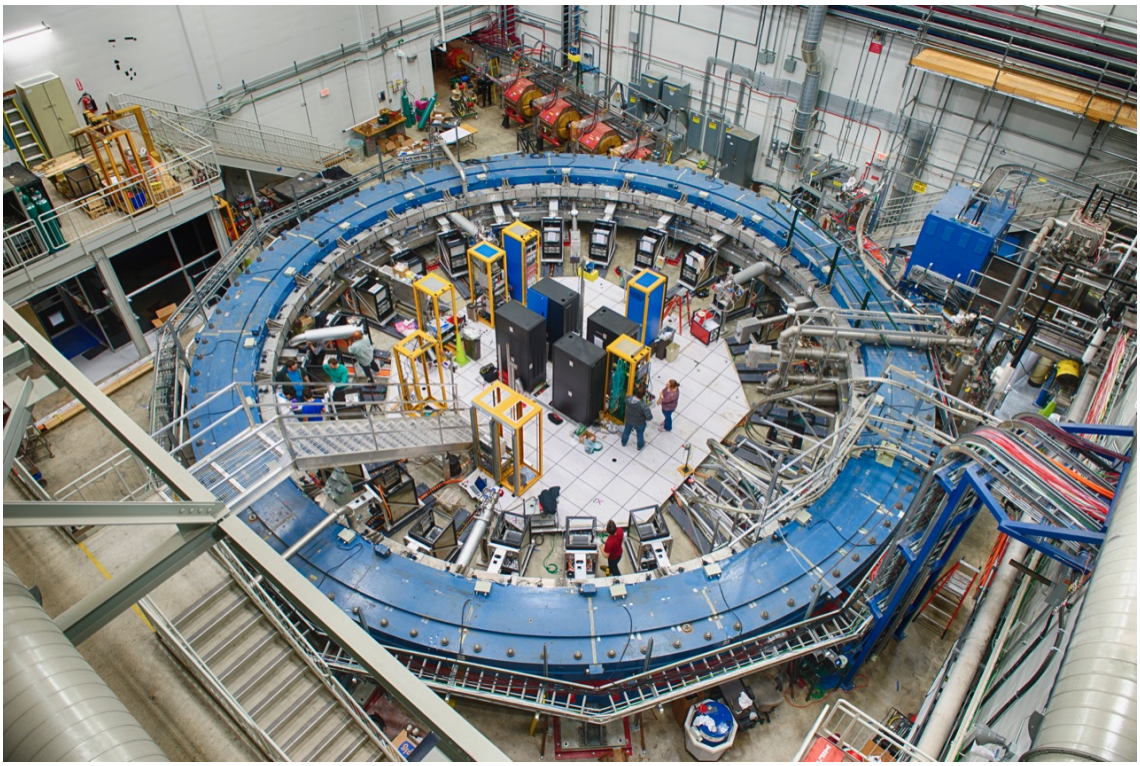

Figure 2.1 – The $g-2$ magnetic storage ring in the MC1 experimental hall at Fermilab. Muons are injected into the storage ring from the M5 final focus line, the red magnets behind the blue storage ring. Muons travel around the circumference of the storage ring, contained by the storage ring magnetic field, until they decay. Decay positrons are detected by calorimeters, located at 24 azimuthal locations. The author is pictured standing in the center of the storage ring with Fermilab colleague Brendan Kiburg.

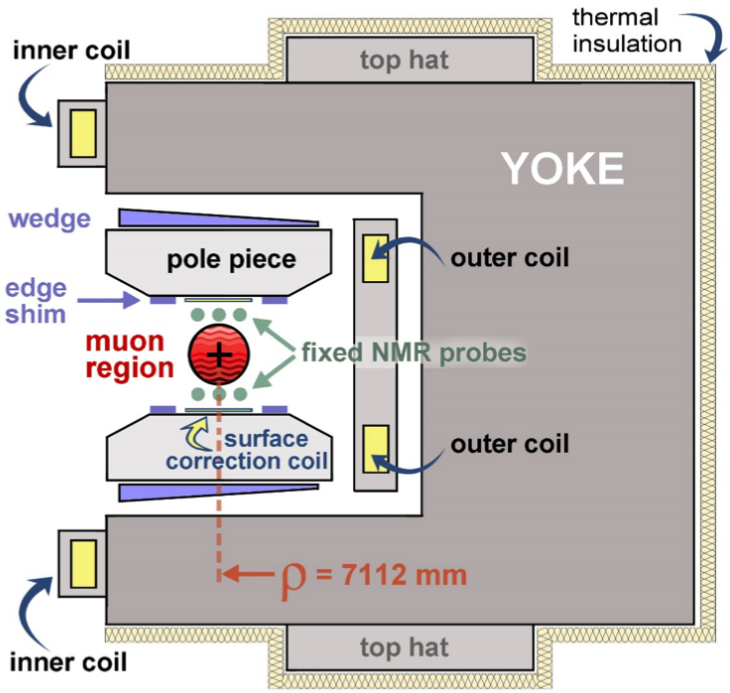

Figure 2.2 – A cross-sectional view of the magnetic storage ring. Four superconducting coils produce a 1.45 T magnetic field. Ultra-low-carbon steel pole pieces sit on an outer steel yoke. Muons traverse the storage ring circumference between the pole pieces, in the muon storage region. All other pictured components are used for magnetic field shimming (Ch. 4). Image credit: [40]

homogeneity is better than 1 ppm and varies by ±25 ppm peak-to-peak around the storage ring circumference. Ch. 4 describes how this magnetic field homogeneity was achieved.

2.3 Muon Beam Production

The Fermilab accelerator complex provides the $g-2$ experiment with an intense beam of highly polarized muons centered around the magic momentum of 3.094 GeV/c. The polarized muon beam is delivered to the experiment in fills, with a minimum temporal separation of 10 ms and an average rate of 11.4 Hz. As the cyclotron period of muons in the storage ring is 149 ns, each fill must have a smaller temporal width, with a goal of approximately 120 ns. The muon beam begins as a proton beam, which impinges on a target and produces pions. The pions decay to muons, from which muons of the proper momentum are selected and injected into the $g-2$ magnetic storage ring. A brief summary of these steps is provided below, with more detailed descriptions available in [10, 42].

The beamline elements used for muon production are shown in Fig. 2.3. The initial beam is comprised of protons. It is accelerated in the linac to 400 MeV/c before being injected into the Booster where it is further accelerated to 8 GeV. Due to a mismatch in sizes between the Booster ring and the $g-2$ storage ring, the proton beam that is accelerated in the Booster is too long to fit within one revolution of the storage ring. The proton beam is injected into the recycler, where it is split into four bunches, each of which can fit within one revolution of the $g-2$ storage ring. Each bunch from the recycler contains $\mathcal{O}(10^{12})$ protons and has a width of approximately 120 ns.

One by one, each bunch from the recycler is directed down the P1, P2, and M1 lines to the AP0 target hall. The proton beam is focused to a small transverse spot before impinging on an Inconel target. Secondary positively charged particles, mostly pions and remaining protons, are collected using a lithium lens. Particles with a momentum of 3.11 GeV/c (±10%) are selected using a bending magnet, while off-momentum particles proceed directly to a beam dump.

The secondary momentum-selected beam travels down the M2/M3 beamlines, during

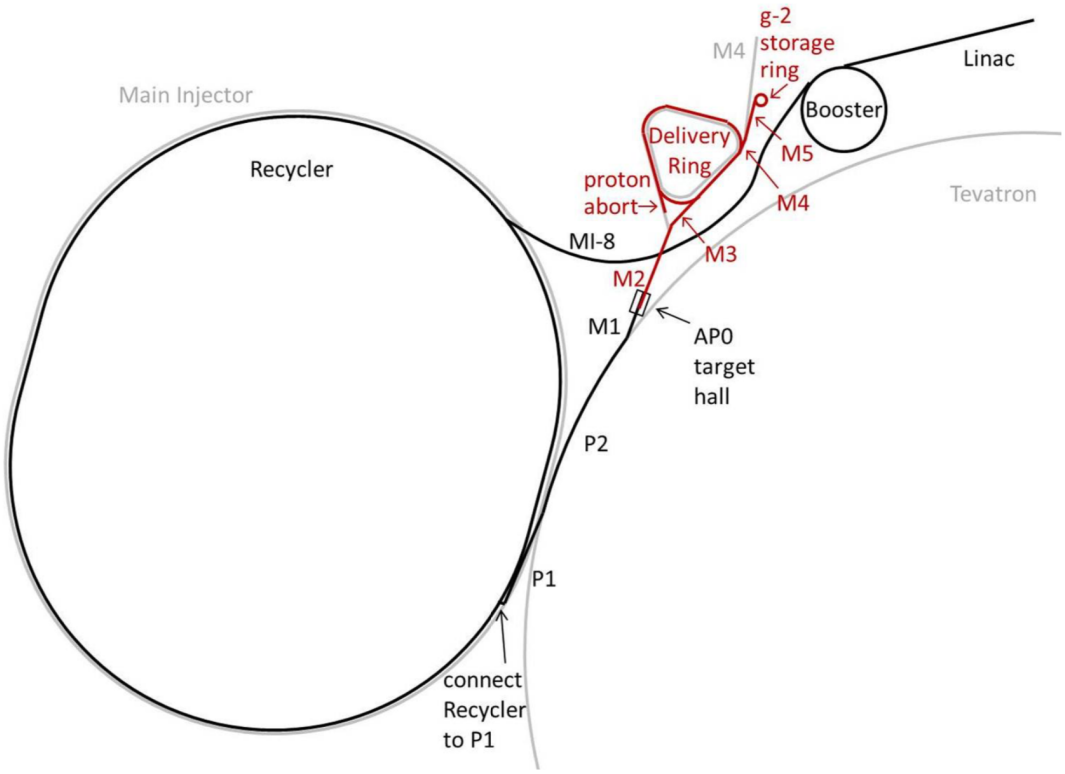

Figure 2.3 – The Fermilab beamline elements used to produce a polarized muon beam for the muon $g-2$ experiment. A proton beam (black elements) is accelerated in the linac and Booster. In the recycler, the proton beam is split into bunches. Each bunch travels through the P1, P2, and M1 lines before impinging upon a pion production target in the AP0 target hall. The secondary beam (red elements) travels through the M2 and M3 lines, before traveling around the delivery ring four times. The now primarily muon beam travels down the M4 and M5 lines before injection into the $g-2$ magnetic storage ring. Image credit: [10]

which time pions decay into muons, forming the polarized muon beam necessary for the $g-2$ measurement. The composite beam is then directed into the Delivery Ring (DR), a ring with a 500 m circumference which serves two purposes. The beam traverses the circumference of the DR four times, allowing remaining pions to decay into muons. Additionally, the muons separate in time from the heavier, same momentum protons still present in the beam. After four turns, muons are allowed to pass on to the next section of beamline while a kicker removes the protons.

The final beamline segments before the muon beam enters the $g-2$ magnetic storage ring are the M4 and M5 lines. The M4 line is primarily used to transport the muon beam from the DR to the MC1 building. The M5 line, known as the final focus section of the beamline, is used to make final preparations to the momentum-selected polarized muon beam.

2.4 Beam Injection and Storage

At the end of the M5 line, the muon beam arrives at the entrance to the $g-2$ magnetic storage ring. It is injected into the storage region through a superconducting inflector magnet, installed in a hole which was bored through the storage ring yoke. Without the inflector present, the fringe field from the storage ring magnetic field would make muon injection into the storage region impossible, as the muons would be deflected into the yoke steel. The inflector magnet was designed to cancel the fringe field in the bore, providing the muon beam a field-free path to enter into the storage region [43]. The inflector placement and magnetic field distribution are shown in Fig. 2.4.

As the muon beam exits the inflector and enters the muon storage area, it is radially offset from the center of the muon storage region by 77 mm. In order to center the muon beam, a set of pulsed kicker magnets is used to deflect the muons. The kicker system is located 90° downstream of the inflector entrance and consists of three sets of plates across which high currents are applied to create a pulsed magnetic field. Fig. 2.5 shows the relative locations of the inflector magnet and the kicker plates. The ideal kick is a square pulse with the necessary amplitude to deflect magic momentum muons approximately 11 mrad in the

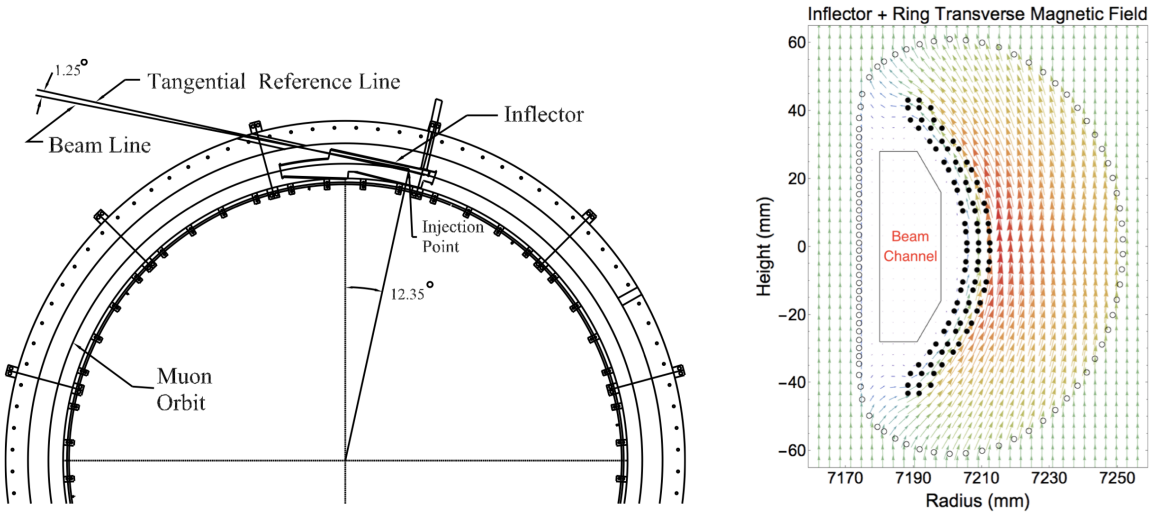

(a) Inflector channel.

(b) Inflector magnetic field.

Figure 2.4 – The muon beam enters the magnetic storage ring through a hole bored in a yoke segment. A superconducting inflector magnet is used to cancel the fringe field of the storage ring magnetic field, providing the muon beam with a field free entrance channel. The inflector position in the yoke is shown in (a) while the magnetic field distribution inside of the inflector is shown in (b). The radial position is relative to the center of the storage ring and the height is relative to the nominal muon beam orbit. Image credit: [43] and [42]

radial direction and a width shorter than the muon orbital period of 149 ns, such that all particles are kicked only once [10, 44].

With the muon beam orbiting at the correct radius, the vertical magnetic field provides radial containment. For particles with momentum only in the azimuthal direction, nothing is needed for vertical containment. However, any particle with a momentum component parallel to the magnetic field would be quickly lost. To combat these losses and provide vertical containment, electric quadrupoles are used. The quadrupoles consist of four sets of four plates (the four sets cover 43% of the storage ring circumference, as shown in Fig. 2.5) across which high voltage is applied to create an electric field which varies as shown in Fig. 2.6. Muons which are vertically high (low) feel a downwards (upwards) force [10, 45]. The magnetic field and electric quadrupoles are used in conjunction to contain the muon beam in both transverse directions.

2.5 $\widetilde{\omega_p}$ *Measurement*

The magnetic field in the muon storage region of the storage ring must be well known in order to extract a value of a_μ with high precision. In order to extract $\widetilde{\omega_p}$, both the magnetic field distribution and the muon beam distribution must be known. These comprise two separate measurements which are later combined, as discussed in Sec. 3.7.

2.5.1 Magnetic Field Measurement

The magnetic field strength and variations within the muon storage region of the storage ring are of utmost importance to the $g-2$ experiment. The nominal 1.4513 T magnetic field serves to radially contain muons with the magic momentum of 3.094 GeV/c in a stable orbit with a radius of 7.112 m [9, 10]. Azimuthal variations of the magnetic field cause local disturbances to the muon beam orbit.

Pulsed nuclear magnetic resonance (pNMR) probes are used to measure the magnetic field. A "trolley" carrying an array of 17 pNMR probes measures the magnetic field in the muon storage region approximately every three days. A suite of 378 pNMR probes embedded

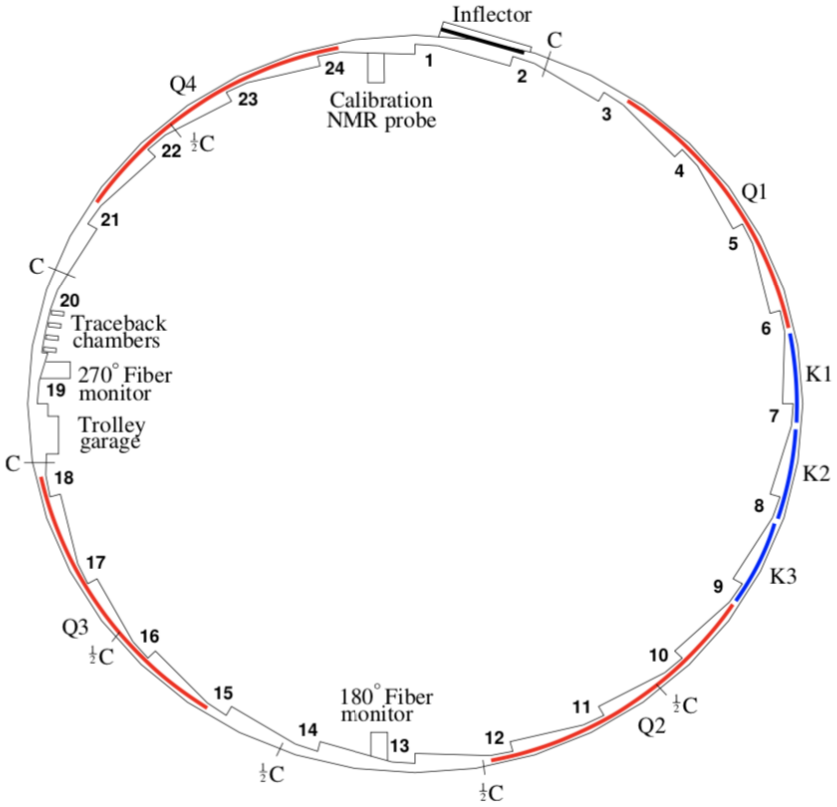

Figure 2.5 – The end of the inflector channel (black) is radially offset from the ideal muon orbit by 77 mm. A set of pulsed kicker magnets (blue) located 90° downstream of the inflector exit deflect the muon beam onto the ideal orbit. Electric quadrupoles (red) cover 43% of the storage ring circumference and are used for vertical containment of the muon beam. Image credit: [10]

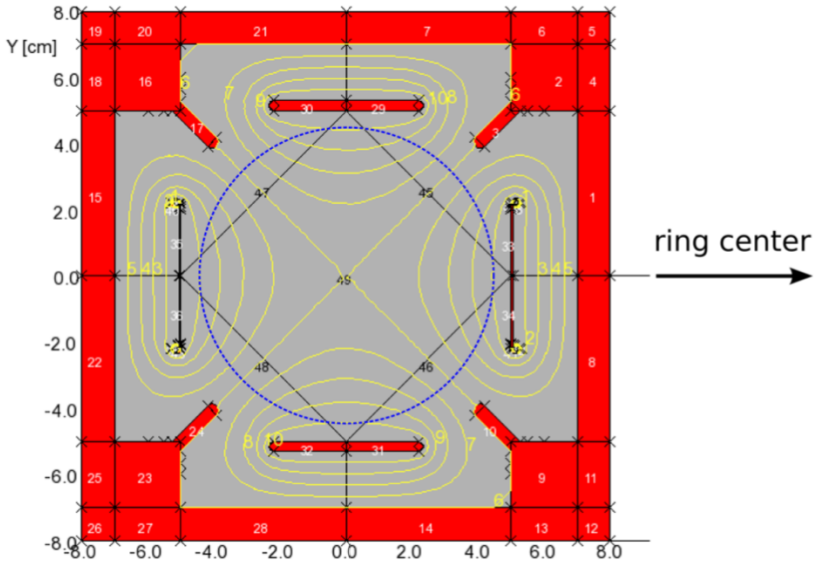

Figure 2.6 – Electric quadrupoles are used for vertical containment of the muon beam. The quadrupoles consist of four plates at high and low voltages. The muon storage region is marked in blue and electric field lines are drawn around the quadrupole plates. Muons which are high (low) feel a downwards (upwards) force from the electric field. Image credit: [10]

in grooves in the top and bottom walls of the vacuum chambers monitor the magnetic field evolution while muons are present. In order to relate the measurements from the pNMR probes to measurements of the Larmor precession of free protons, a "plunging probe" with well understood characteristics is used for calibration. The $g-2$ pNMR probes are discussed in Sec. 3.4, pNMR probe calibration in Sec. 3.5, and magnetic field analysis and tracking in Ch. 6.

The magnetic field homogeneity in the muon storage region was improved significantly during a period of shimming which took place from late 2015-August 2016. Magnetic field variations were improved both azimuthally, where variations have an RMS of less than 25 ppm, and transversely, where azimuthally averaged magnetic field variations are less than 1 ppm. Shimming, which is discussed in detail in Ch. 4, involved the addition and movement of almost 10,000 pieces of ferrous and non-ferrous materials around the muon storage region.

2.5.2 Muon Beam Distribution Measurement

The final a_μ^{exp} calculation requires knowing the muon-weighted magnetic field value, $\widetilde{\omega_p}$. The muon distribution is measured using straw tracking detectors, or "trackers". There are two tracking stations in the storage ring, at 180° and 270°, with each station containing eight tracker modules. Each module consists of four layers of straw tubes, with alternating planes oriented ±7.5° from vertical. Each row of straws contains either 32, 24, or 16 straws, depending on the location. Each straw consists of a Mylar outer shell threaded with a wire which can hold high voltage. A tracker module is pictured in Fig. 2.7a. The trackers sit in the vacuum chamber, just before the calorimeters (in the white space to the left of the calorimeters in Fig. 2.8).

As a positron passes through a tracking detector, it ionizes the Argon-Ethane gas mixture with which the straws are filled. The now freed electrons drift towards the sense wire, creating a measurable signal. The time of each signal is read out and the event is then defined as a straw hit. Hits close together in time are grouped into "time islands" which are analyzed to reconstruct both the positron trajectory and the positron birth time, position and momentum

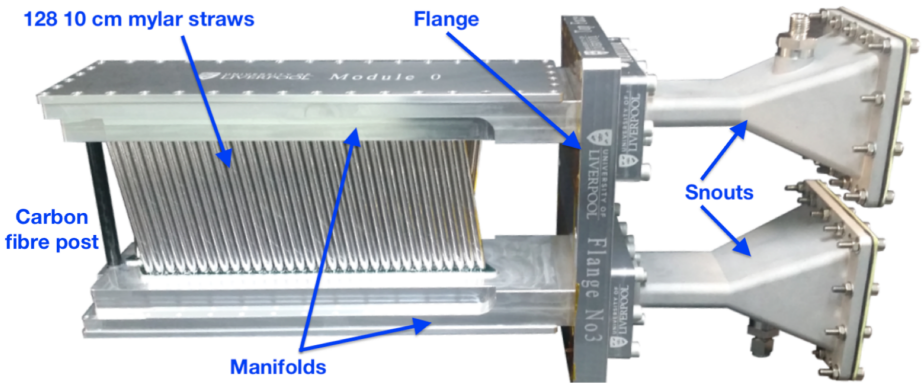

(a) Tracker module.

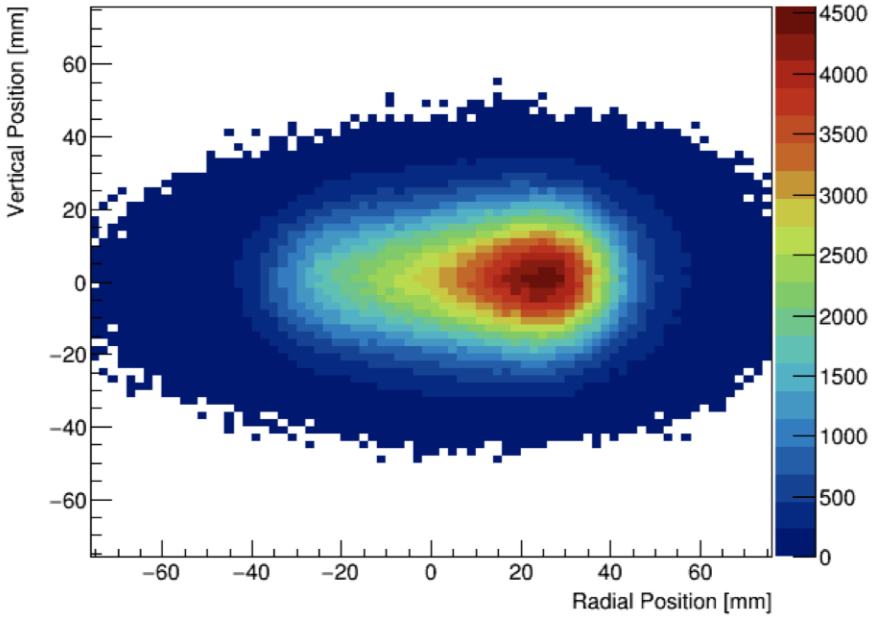

(b) Muon beam distribution.

Figure 2.7 – Each straw tracking detector station contains eight tracker modules (a), each of which contains four planes of high voltage wires threaded in mylar straws. As a positron passes through a straw, it ionizes the gas filling the straw and the free electrons drift towards the sense wire, creating a measurable signal. The positron birth times, locations, and momenta can be extracted from tracker measurements. The birth locations are used to reconstruct the stored muon beam distribution (b). Image credit: [46]

[10, 46]. The muon beam distribution is constructed by looking at the average birth positions of many positrons. An example beam distribution is shown in Fig. 2.7b.

2.6 Anomalous Precession Frequency Measurement

The other measurement which contributes to the a_μ^{exp} calculation is the measurement of ω_a, the anomalous precession frequency of muons in the storage ring. The anomalous precession, caused by a difference in spin and cyclotron precession frequencies, causes an oscillation in the number of positrons emitted in the forward direction. The value for ω_a is determined by observing decay positrons using calorimeters located in the center of the storage ring.

2.6.1 Calorimeters

When muons decay, the produced positrons move towards a lower radius due to their lower momenta. The positrons quickly exit the storage ring through thin aluminum windows in the vacuum chambers and are detected by electromagnetic calorimeters located at 24 evenly spaced azimuthal locations inside of the storage ring. Fig. 2.8 shows the path of both a high and low energy positron as it exits the storage ring and hits a calorimeter. The calorimeters are designed to measure the arrival time and energy of decay positrons, and are used to count the number of positrons with energy above a given threshold.

Each calorimeter station contains a 9×6 array of PbF_2 crystals, each of which has a silicon photomultiplier (SiPM) chip glued to its downstream face, as shown in Fig. 2.9. As a positron passes through a calorimeter, Cerenkov light is produced. This light is detected by the SiPMs and is used to extract the positron arrival time and energy. In order to avoid transmission of light between neighboring crystals, each crystal is wrapped in a light-tight cover. The segmented design, unique to the Fermilab experiment, allows for distinction between positrons which arrive within a short time window but at different positions, something which the Brookhaven calorimeters could not do. The pulses measured by the SiPMs are fit to custom pulse templates, from which the positron energy and arrival time can be extracted [10, 47].

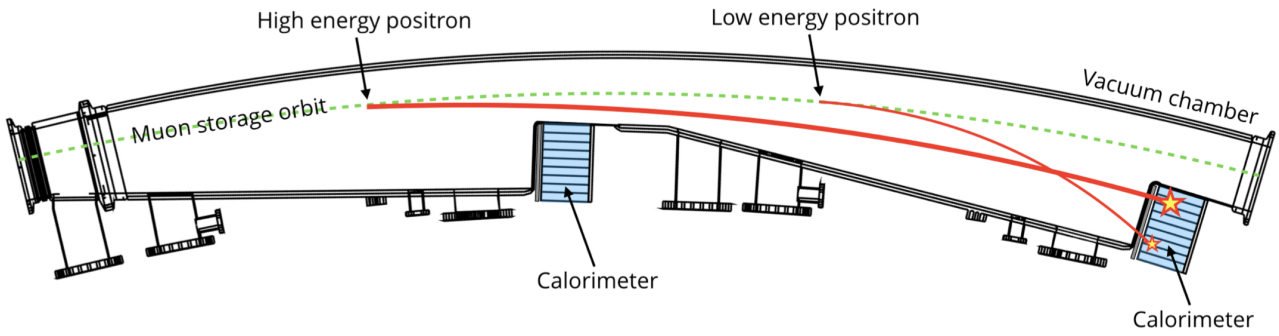

Figure 2.8 – After a muon decays, the produced positron curls towards the center of the storage ring due to its lower momentum. Upon exiting the vacuum chamber, positrons are detected by electromagnetic calorimeters, which are located at 24 evenly spaced azimuthal locations. Image credit: [47]

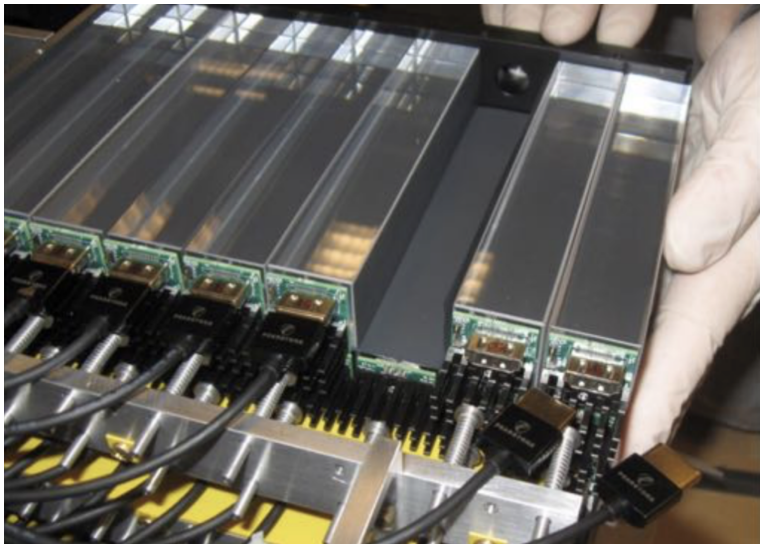

Figure 2.9 – Each calorimeter consists of a 9x6 array of PbF_2 crystals with attached silicon photomultiplier (SiPM) chips. The SiPMs detect the Cerenkov light produced in the crystals when a positron passes through a calorimeter. Image credit: [48]

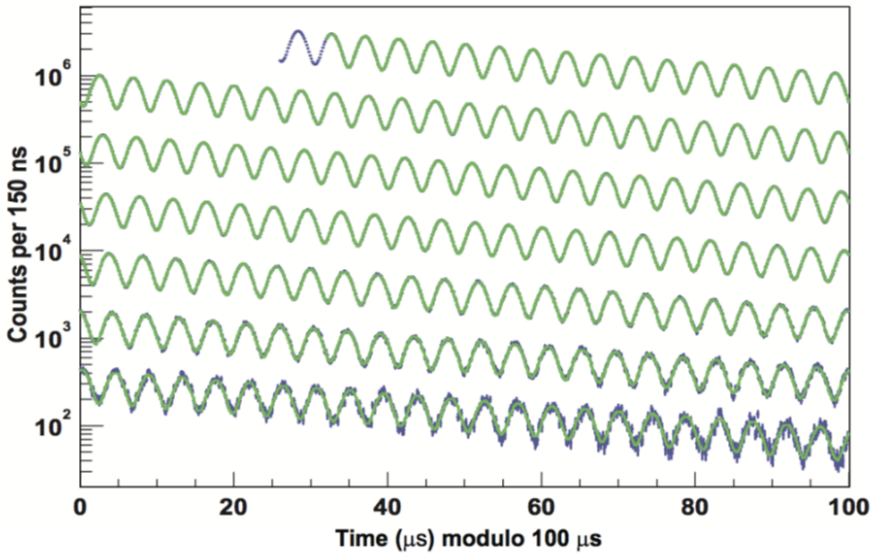

Figure 2.10 – Each detected positron with energy above a given threshold is inserted into a histogram. This plot shows oscillation due to the anomalous precession and exponential decay due to the finite muon lifetime. Image credit: [10]

2.6.2 ω_a Measurement

Positrons with an energy above a given threshold are added to a histogram, as shown in Fig. 2.10. The number N of high energy positrons striking the calorimeters as a function of time can be described in the most simple form as

$$N(t) = N_0 \exp\left(-t/\gamma\tau\right)\left[1 - A\cos(\omega_a t + \phi)\right], \tag{2.6}$$

where N_0 is a normalization factor, $\gamma\tau$ is the time-dilated muon lifetime, A is the decay asymmetry, and ϕ is an arbitrary phase [47].

In actuality, many effects must be considered to correctly describe the time variation of the signal recorded by the calorimeters, including but not limited to: muons don't orbit the storage ring following a simple elliptical path, but instead undergo betatron oscillation; some muons are not stored and pass through calorimeters; muons are not evenly distributed as a function of azimuth; due to betatron oscillations, muons have a momentum component in

the same direction as the magnetic field; off-momentum muons see the quadrupole electric field distribution as a motional magnetic field. There are also detector effects which must be accounted for. The final function used to fit the histogram of positron counts must account for all of these effects. Detailed descriptions of these effects can be found in Aaron Fienberg's thesis [49].

Chapter 3

MAGNETIC FIELD MEASUREMENT

3.1 Magnetic Field Measurement Goals

As discussed in Ch. 1, in order to precisely extract the anomalous magnetic moment of the muon (a_μ), the muon $g-2$ experiment carries out two precision measurements: a measurement of the anomalous precession frequency of muons in a magnetic field (ω_a) and a measurement of the magnetic field experienced by the muons. In practice, the magnetic field is measured as the precession frequency of free protons in the magnetic field, ω_p. To reach the final uncertainty goal of 140 ppb for a_μ, a 70 ppb uncertainty goal was set for the magnetic field measurement. A breakdown of the uncertainty budget for the magnetic field measurement is given in Tab. 3.1, together with the final uncertainties from the Brookhaven experiment. More details are provided in [9, 10]. The following sections detail the E989 magnetic field measurement hardware, with magnetic field analysis discussed in Ch. 6.

3.2 Nuclear Magnetic Resonance

The magnetic field in the muon storage region of the $g-2$ magnetic storage ring is measured using pulsed Nuclear Magnetic Resonance (pNMR) probes. The main probes used were built at the University of Washington. Two special pNMR probes were also designed and built at the University of Massachusetts [50] and University of Michigan [51]. These probes are used for calibration purposes, to relate measured precession frequencies to free proton precession frequencies.

The pNMR probes work based on the principle of the Larmor precession of spins when placed in a magnetic field. In vacuum, the Larmor precession of a particle's spin is related

Source of Uncertainty	**Uncertainty Achieved, Brookhaven (ppb)**	**Uncertainty Goal, Fermilab (ppb)**
Absolute calibration of standard probe	50	35
Calibration of trolley probes	90	30
Trolley measurements of B_0	50	30
Interpolation with fixed probes	70	30
Muon distribution	30	10
Time dependent external magnetic fields	-	5
Other sources (higher order magnetic field multipoles, kicker eddy currents, trolley temperature)	100	30
Total	170	70

Table 3.1 – The final uncertainties achieved in the Brookhaven magnetic field measurement (final combined uncertainty of 170 ppb) can be compared to the uncertainty goals for the Fermilab experiment (combined goal of 70 ppb).

to the magnetic field magnitude B as

$$\omega_L = \frac{geB}{2m}, \tag{3.1}$$

where ω_L is the Larmor precession frequency and g, e, and m are the g-factor, charge, and mass of the particle [52]. A brief summary of the basic principles of pulsed NMR, geared towards the $g-2$ pNMR probes, is provided below. Refs. [53] and [54] provide historical background information on nuclear magnetic resonance measurements.

One of the most crucial parts of any pNMR probe is the spin sample. In particular, a sample of protons, as found in petroleum jelly or water, is used in the $g-2$ pNMR probes. Due to the magnetic moment-field interaction, there is a small net magnetization of the proton sample when in the presence of an external magnetic field. This magnetization is aligned with the magnetic field. The fraction of aligned spins can be described by the Boltzmann equation [55]

$$N_{aligned} = \frac{e^{-\mu_z B_z/k_B T} - e^{\mu_z B_z/k_B T}}{e^{-\mu_z B_z/k_B T} + e^{\mu_z B_z/k_B T}}. \tag{3.2}$$

Using the CODATA values for μ_p and the Boltzmann constant k_B [3], $N_{aligned} \approx 4.94 \times 10^{-6}$ at room temperature (300 K) in the $g-2$ 1.45 T magnetic field. This is a small but useful fraction of aligned spins.

To initiate a magnetic field measurement with a $g-2$ pNMR probe, an RF magnetic field is superimposed around the proton sample. This causes the polarization vector of the sample to rotate into the plane perpendicular to the external magnetic field. With the frequency of the RF magnetic field chosen to be the expected Larmor precession frequency of protons, the magnetic field experienced by the sample is expressed as

$$\vec{B} = b\cos(\Omega t)\hat{x} + b\sin(\Omega t)\hat{y} + B_0\hat{z}, \tag{3.3}$$

where B_0 is the external magnetic field strength (defined to point in the $\hat{z}$ direction), b is the RF magnetic field strength, and Ω is the frequency of the applied RF magnetic field [56].

The $\hat{z}'$ component[1] of the spin precession vanishes in the frame rotating at a frequency $\Omega = \omega_{L,p}$, the Larmor precession frequency of protons (61.79 MHz in the $g-2$ magnetic field). Given a perfectly on-resonance RF magnetic field, the oscillating field in the $\hat{x}'$ direction looks constant[2], or $B_{x'} = b$. The net magnetization of the proton sample thus rotates about the x' axis, towards the $x-y$ plane. In the $g-2$ pNMR probes, the RF pulse is applied just long enough for the magnetization of the sample to rotate $\pi/2$ radians, until it lies in the $x-y$ plane. The RF pulse is thus referred to as a $\pi/2$ pulse.

After the RF pulse has been turned off, the polarization vector of the sample precesses in only the external magnetic field. This precession lasts until the net magnetization returns to being aligned with the external magnetic field. The precession component in the $x-y$ plane induces a detectable EMF in the same coil used to apply the RF pulse. The resultant signal is known as a free induction decay signal, or FID.

The resultant FID does not show a constant oscillation, but rather an oscillation with a decaying envelope. This decay is caused by two main factors: longitudinal relaxation and transverse relaxation. Longitudinal relaxation occurs due to the alignment of the spins in the sample with B_z. The precession component in the $x-y$ plane, which causes the induced EMF, is reduced as the spins move towards being aligned with the external magnetic field. This process proceeds exponentially with a characteristic time T_1. Transverse relaxation occurs for two reasons. The first is that the sample, while finite, is not point-like. In a magnetic field that is not perfectly homogeneous, each spin experiences a slightly different magnetic field. The spin precession for each spin therefore progresses slightly differently. This spin decoherence reduces the strength of the induced EMF. Spin-spin interactions between atoms in the sample additionally lead to further spin decoherence. Like longitudinal relaxation, transverse relaxation proceeds exponentially, with a characteristic time T_2.

The time evolution of the magnetization $\vec{M}$ after the RF pulse has been applied is de-

[1]Primed quantities represent the rotating frame.

[2]If the RF magnetic field is off resonance, a residual, time-varying field remains

scribed by the Bloch equations [56, 57]

$$\begin{aligned}
\frac{dM_x}{dt} &= -\gamma\left(M_y B_z - M_z B_y\right) - \frac{M_x}{T_2} \\
\frac{dM_y}{dt} &= -\gamma\left(M_z B_x - M_x B_z\right) - \frac{M_y}{T_2} \\
\frac{dM_z}{dt} &= -\gamma\left(M_x B_y - M_y B_x\right) - \frac{1}{T_1}\left(M_z - M_0\right),
\end{aligned} \tag{3.4}$$

where γ is the gyromagnetic ratio of the spin sample particles. In a perfectly uniform external magnetic field in the $\hat{z}$ direction, there would be no spin decoherence, i.e. $T_2 \to \infty$. The solutions to Eqs. 3.4 in the x and y directions would be given by a simple sinusoid with an exponentially decaying amplitude with characteristic time T_1:

$$M_{x,y}(t) = \exp^{-t/T_1} \sin(\omega t - \phi_0). \tag{3.5}$$

An example FID that would be produced in this magnetic field environment is shown in Fig. 3.1a. If the external magnetic field is not perfectly homogeneous, the resultant FIDs would look similar to Fig. 3.1b.

3.3 FID Frequency Extraction

The frequency of an FID encodes the magnetic field strength experienced by the spin sample in the pNMR probe, as described by Eq. 3.1. Magnetic field gradients, the finite extent of the sample, and the sensitivity of the pickup coil are just three of many effects which can affect the extraction of a frequency from an FID. Many methods for frequency extraction were studied, with details provided in [58]. A method known as the phase fit method is used in all following analyses. In this method, the phase of an FID, as opposed to the frequency, is extracted as a function of time.

The first step in the phase fit method of frequency extraction is the calculation of the Hilbert transform of the FID

$$h(t) = IFFT\left(-i \cdot sgn(\omega) f(\omega)\right), \tag{3.6}$$

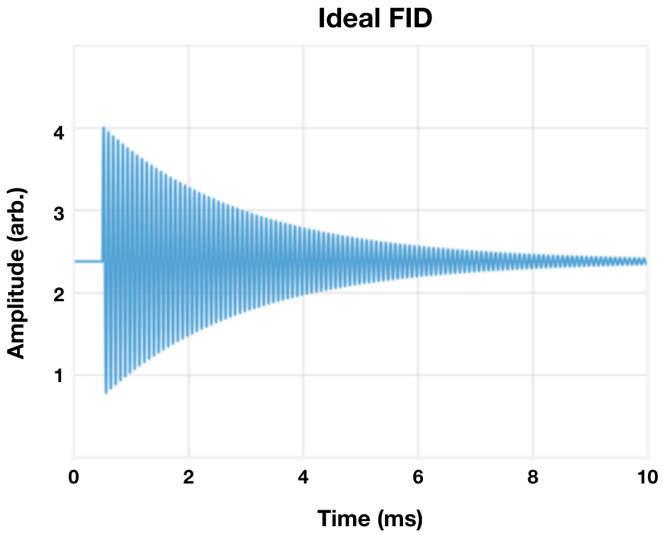

(a) Ideal FID.

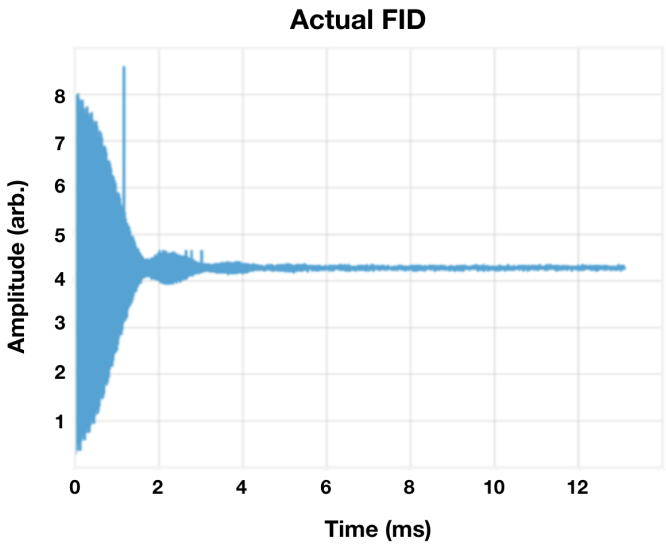

(b) Typical FID.

Figure 3.1 – In a perfectly homogeneous magnetic field, the FID produced by the relaxation of the net magnetization of a sample of spins after a $\pi/2$ pulse has been applied is a sinusoid with an exponentially decaying amplitude (a). In an inhomogeneous magnetic field, the resultant FIDs look more similar to (b). Image credit: [58]

where IFFT stands for Inverse Fast Fourier Transform and $f(\omega)$ is the Fourier transform of the FID signal in the time domain ($f(t)$). The Hilbert transform assigns an imaginary complement to each real part of a signal by shifting each Fourier component of the signal by a quarter of a period. In the frequency domain, this can be understood as adding a 90° phase shift to each Fourier component [59]. The phase as a function of time is extracted by taking the arctangent of the ratio of the FID and its Hilbert transform:

$$\phi(t) = \arctan\left(h(t)/f(t)\right). \tag{3.7}$$

As discussed, each spin in the sample experiences a slightly different magnetic field, causing the relaxation of each spin to proceed uniquely. Each spin thus contributes differing amounts to the measured FID as a function of time. Flowers et al analytically calculated the frequency distribution of an FID as an expansion in terms of moments and showed that the initial frequency of an FID corresponds to the centroid frequency of the signal [60]. For this reason, the FID frequency is extracted for use in the $g-2$ experiment as the linear slope of the extracted phase at time $t=0$, $\frac{\partial\phi}{\partial t}|_{t=0}$.

3.4 pNMR Probes

Three different types of pNMR probes were built for use in the Fermilab $g-2$ experiment. The first type of probe, of which over 400 were built, uses petroleum jelly as the proton sample. Two special probes, known as the plunging and ^{3}He probes, were built for calibration purposes.

3.4.1 Petroleum Jelly pNMR Probes

The basic design of the $g-2$ pNMR probes was first developed by the magnetic field team of the Brookhaven $g-2$ experiment. Fig. 3.2 shows a diagram of a BNL pNMR probe, a resonant RLC circuit. The probes initially used water doped with paramagnetic $CuSO_4$ as a spin source, where the doping agent was added to reduce the T_1 relaxation time. A coil wrapped around the source was used to both apply $\pi/2$ pulses and record the induced EMF.

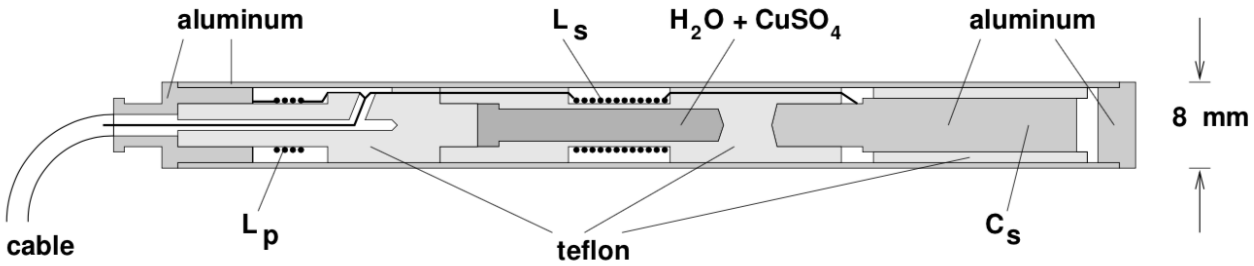

Figure 3.2 – Diagram of a Brookhaven pNMR probe. Water doped with $CuSO_4$ was used as a spin sample. A coil (L_s) wrapped around the water sample was used to both apply $\pi/2$ pulses and record the resultant FIDs. A teflon cylinder (C_S) could be moved in and out to tune the resonant circuit. The probes were housed within cylindrical aluminum shells. Image credit: [57]

A teflon cylinder could be moved in and out to tune the resonant circuit. The probes were housed within aluminum outer shells [57].

A sample Fermilab pNMR probe is shown in Fig. 3.3. Designed and built at the University of Washington, the probes draw from and improve upon the Brookhaven design. Each pNMR probe consists of two inductor coils, a Teflon sample holder, a tunable Teflon capacitor, an aluminum outer shell, and an RF cable with an SMA connector. One of the two coils surrounds a petroleum jelly sample and is used to both apply $\pi/2$ pulses and record the resultant FID signals. The other is used to match the 50Ω impedance of the cable.

Throughout the course of the Brookhaven experiment, the pNMR probe performance gradually worsened. The cause of this worsening was found to be the slow evaporation of the water samples, leading to the corrosion of the interior parts of the probes. Some probes were refilled with petroleum jelly, as time allowed [9]. All Fermilab probes use petroleum jelly as a proton source, with the petroleum jelly all coming from the same produced batch. These samples should neither evaporate nor cause corrosion.

An additional improvement was made in the connection between the pNMR probe body

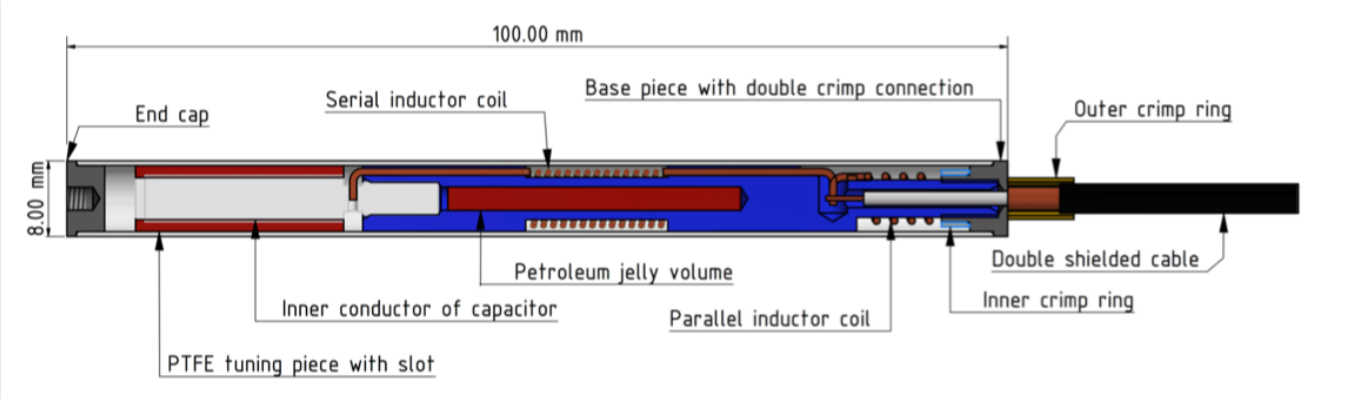

(a) Fermilab pNMR probe diagram.

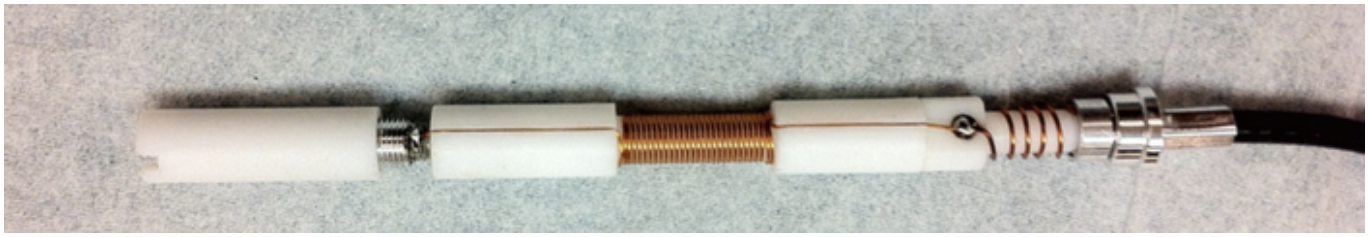

(b) Fermilab pNMR probe.

Figure 3.3 – A diagram and picture of one of the pNMR probes used to measure the magnetic field in the Fermilab $g-2$ experiment. A petroleum jelly sample is surrounded by a serial inductor coil which is used to both provide $\pi/2$ pulses to tilt the net magnetization of the sample and to measure the relaxation of the magnetization after the pulse has been applied. A teflon tuning capacitor is used to tune the resonant circuit to the expected Larmor precession frequency of protons in the $g-2$ magnetic field. A parallel inductor coil is used to tune the probe impedance. Image credit: [61]

and the signal cable. Many Brookhaven probes provided poor signals due to weak connections to the signal cable. In the Fermilab probes, a more stable crimp connection is used. Finally, an improvement was made to the tuning capacitor. In the Brookhaven probes, the outer aluminum shell had to be removed to tune a probe's resonant frequency. Each removal of the shell provided an opportunity to damage the probe in various ways. In the Fermilab probes, only an end cap needs to be removed to tune the resonant frequency. With the cap removed, a special screwdriver can be used to adjust the position of the Teflon capacitor, thereby changing the capacitance of the pNMR probe.

The process for assembling and tuning the Fermilab pNMR probes was developed at the University of Washington [62]. The first step in building a probe involves filling the Teflon sample holders with petroleum jelly. As petroleum jelly is a solid at room temperature, it is first melted in a 90 °C water bath. The sample holders are warmed in this same bath, as shown in Fig. 3.4. The melted petroleum jelly is transferred into the warm sample holders using a syringe which has also been warmed in the same water bath, before being removed from the bath and allowed to cool to room temperature. This procedure makes the filling process simple, in addition to minimizing the risk of air bubble formation.

Once the sample holders have been filled, a winding machine is used to wind the coil surrounding the petroleum jelly sample. Finally, to ensure a permanent and low resistance connection between the serial inductor coil and the capacitor, an eye is soldered to the inner conductor using an ultrasonic soldering iron. The serial conductor wire is then soldered to this same eye.

After being assembled, the resonant frequency of each pNMR probe is tuned to 61.79 MHz, the Larmor precession frequency of protons in the $g-2$ experiment's 1.45 T magnetic field. The impedance of each probe is tuned to 50Ω. A network analyzer is used for both of these tuning procedures. After tuning, every pNMR probe is catalogued in an online database in order to track the individual probe characteristics.

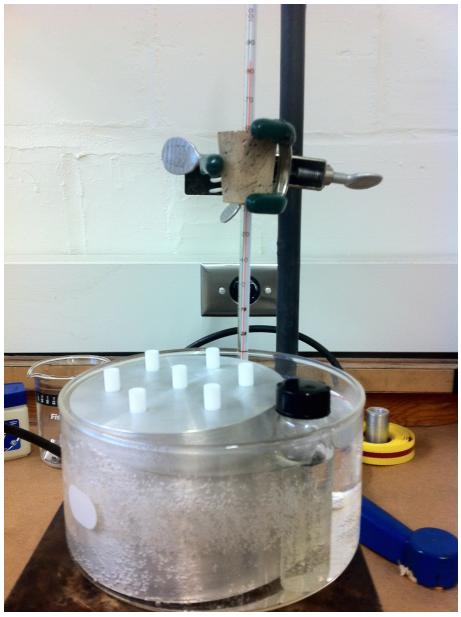

Figure 3.4 – To fill the teflon sample holders of the pNMR probes with petroleum jelly, the sample holders are placed in an aluminum block and warmed in a 90 °C water bath. With the holders warm, the petroleum jelly is melted in the same bath. Filling warmed sample holders with melted petroleum jelly both makes the filling procedure simple and minimizes the risk of air bubble formation. Image credit: [62]

Trolley and Fixed Probe Systems

The magnetic field in the muon storage region is mapped by an array of 17 pNMR probes every three days. The probes and their associated electronics are housed in what is known as the "trolley". This array contains one center probe, an inner ring of four probes at a radius of 1.75 cm, and an outer ring of twelve probes at a radius of 3.50 cm. The relative positions of the trolley pNMR probes are illustrated in Fig. 3.5a. The trolley rides on rails within the vacuum chambers and is centered at the nominal muon beam radial and vertical positions. While muons are present in the storage ring, the trolley is parked outside of the storage region in a "garage."

The trolley is pulled around the storage ring azimuth in vacuum using a fishing line in one direction and a signal cable in the other. The trolley's azimuthal position is tracked using two methods. The first method monitors the encoder counts of the motors used to pull the trolley. The second method relies upon a series of barcode markings printed on the bottoms of the vacuum chambers. A "barcode reader" detects the markings and the unique patterns are used to determine the trolley's location. When the trolley encounters regions of the storage ring where it experiences increased friction, there is an increased force in the pulling cable. The encoders interpret this increased tension as trolley motion, even when the trolley is stationary. Using the barcode markings is therefore a more robust position determination method.

Due to the fact that the trolley can not be present in the muon storage region at the same time as muons, a second set of pNMR probes is used to constantly monitor the evolution of the magnetic field. A suite of 378 probes, known as the "fixed probes," is embedded in grooves in the outer walls of the vacuum chambers, as shown in Fig. 3.5b. Fixed probes are located at 72 azimuthal locations, or "stations", evenly spread around the magnetic storage ring with either four or six pNMR probes per station (two or three probes each on both the top and bottom of the vacuum chambers). Fig. 3.6 shows the azimuthal distribution of the fixed probes. The probes within each station have a radial separation of 3 cm, with

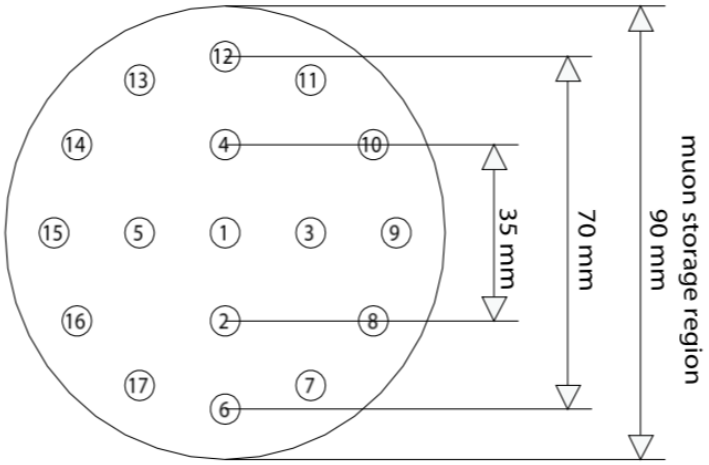

(a) Trolley pNMR probe array.

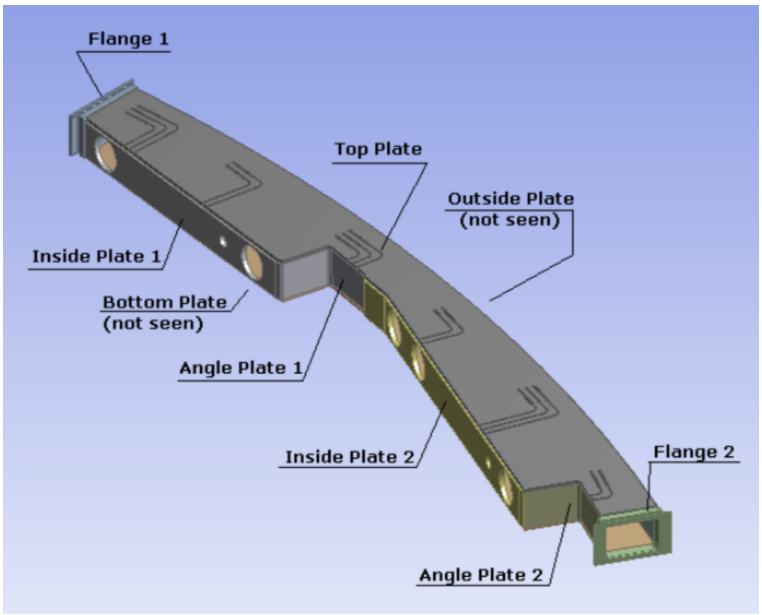

(b) Fixed probes grooves on the top of a vacuum chamber.

Figure 3.5 – The trolley holds an array of 17 pNMR probes at three different radii (a). It is pulled through the muon storage region every three days. The fixed probes are a suite of 378 pNMR probes embedded in grooves on the tops and bottoms of the vacuum chambers (b). The fixed probes constantly monitor the evolution of the magnetic field. Image credit: [10]

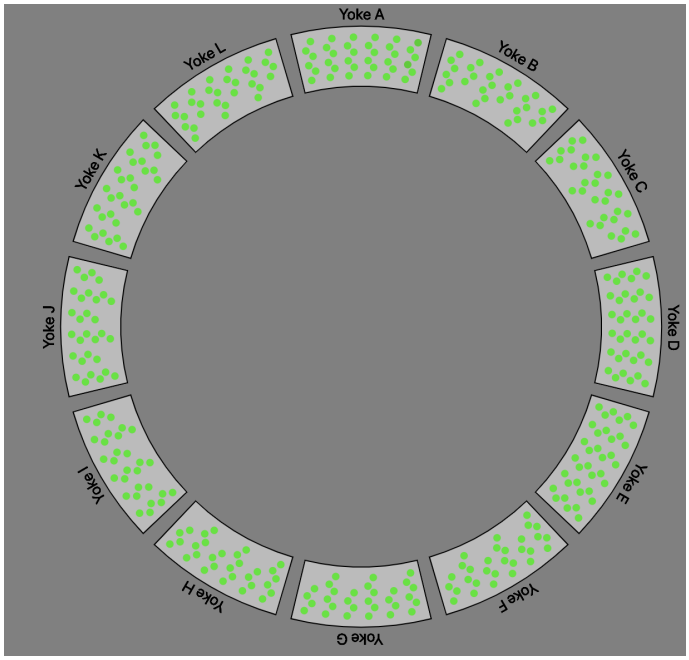

Figure 3.6 – Fixed probes are located at 72 azimuthal locations around the storage ring. Each location contains either four or six pNMR probes.

the middle probe centered radially on the ideal muon storage radius. They are located at vertical positions of $\pm 7.71\,\text{cm}$ with respect to the muon beam storage region mid-plane.

Each fixed probe makes a measurement every 1.7 seconds at all times when the magnetic field is on, whether the trolley is parked in its garage or is being pulled through the muon storage region. When the trolley is being pulled through the storage region, each trolley probe makes two measurements per second. Details on tracking the magnetic field evolution between trolley runs using the fixed probes are presented in Ch. 6.

3.4.2 Plunging Probe

Frequencies extracted from the FIDs of the previously discussed pNMR probes are the Larmor precession frequencies of protons in petroleum jelly. However, what is needed for the extraction of a_μ is the precession frequency of free protons. A "plunging probe" was de-

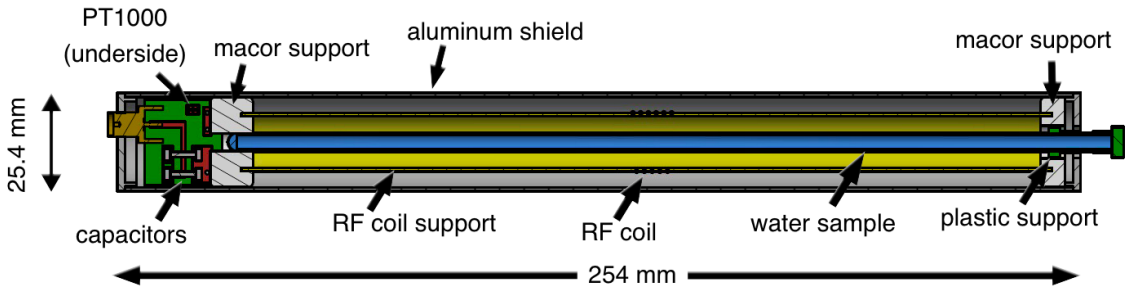

(a) Plunging probe design.

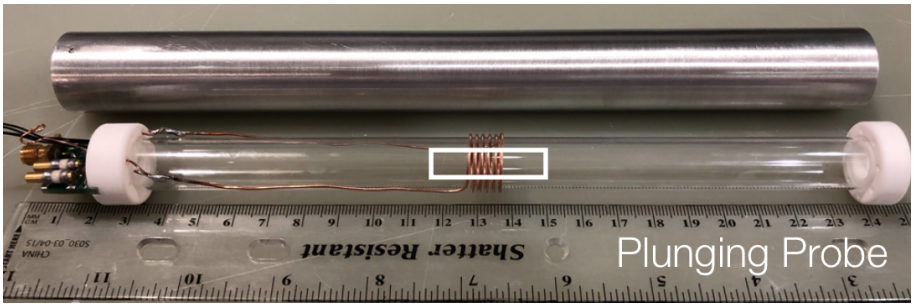

(b) Plunging probe.

Figure 3.7 – The plunging probe is a pNMR probe whose magnetic characteristics are well understood. It uses a cylindrical sample of water as the proton source. The plunging probe is used to calibrate the trolley probes, such that measured precession frequencies of protons in petroleum jelly can be related to the equivalent frequencies of free protons in the same magnetic field. Image credit: [63]

signed by David Flay (UMass Amherst) to calibrate the trolley pNMR probes. It is used to convert Larmor precession frequencies extracted from petroleum jelly pNMR probe FIDs to free proton frequencies [50]. The plunging probe is pictured in Fig. 3.7.

The plunging probe uses water as its proton source, with the bare proton precession frequencies getting masked by multiple sources. This masking requires corrections to the

measured signals as follows [10, 50, 64]:

$$\omega_p^{meas} = \omega_p^{free}\left(1 - \sigma(H_2O, T) - \left(\epsilon - \frac{4\pi}{3}\right)\chi(H_2O, T) - \delta_m\right). \tag{3.8}$$

In this equation, $\sigma(H_2O, T)$ is the effect of the diamagnetic shielding of protons by the electrons in the water molecules. This effect has been measured by Neronov and Seregin, as well as by Phillips et al [65, 66], and is given as a function of temperature as

$$\sigma\left(H_2O, T\right) = [25680.0(2.5) + 10.36(30) \times (T - 25\,^{\circ}\mathrm{C})] \times 10^{-9}. \tag{3.9}$$

This is a 25 ppm effect for the $g - 2$ magnetic field measurement. The $\chi(H_2O, T)$ term corrects for the bulk susceptibility of the water sample, including shape dependent effects. The plunging probe uses a cylindrical sample holder with a 5 mm outer diameter, for which $\epsilon = 2\pi$ (this factor assumes an infinite cylinder, a good approximation in the case of the plunging probe) [1]. The temperature dependence of the susceptibility of water has been measured by Blott and Daniell [67] and is given by

$$\chi\left(H_2O, T\right) = \chi\left(H_2O, 20\,^{\circ}\mathrm{C}\right) \times [1 + a_1(T - 20\,^{\circ}\mathrm{C}) + a_2(T - 20\,^{\circ}\mathrm{C})^2 + a_3(T - 20\,^{\circ}\mathrm{C})^3], \tag{3.10}$$

where $\chi\left(H_2O, 20\,^{\circ}\mathrm{C}\right) = -720(3) \times 10^{-9}$, and the a_i terms have values $a_1 = 1.3881 \times 10^{-4}/^{\circ}\mathrm{C}$, $a_2 = -1.2684 \times 10^{-7}/^{\circ}\mathrm{C}^2$, and $a_3 = 8.09 \times 10^{-10}/^{\circ}\mathrm{C}^3$. Finally, δ_m is the effect due to the magnetization of the probe materials which perturb the magnetic field at the site of the sample. This effect has been carefully measured for the plunging probe, as described in [68].

With the relationship between the precession frequency extracted from a plunging probe measurement and the precession frequency of a free proton well understood, the plunging probe can be used to calibrate the trolley pNMR probes. The relationship between the precession frequency of a free proton and the precession frequency of a proton in petroleum jelly does not need to be well known.

3.5 Trolley Probe Calibration

Each trolley probe must be separately calibrated in order to understand the magnetic field experienced by muons as measured by free protons. The calibration principle is simple: the

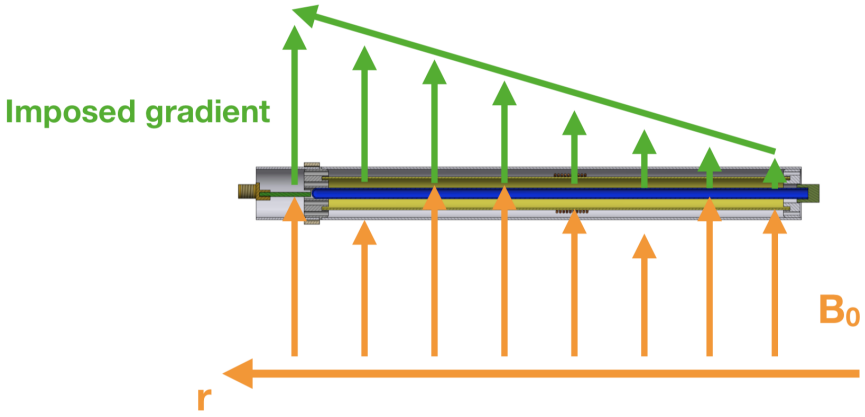

Figure 3.8 – To calibrate a particular trolley probe, the plunging probe and the trolley probe must make measurements at the same location, to within approximately 2 mm in all directions. Measurements taken with and without applied, well-known magnetic field gradients are compared in order to locate the probes. This is known as the "Delta-B" method. Image credit: [63]

plunging probe, whose magnetic field measurements are related to those of a sample of free protons by Eq. 3.8, is brought to the location of each trolley probe and the differences in the measurements of the two types of pNMR probes are calculated.

A method known as the "Delta-B" method is used to align the plunging probe with each trolley probe. To determine the location of a given probe, known linear gradients are individually applied in all three coordinate directions[3] using a set of current carrying coils[4]. By comparing the differences in measured magnetic field values with these gradients turned on and off, the probe in question can be located in the dimension being studied [68]. The Delta-B principle is pictured in Fig. 3.8, with the plunging probe used as a reference.

The first step in calibrating an individual trolley probe is determining its location using Delta-B measurements in the three coordinate directions. This is done at a specific

[3]A gradient of 40 Hz/mm is used in the transverse directions, while 10 Hz/mm is used in the azimuthal direction.

[4]The coils used are known as surface coils. They are described in Sec. 4.5.1.

azimuthal location in the magnetic storage ring where the magnetic field has been made extremely homogeneous. With the trolley probe position known, the trolley is moved out of the calibration region and the plunging probe is moved to approximately the same location. The same three Delta-B measurements are then taken. The plunging probe location is systematically adjusted until all three of its Delta-B measurements are within 20 Hz of the trolley probe's measurements. This amounts to a physical alignment of the two systems to approximately 1-2 mm in all three directions [68].

Once the trolley probe and plunging probe can be reliably positioned at the same location, a sequence of alternating measurements is taken in quick succession. After taking a trolley measurement, the trolley is moved azimuthally out of the calibration region and the plunging probe is moved to the calibration position. After a plunging probe measurement has been made, the plunging probe is retracted and the trolley is moved back to the calibration position for another measurement. A single swap sequence, defined as making one measurement with each type of probe, takes six minutes. The swapping sequence is repeated 10 times per trolley probe.

The trolley must be moved away from the calibration position not only so that the plunging probe can be inserted, but also because the trolley has a magnetic footprint that would perturb the magnetic field measured by the plunging probe were it too close[5]. A dedicated study showed that if the trolley is moved 4° (50 cm) away from the calibration position, its magnetic footprint is no longer visible to the plunging probe.

Calibration of the 17 trolley probes was first undertaken in July 2018. Preliminary results are presented in [69]. A second round of calibration measurements was started in February 2019, but not all trolley probes were calibrated at this time. The remaining probes were calibrated in July 2019. Ideally, the calibration procedure should be done both before and after every data taking run. The July 2018 calibration results are used in the analysis presented in Ch. 6, where for each trolley probe, the calculated calibration offset is individually applied

[5]The trolley magnetic footprint is discussed in Ch. 6.

to each trolley probe measurement. The fixed probes are calibrated to trolley measurements, so individual fixed probes are not calibrated directly to the plunging probe.

An alternative calibration probe which uses ^{3}He to provide a spin sample is used for verification. The motivation for a cross check with a different probe is that ^{3}He has different systematics than water as an NMR sample. The diamagnetic shielding term is larger for ^{3}He than water, but is known with four times better precision and has a smaller temperature dependence. The magnetic susceptibility of ^{3}He is also smaller than that of water, and because of its gaseous form, the associated correction is less sensitive to the sample shape. Details of the ^{3}He probe cross-calibration are presented in [51].

3.6 Magnetic Field Multipole Expansion

A 2D multipole expansion is used to discuss the uniformity of the magnetic field in the muon storage region, the same as was done in the Brookhaven experiment [9]. During a trolley run, magnetic field measurements are taken at over 7000 azimuthal locations. A frequency is extracted from the FID of each trolley probe from each measurement (or "event"), and the calibration correction is applied. The calibrated frequencies are fit to a function of the form

$$B(r,\theta) = B_0 + \sum_{n=1}^{N} \left(\frac{r}{r_0}\right)^n [a_n \cos(n\theta) + b_n \sin(n\theta)], \tag{3.11}$$

where B_0 is referred to as the dipole magnetic field component, the a_n values as normal multipole components, and the b_n values as skew multipole components. The multipoles are normalized to $r_0 = 4.5\,\text{cm}$, the edge of the muon storage region. The multipole components through $n = 4$, besides the dipole component which is a constant vertical magnetic field, are graphically represented in Fig. 3.9. $n = 1$ terms are referred to as quadrupole terms, $n = 2$ terms as sextupole terms, $n = 3$ terms as octupole terms, and $n = 4$ terms as decupole terms. For the remainder of this document, the magnetic field will be discussed in terms of the amplitudes (the a_n and b_n values) of these magnetic field multipole moments.

The magnetic field experienced by the muon beam in the $g-2$ magnetic storage ring is

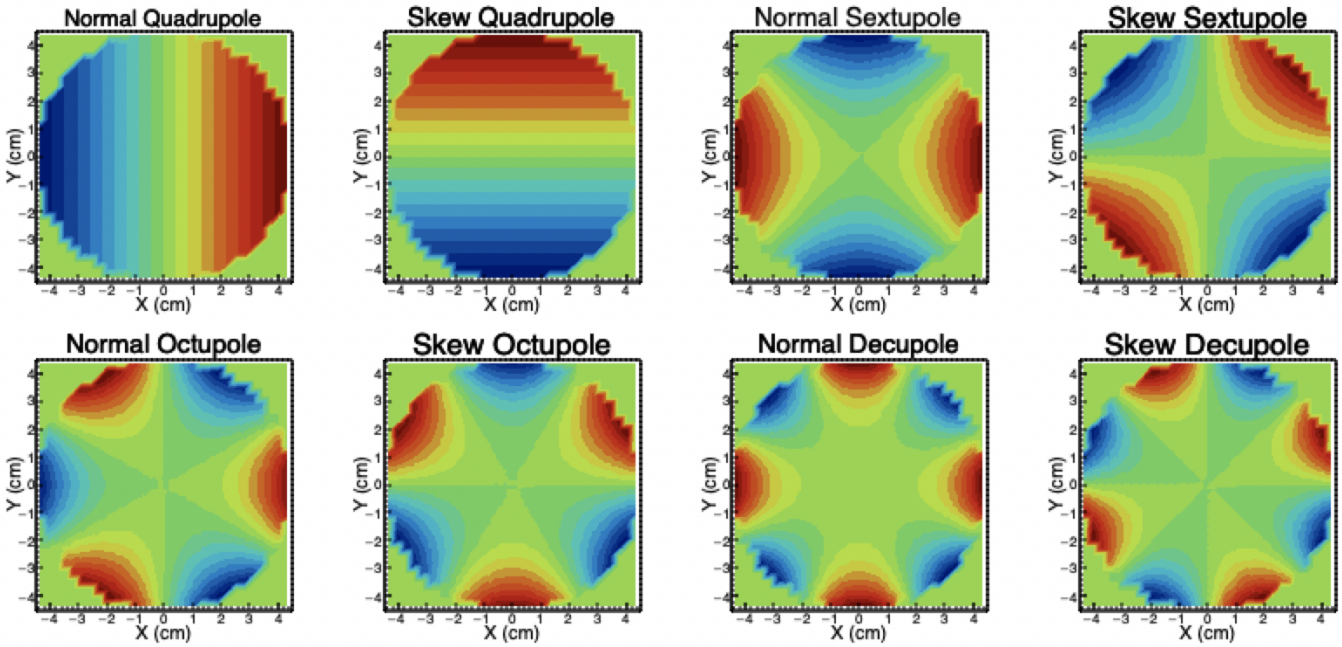

Figure 3.9 – Graphical representations of the first eight magnetic field multipole components described by Eq. 3.11. Color scale in arbitrary units.

not simply two-dimensional, but rather is a three-dimensional magnetic field. The differences between a 2D and 3D multipole expansion have been studied [70]. A toroidal expansion of the three-dimensional magnetic field has also been explored [71]. A 3D multipole expansion of the magnetic field has not yet been included in any Fermilab magnetic field analyses, but incorporating one presents a unique improvement that could be made by future analyses.

3.7 Magnetic Field-Muon Beam Convolution

The final value of ω_p required for the extraction of a_μ is not simply the average magnetic field experienced by muons as measured by free protons, but rather the measured magnetic field weighted by the muon beam distribution. Simply put, the average magnetic field experienced by stored muons is required. The muon beam distribution is reconstructed using the tracking detectors[6]. Letting $M(\vec{r}, t)$ represent the muon beam distribution as a function of space and time, the muon-weighted free proton precession frequency is calculated as

$$\widetilde{\omega_p} = \iint M(\vec{r}, t)\omega_p(\vec{r}, t)dtdV, \tag{3.12}$$

where the magnetic field as a function of time ($\omega_p(\vec{r}, t)$) is determined using fixed probe tracking, discussed in Ch. 6.

The timescale over which this convolution should be done has not yet been determined. One consideration includes a balance between increasing the resolution of the magnetic field measurements (by averaging together data) while still retaining information about real magnetic field changes. A similar consideration must be taken into account for ω_a data, while also considering the statistical impact that a longer data taking period has on the ω_a measurement.

[6]Details of the tracking detectors and how they are used to reconstruct the muon beam distribution can be found in [46].

Chapter 4

MAGNETIC FIELD SHIMMING

4.1 Magnetic Field Shimming Introduction

One of the first activities that took place after the magnetic storage ring was assembled at Fermilab was the process of shimming the magnetic field. In this context shimming refers to fine-tuning the magnetic field in the muon storage region, both to make it uniform as a function of azimuth and to make the cross-sectional magnetic field distribution at all azimuthal locations homogeneous. Both types of homogeneity are important in minimizing the uncertainty in magnetic field tracking.

Shimming consists of two distinct phases. Passive shimming, which took place from October 2015-September 2016, involved the precise adjustment of thousands of pieces of ferrous and nonferrous material in and around the muon storage region. Active shimming involves the setting and monitoring of 200 concentric current-carrying wires sitting on the pole faces, which are continuously active when the magnet is powered. A cross-sectional view of the storage ring magnet with many shimming "toolbox" elements labeled is depicted in Fig. 4.1. It is reproduced here from Fig. 2.2. The mechanical design includes various adjustable components which can be used to locally tune the magnetic field multipole components introduced in Sec. 3.6. The effects of these adjustable knobs were first simulated and calibrated by the Brookhaven magnetic field team [72, 73, 74, 75, 76]. The Fermilab magnetic field team repeated this process of simulation and calibration. Individual components are discussed in the following subsections.

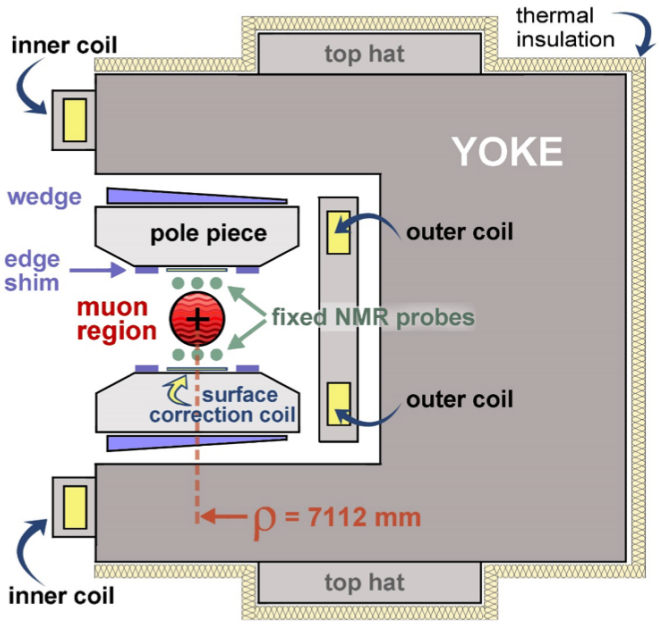

Figure 4.1 – A cross-sectional illustration of the $g-2$ storage ring magnet, highlighting various elements of the passive shimming "toolbox." The image is reproduced here from Fig. 2.2. Ultra-low-carbon steel pole pieces sit in the opening of the C-shaped outer steel yoke. Wedge shims sit between the poles and the yokes, while surface correction coils sit on the pole faces. Image credit: [40]

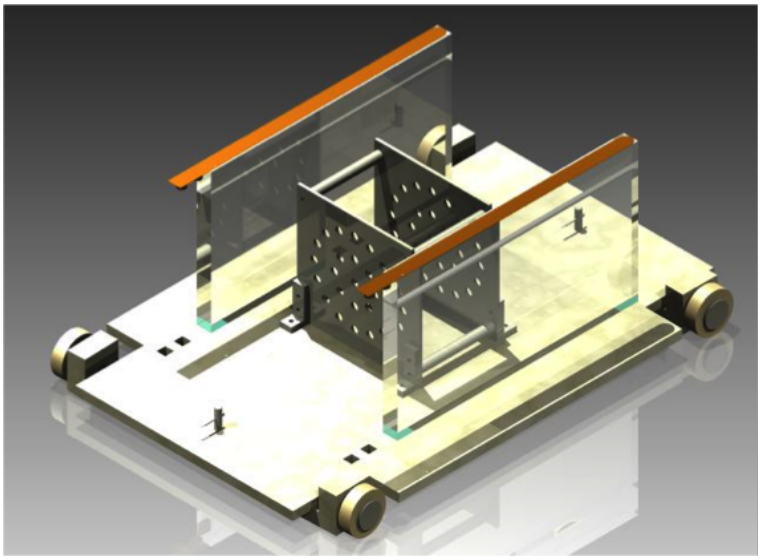

Figure 4.2 – A special shimming trolley was used to make magnetic field measurements during the rough shimming period of the Fermilab experiment. The trolley holds a matrix of 25 pNMR probes and is equipped with capacitive sensors (orange strips). Image credit: [77]

4.2 Shimming Measurement Tools

4.2.1 Shimming Trolley

During the rough shimming period, before vacuum chamber installation, measurements of the magnetic field in the muon storage region were made using a "shimming trolley" that was pulled along the bottom pole surfaces [10]. Designed by Brendan Kiburg (Fermilab), it is pictured in Fig. 4.2. The shimming trolley was designed to be completely non-magnetic, so that it does not affect any magnetic field measurements. The cart is built out of PEEK, chosen for its strength and non-magnetic properties, and the wheels are plastic ball bearings with glass balls.

The shimming trolley holds a matrix of 25 pNMR probes at radii of 0 cm (1 probe), 2.25 cm (8 probes), and 4.5 cm (16 probes) with respect to the central muon beam orbit. The probe matrix is pictured in Fig. 4.3. During the assembly process, the end caps of the

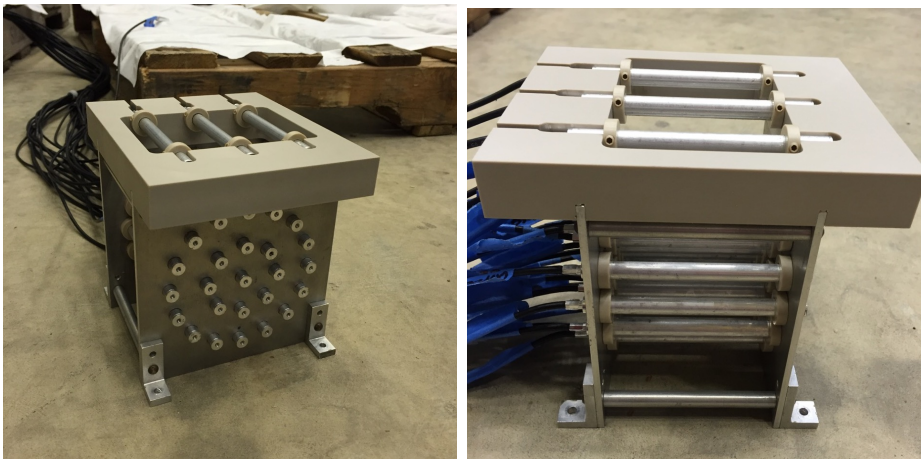

(a) Front view. (b) Side view.

Figure 4.3 – 25 pNMR probes are mounted in a matrix affixed to the shimming trolley. The probes were aligned using an alignment plate and are held in place by PEEK rings and set screws to ensure that the centers of the petroleum jelly samples remain in the same plane. Three pNMR probes are mounted to the top of the matrix, at the radial and vertical locations of the fixed probes.

probes were aligned with an alignment plate. The probes are held in place with PEEK rings and set screws to ensure that the centers of the 25 petroleum jelly samples remain in the same transverse plane.

The shimming trolley is also equipped with four Capacitec 4100-SL capacitive sensors [78]. The sensors are mounted to the tops and bottoms of two quartz plates at the inner and outer cart radii. They were used to measure both the individual pole shapes and the shape of the gap between the top and bottom pole surfaces with 70 nm resolution and a few micron reproducibility.

Similar to the trolley discussed in Sec. 3.4.1, the shimming trolley could be pulled around the full 360° of the storage ring magnet. Because the vacuum chambers were not yet installed in the magnet gap at the time of rough shimming, a stepper motor was used to pull the

shimming trolley around the storage ring. The magnetic stepper motor was mounted on a vertical arm attached to a non-magnetic table which sat in the center of the storage ring, thereby moving the motor more than 1.5 m away from the muon storage region. Fishing line wound around a pulley in the magnet gap connected the shimming trolley to the motor.

The stepper motor had the ability to pull the shimming trolley around the storage ring with varying step sizes. For a typical magnetic field scan, a step size of 5 mm was used. When aiming to understand magnetic field features present in a specific region of the storage ring, a step size of 1 mm was used. The smaller step size gave better resolution on the magnetic field shape. The trolley's azimuthal location, height, and radial position were tracked using a laser tracker located at the center of the storage ring in conjunction with four retroreflectors attached to the inner quartz plate (not pictured in Fig. 4.2).

4.2.2 Tilt Measurements

The shapes of individual pole pieces and the relative alignment of the top and bottom pole pieces have a large effect on the local magnetic field strength. The shape and alignment of all 72 poles pieces were measured using electrolytic tilt sensors mounted on a platform machined from a single piece of aluminum to ensure parallelism of the faces. The platform, pictured in Fig. 4.4, uses a 3-point contact system with two sets of three ceramic balls located on the base of the platform and on rods machined onto the platform. Balls 1 and 2 are separated by 11.75 inches. Ball 3 is centered between the other two, offset by 2.25 inches. A pair of electrolytic tilt sensors are mounted to the center of the platform, oriented to measure tilt in the radial and azimuthal directions. The two Fredericks Co. 0719-3701-99 tilt sensors are read out with a Fredericks Co. 1-6200-012 signal conditioning board [79].

Small pieces of shim material of known thickness were inserted under two of the ceramic balls to calibrate the responses of the tilt sensors. Shims inserted under ball 1 affected both the radial and azimuthal tilts of the platform, while shims inserted under ball 3 affected only the azimuthal tilt. Shim thicknesses up to 10 mils were used, corresponding to tilts of up to 0.25°. For each trial, the tilt sensor output bits were recorded and plotted as a

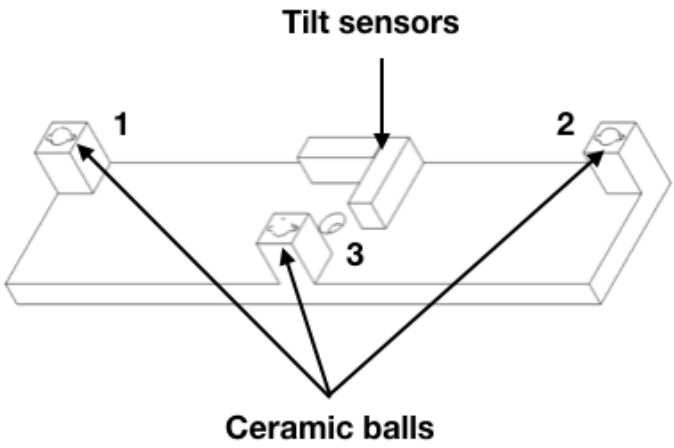

Figure 4.4 – Two electrolytic tilt sensors are used to measure the tilts of the poles in both the radial and azimuthal directions. Three balls in the base of the measurement platform and three on the tops of rods on the platform form a 3-point contact system for both bottom and top pole tilt measurements. Image credit: [61]

function of expected tilt. The data were fit to a linear line whose slope corresponds to the bits/degree calibration necessary to interpret tilt measurements. Two example calibration plots are shown in Fig. 4.5. The tilt sensors are quoted to have a linear response within a range of $\pm 0.25^{\circ}$. The outlier point in the azimuthal tilt plot is on the edge of this range and was not included in the fit. Due to the experimental setup, more shim material was required to change the radial tilt of the platform than the azimuthal tilt. The platform became unstable at the largest tested tilt. This point was not included in the fit of the radial tilt sensor calibration data.

4.3 Initial Magnetic Field

The magnetic storage ring was first powered at Fermilab on September 22, 2015. Shortly thereafter, the magnetic field team began commissioning the shimming trolley. On October 14, the magnetic field in the full 360° of the muon storage region was measured for the first

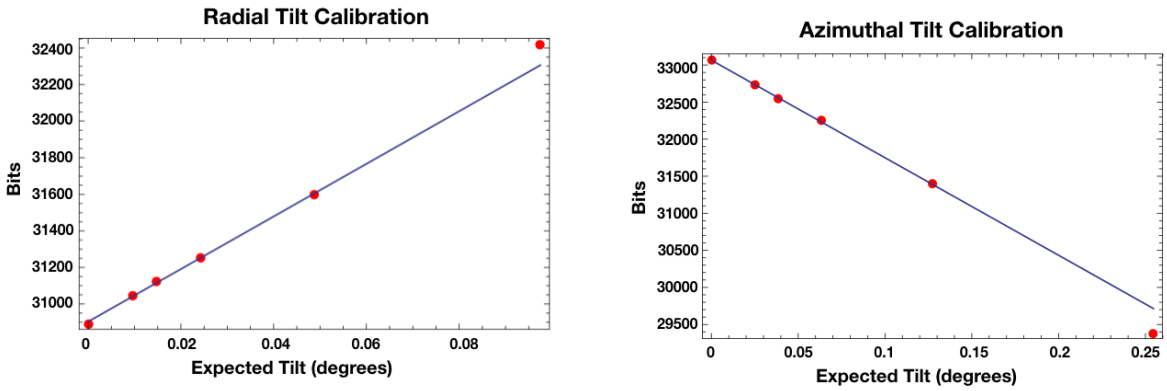

(a) Radial tilt calibration.

(b) Azimuthal tilt calibration.

Figure 4.5 – Shims of varying thicknesses were placed underneath the bottom ceramic balls of the tilt sensor platform to calibrate the tilt sensors. A calibration value in bits/degree was extracted for both the radial and azimuthal tilt sensors by fitting a plot of expected tilt vs. tilt sensor readout to a linear line.

time. Fig. 4.6 shows both the dipole magnetic field component as a function of azimuthal position and the azimuthally averaged magnetic field as a function of x and y (computed from the individual $x - y$ slices at each azimuthal measurement location) from this first measurement. The amplitudes of the azimuthally averaged magnetic field multipole moments are listed in Tab. 4.1. The dipole component varied by ± 700 ppm and the azimuthally averaged magnetic field showed a large normal quadrupole component. This can be compared to the fully shimmed Brookhaven magnetic field, pictured in Fig. 4.7. The dipole magnetic field component varied by ± 50 ppm and all azimuthally averaged multipole components had amplitudes at the 1 ppm level [9]. In the process of disassembling the storage ring magnet, transporting it from Brookhaven National Laboratory to Fermilab, and reassembling it, the magnet was not put together in exactly the same way. The Fermilab shimming team was not able to build upon the Brookhaven shimming efforts, but rather had to begin anew, starting with passive shimming.

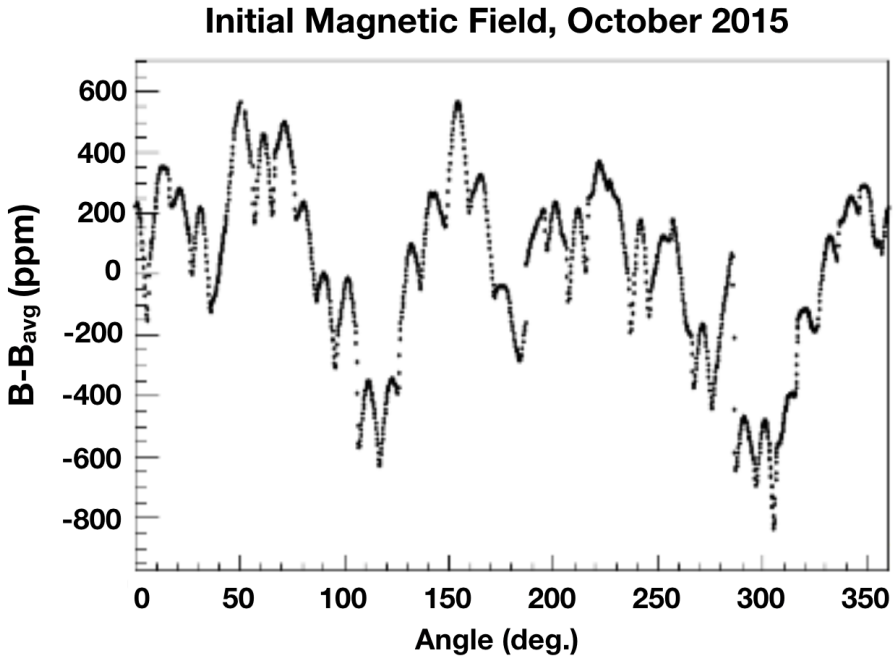

(a) Dipole magnetic field component vs azimuth.

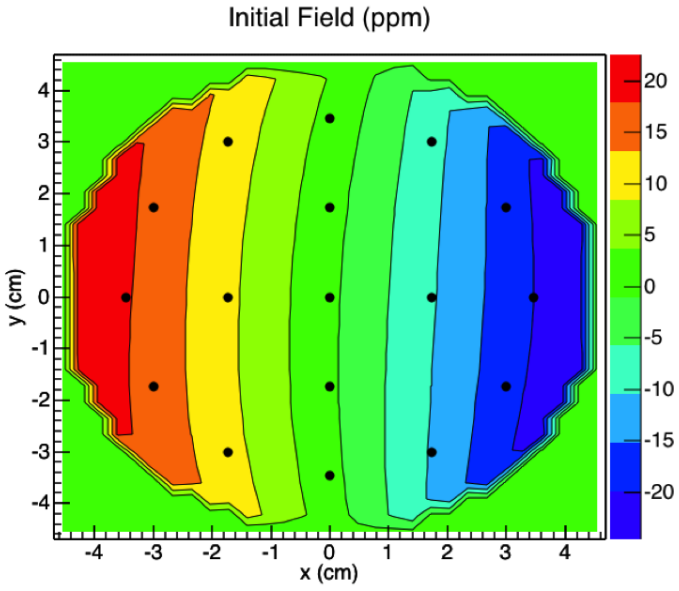

(b) Azimuthally averaged magnetic field as a function of x and y.

Figure 4.6 – The first shimming trolley measurement was made on October 14, 2015. The amplitude of the dipole magnetic field component is shown as a function of azimuthal location in (a). The azimuthally averaged magnetic field in the muon storage region is shown in (b). The amplitude of the dipole component varied by ±700 ppm while a large normal quadrupole magnetic field component is visible in the azimuthally averaged magnetic field.

Multipole	Normal component amplitude (ppm)	Skew component amplitude (ppm)
Quadrupole	-25.4	1.09
Sextupole	-1.81	0.35
Octupole	0.98	-0.13
Decupole	0.90	-0.42

Table 4.1 – Amplitudes of the azimuthally averaged magnetic field multipole components from the first shimming trolley measurement taken on October 14, 2015.

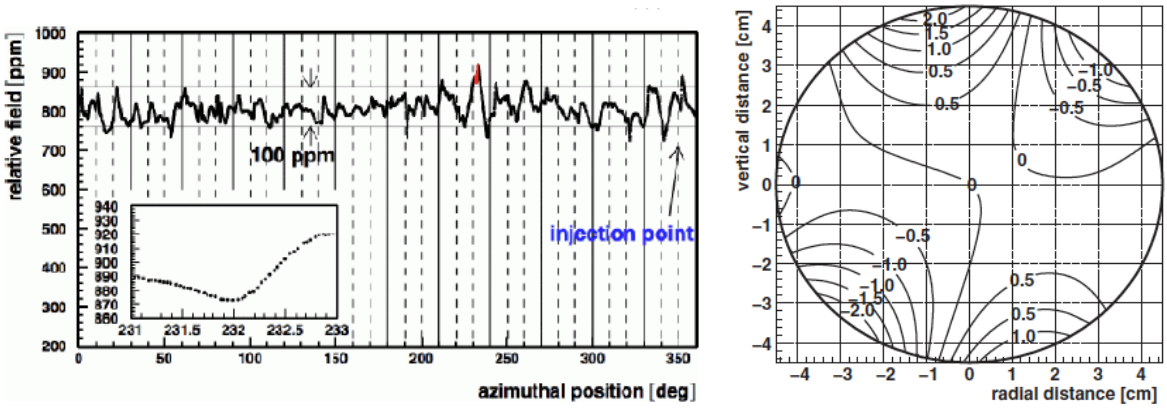

(a) Dipole vs azimuth.

(b) Azimuthally averaged magnetic field.

Figure 4.7 – The fully shimmed Brookhaven magnetic field. The amplitude of the dipole magnetic field component varied by ±50 ppm in azimuth (a) while the azimuthally averaged magnetic field (b) contained variations up to ±2 ppm. Image credit: [9]

4.4 Passive Shimming

The process of passive shimming, which relied heavily on the work of the Brookhaven magnetic field shimming team [72, 73, 74, 75, 76], included the adjustment and addition of over 10,000 pieces of ferrous and nonferrous material near the muon storage region. The goal of passive shimming was to reduce the azimuthal variations of the magnetic field multipole components. The components discussed below are all depicted in Fig. 4.1. Passive shimming adjustments were calculated by Matthias Smith [58], while the author took a leading role in the implementation of the recommendations.

4.4.1 Top Hats

Top hats are the largest shims with the most far reaching effect of all shims available for use during passive shimming. They are 15° long pieces of steel which are bolted to the tops and bottoms of the yokes. Strips of G10, up to 2 mm thick, were either added to or removed from the gap between the yokes and the top hats. The effect of adding one such strip is shown in Fig. 4.8, showing the large azimuthal extent (±50°) of the effect on the strength of the dipole magnetic field component.

4.4.2 Pole Pieces and Pole Feet

The pole pieces are 10° long segments of iron located above and below the muon storage region. There are six pole pieces per yoke segment, three each on top and bottom. Each pole is held to the yoke by four bolts and sits on either eight or ten pole feet. Thin pieces of material (iron, aluminum, or bronze), ranging in thickness from 0.25-10 mils, sit between each pole and its pole feet and help orient and flatten the pole face. Fig. 4.9 shows a graphical representation of the the shims between a pole and a pole foot.

The shapes of the pole pieces affect the strengths of both the dipole and normal quadrupole magnetic field components. The size of the air gap between the upper and lower pole faces at any location is the main factor in determining the strength of the dipole magnetic field

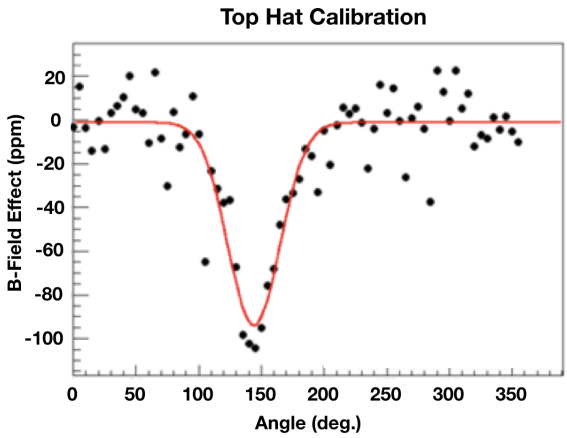

Figure 4.8 – Changing the air gap between a top hat and a yoke affects the amplitude of the dipole magnetic field component over a large azimuthal extent (±50°). The effect due to the insertion of a G10 shim under a top hat at 150° is pictured as a function of azimuthal location. Plot credit: [58]

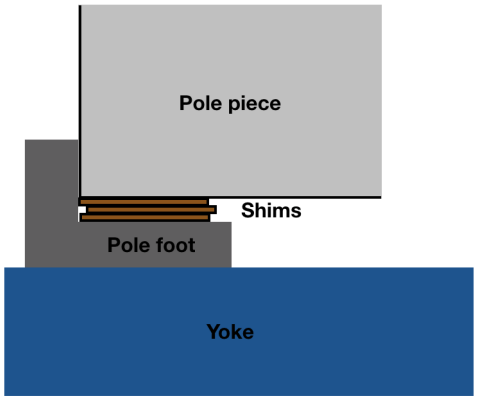

Figure 4.9 – 10° long pole pieces, bolted to the magnet yoke, sandwich the muon storage region. Pole feet sit between the poles and the yoke, and sandwich thousandths of an inch thick shims which orient and flatten the pole pieces.

component at that location. A relative tilt between the top and bottom pole faces creates a normal quadrupole magnetic field component, a linear variation in magnetic field strength as a function of radial position [80]. Using input from tilt sensor measurements taken across the pole surfaces, the shims between the poles and the pole feet were adjusted to both flatten the pole faces and to ensure that the bottom and top pole faces are parallel to one another. This adjustment allowed for alterations of the planes of the pole pieces of up to 200 µm, with a precision of 5 µm. The pole face smoothness was verified post-shimming using both the capacitive sensors mounted on the shimming trolley and the tilt sensors. The pole foot adjustments were completed over an almost three month long period in early 2016.

4.4.3 Wedge Shims

Wedge shims are 10 cm wide, 53 cm long, wedge shaped pieces of steel that are thicker at the outer radius than inner. They sit between the poles and the yokes, as shown in Fig. 4.10a. They can be moved in the radial direction over a distance of 18 mm. Changing the radial position of a wedge shim has the largest effect on the strength of the dipole magnetic field component, because the change in position causes more/less iron to be present at a given radius. The effect has an approximately gaussian shape that is centered at the azimuthal location of the wedge shim and extends over a range of $\pm 10°$. Changing the radial position of a wedge shim also causes a smaller change in the strength of the local normal quadrupole magnetic field component [81].

Various configurations were used to calibrate the effects of changing the radial position of a wedge shim. To begin, all wedges in a pole were aligned at the center of their range of motion and a magnetic field measurement was taken with the shimming trolley. One (or multiple) wedges would then be moved radially into or out of the storage region by a known amount, and the magnetic field would be rescanned. The difference in the magnetic field, shown in Fig. 4.10b for moving one wedge shim, was used as a calibration.

Positioning the wedge shims was an iterative process. To begin, the magnetic field was measured as a function of azimuth. This measurement served as input to an optimization

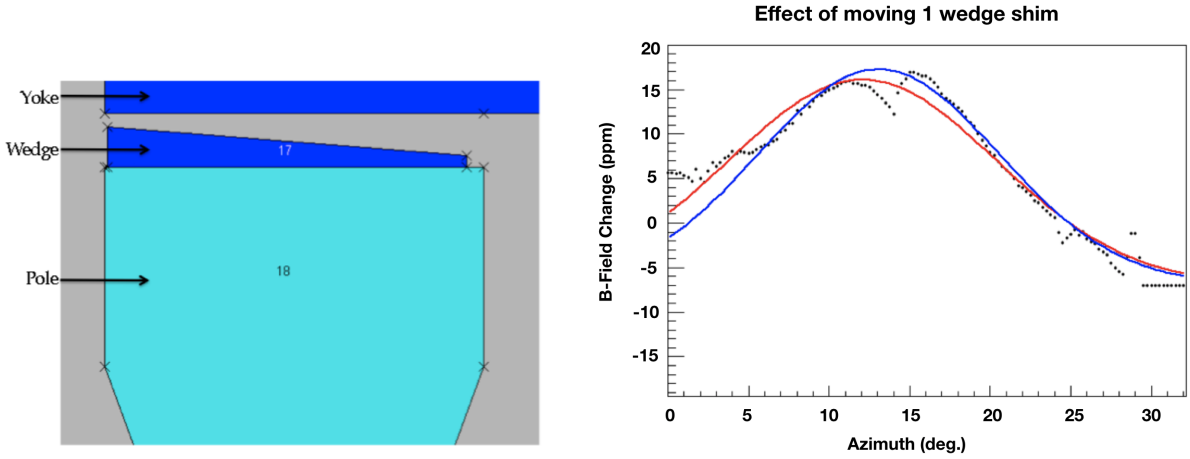

(a) Wedge shim.

(b) Wedge shim calibration.

Figure 4.10 – 10 cm wide wedge shaped pieces of iron known as wedge shims sit between the pole pieces and the yoke, as shown in (a). Their radial positions, which can be varied over an 18 mm range, affect the magnetic field strength over an azimuthal extent of ±10°. (b) shows the effect of moving one wedge shim as a function of azimuthal location, where the red and blue curves represent two different fits to the measured data. Image and plot credit: [10, 58]

program which provided recommendations for ideal wedge shim positions. After the radial positions of all wedge shims had been adjusted, the magnetic field was remeasured, providing new input to the optimization program. This process was repeated until the recommended changes caused immeasurably small improvements to the magnetic field uniformity.

4.4.4 Iron Foil Laminations

The final passive shimming tool, the one with the smallest azimuthal extent, is known as iron foil laminations. This idea was used in the Brookhaven experiment, but not to the same extent [82]. During the summer of 2016, over 8,000 four-inch long strips of 1 mil thick iron were arranged on the pole surfaces at three radial positions with a 0.244° spacing. The foils were each modeled as a collection of magnetic dipoles in order to determine the width of foil (or equivalently the weight of iron) to place at each location. The number of magnetic dipoles at each azimuthal and radial position was iteratively increased until the strengths of the higher order magnetic field multipole components were minimized [83].

For the production of the iron foil laminations, iron strips of varying width (mass) were laser cut and cleaned in an ultra-sonic bath. Each strip was weighed and sorted into groups by mass, thereby creating a catalogue of available strips. This method of manual histogramming utilized over 100 bins, with each bin containing iron foils within a 2% range of a mean mass.

The foils were taped to G10 sheets cut to the exact size and shape of the pole piece faces, which were then installed directly on the pole faces. After installation of the first G10 sheets, it was quickly found that the radially oriented iron foils caused intolerable magnetic field gradients across the sensitive volumes of the fixed probes, rendering the fixed probes unusable. This issue was circumvented by replacing the radially oriented iron foils at these azimuthal locations with azimuthally oriented thin iron strips. The thickness of the thin strips was determined based on the total mass of the four-inch long strips that were being replaced. The thin strips produce much smaller magnetic field gradients than the wider, four inch long strips and allow for good fixed probe performance. Fig. 4.11 shows a rendering of a G10 sheet with iron foils attached. After all of the iron foils for a pole face had been

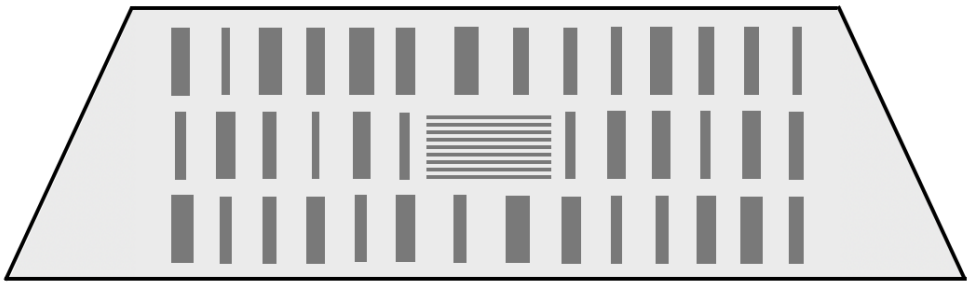

Figure 4.11 – Iron foil laminations consist of four inch long pieces of iron of varying widths arranged in three rows at different radial positions with a 0.244° azimuthal spacing. The radially oriented strips at fixed probe locations are replaced by thin, azimuthally oriented iron strips which produce much smaller magnetic field gradients. These laminations reduce the strengths of local higher order magnetic field multipole components.

attached to the G10 sheet, the sheet was epoxied to the pole surface.

4.4.5 Passive Shimming Results

After eight months of passive shimming, the magnetic field homogeneity in the muon storage region had been improved significantly. The azimuthal variations of the dipole component were reduced from ±700 ppm to ±25 ppm. The strengths of all azimuthally averaged higher order magnetic field multipole components, besides the skew octupole, were reduced to sub-ppm values. Final rough shimming magnetic field maps are shown in Fig. 4.12 and the strengths of the multipole components are listed in Tab. 4.2.

4.5 Active Shimming

At the end of the passive shimming period, the azimuthally averaged magnetic field variations were still above the final magnetic field uniformity goal. Nothing more could be done to reduce the azimuthal magnetic field variations with the built-in toolkit, but one tool remained

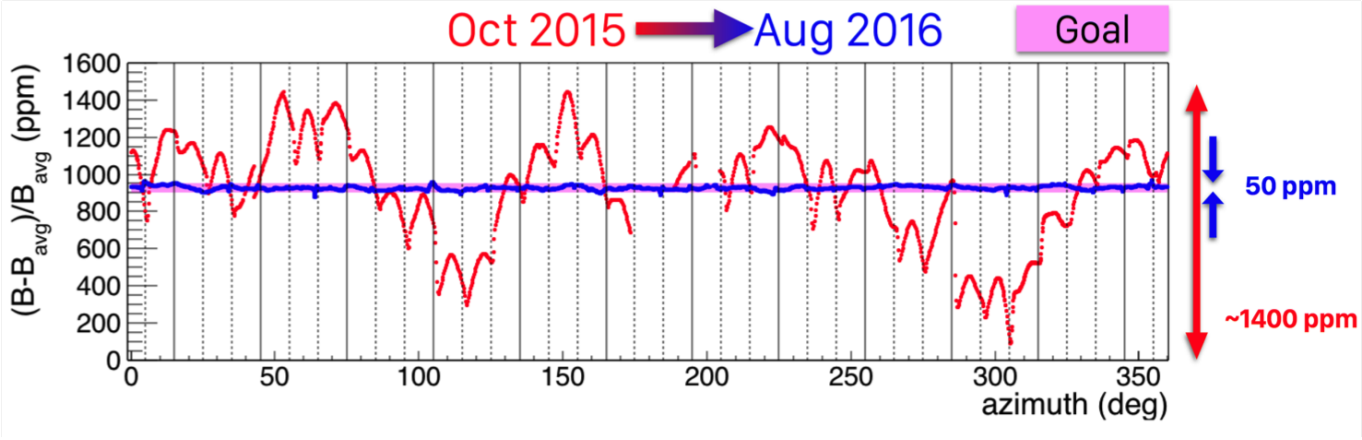

(a) Amplitudes of the pre- and post-rough shimming dipole magnetic field component vs azimuth.

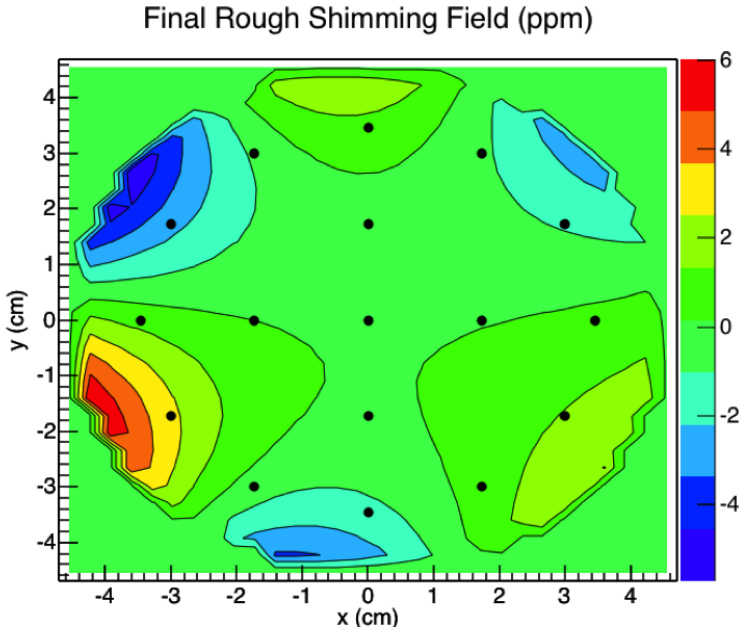

(b) Post-rough shimming azimuthally averaged magnetic field.

Figure 4.12 – Rough shimming reduced the azimuthal variations of the dipole magnetic field component from ±700 ppm to ±25 ppm, as shown in (a). The post-rough shimming azimuthally averaged magnetic field map is shown in (b). The amplitudes of all azimuthally averaged magnetic field multipole components, besides the skew octupole, were reduced to sub-ppm values.

Multipole	**Normal component amplitude (ppm)**	**Skew component amplitude (ppm)**
Quadrupole	0.02	-0.71
Sextupole	0.75	0.44
Octupole	-0.56	-3.77
Decupole	0.62	-1.61

Table 4.2 – Amplitudes of the azimuthally averaged magnetic field multipole components after rough shimming.

to minimize the amplitudes of the azimuthally averaged higher order magnetic field multipole components. The subsystem is known as the "surface coils". Additionally, the strength of the dipole magnetic field component is kept stable over time through a system known as power supply feedback.

4.5.1 Surface Coils

The surface coils are two sets of 100 concentric, current-carrying coils, located above and below the vacuum chambers. The coils sit on top of the iron foil laminations and have a radial spacing of 2.5 mm. The currents in the coils are controlled by driver boards, each of which controls four coils. Each current source can be adjusted within a range of ± 2.5 A. Different patterns of currents can be used to produce the various magnetic field multipole components.

To derive the current distributions which produce the different multipole components, one starts with Maxwell's equations (the derivation is reproduced here in full, with the different steps taken from a combination of sources [84, 85, 86, 87]). Specifically, one starts with the fact that in free space, with no current sources, the curl of a magnetic field is zero:

$$\vec{\nabla} \times \vec{B} = 0. \tag{4.1}$$

The magnetic field can therefore be written as the gradient of a scalar potential Ψ

$$\vec{B} = \vec{\nabla}\Psi, \tag{4.2}$$

where the potential can be generally expressed in cylindrical coordinates as

$$\Psi = A_n r^n \sin\left(n\theta + \alpha\right). \tag{4.3}$$

$\alpha = 0$ corresponds to normal magnetic field multipole components and $\alpha = \pi/2$ to skew components. Combining Eqns. 4.2 and 4.3, the magnetic field components in the the x (radial) and y (vertical) directions can be expressed as

$$B_x = \frac{\partial}{\partial x}\Psi = A_n n r^{n-1} \sin\left((n-1)\theta + \alpha\right) \tag{4.4}$$

and

$$B_y = \frac{\partial}{\partial y}\Psi = A_n n r^{n-1} \cos\left((n-1)\theta + \alpha\right). \tag{4.5}$$

Assuming that the pole pieces have a large (infinite) permeability, there is a boundary condition on the tangential magnetic field created by the surface coils

$$\hat{n} \times \vec{H} = \vec{K} \longrightarrow \mu_0 \vec{K} = \hat{n} \times \vec{B}, \tag{4.6}$$

where $\vec{K}$ is the current density and $\hat{n}$ is the direction normal to the pole surface. The surface coil currents are constrained to flow azimuthally, in the $\hat{z}$ direction. The vectors normal to the plane of the coils point in the $\pm\hat{y}$ direction, such that $\hat{n} = (0, \pm 1, 0)$. The current distributions associated with each magnetic field component can therefore be written as

$$\mu_0 K_z = -n_y B_x, \tag{4.7}$$

with $n_y = 1$ at the bottom pole and $n_y = -1$ at the top pole. Using Eq. 4.4 and ignoring overall constants, the magnetic field multipole moments can be expressed as shown in Tab. 4.3.

n (Multipole moment)	$\boldsymbol{B_x}$, $\boldsymbol{\alpha = 0}$ **(Normal)**	$\boldsymbol{B_x}$, $\boldsymbol{\alpha = \pi/2}$ **(Skew)**
1 (Dipole)	0	1
2 (Quadrupole)	$r\sin(\theta) = y$	$r\cos(\theta) = x$
3 (Sextupole)	$r^2\sin(2\theta) = 2r^2\sin(\theta)\cos(\theta) = yx$	$r^2\cos(2\theta) = r^2\left(\cos^2(\theta) - \sin^2(\theta)\right) = x^2 - y^2$
4 (Octupole)	$r^3\sin(3\theta) = \ldots = 3yx^2 - y^3$	$r^3\cos(3\theta) = \ldots = x^3 - 3y^2x$
5 (Decupole)	$r^4\sin(4\theta) = \ldots = yx^3 - y^3x$	$r^4\cos(4\theta) = \ldots = x^4 + y^4 - 6x^2y^2$

Table 4.3 – Normal and skew magnetic field multipole moments expressed in both polar and cartesian coordinates.

Defining the distance from the pole midplane to the pole surfaces (9 cm) as a, $y_{top} = a$ and $y_{bot} = -a$. From Eq. 4.7, $K_z = -n_y B_x/\mu_0$. Ignoring the constant, the distributions of currents in the top and bottom surface coils which produce the different magnetic field patterns are thus given as

$$K_z^{top} = B_x \tag{4.8}$$

and

$$K_z^{bot} = -B_x. \tag{4.9}$$

The current distributions which produce the different magnetic field multipole components are derived by inserting the expressions of Tab. 4.3 into Eqs. 4.8 and 4.9. They are listed in Tab. 4.4.

n (Multipole moment)	**Normal, K_z^{top}**	**Normal, K_z^{bot}**	**Skew, K_z^{top}**	**Skew, K_z^{bot}**
1 (Dipole)	–	–	a	$-a$
2 (Quadrupole)	a	a	x	$-x$
3 (Sextupole)	ax	ax	$x^2 - a^2$	$-x^2 + a^2$
4 (Octupole)	$3ax^2 - a^3$	$3ax^2 - a^3$	$x^3 - 3a^2x$	$-x^3 + 3a^2x$
5 (Decupole)	$ax^3 - a^3x$	$ax^3 - a^3x$	$x^4 + a^4 - 6a^2x^2$	$-x^4 - a^4 + 6a^2x^2$

Table 4.4 – The surface coil current configurations which produce the different magnetic field multipole components. In these expressions x is radial position and a is a constant.

Thus, for example, the same current (magnitude and sign) can be used in all 200 coils to produce a normal quadrupole magnetic field distribution. To produce a skew quadrupole distribution, the strengths of the currents in the top coils should vary linearly as a function of radial position, while the currents in the bottom coils should have the same magnitudes but opposite signs.

While each of the current configurations in Tab. 4.4 aims to create one pure magnetic field multipole component, each also creates small amounts of the other components. The multipole components produced by each configuration must be well understood in order to properly shim the magnetic field. After vacuum chamber installation, the trolley described in Sec. 3.4.1 was used to measure the effects of each current configuration. For this study, the currents in the 200 surface coils were toggled between two configurations: all set to 0 A and all set to a value consistent with a given multipole configuration. The differences in the measured strengths of the magnetic field multipole components between the two configurations were taken as the calibration values for that multipole current configuration. A maximum current of 2 A was used for the calibration measurements. Scaling linearity was verified with the normal quadrupole configuration by measuring the magnetic field components produced by currents of 10 different strengths.

Multipole Effect (ppm)	**Norm. Quad. Config**	**Skew Quad. Config**	**Norm. Sext. Config**	**Skew Sext. Config**	**Norm. Oct. Config**
Norm. Quad.	-339.402	4.726	2.493	0.433	-43.661
Skew Quad.	-10.505	-141.516	-0.970	0.472	-1.244
Norm. Sext.	-2.052	-0.202	-56.291	1.391	0.678
Skew Sext.	0.042	-1.454	-3.575	-20.951	-0.242
Norm. Oct.	3.378	-1.213	-0.322	-0.044	-9.979
Skew Oct.	0.818	11.110	-0.016	-0.387	-0.904
Norm. Dec.	-0.221	0.024	1.711	-0.474	-0.147
Skew Dec.	0.040	0.196	0.366	3.106	-0.036

Table 4.5 – The strengths of the magnetic field multipole components produced by the current configurations of Tab. 4.4. Each configuration through the skew sextupole produces the desired magnetic field component, in addition to small amounts of the other components. The normal octupole configuration produces a large normal quadrupole component.

Results of the calibration measurements are given in Tab. 4.5. Current configurations through the skew sextupole produce the desired magnetic field distributions. The hardware configuration was unable to produce the desired results for the higher order multipole configurations[1]. However, this fact is not concerning. As discussed in Sec. 3.7, the magnetic field is convoluted with the muon beam distribution. However, there are no significant multipole components present in the muon beam distribution above the normal sextupole.

A method of images calculation was used to verify the measured magnetic field contributions from each current configuration. The magnetic field produced by a circular current-

[1]A method of images calculation revealed that these current configurations would only be effective with either more concentric coils or with a smaller gap between the upper and lower pole pieces.

carrying coil in free space can be expressed using the law of Biot-Savart:

$$B_{coil}(r) = \frac{\mu_0 I}{2r}. \tag{4.10}$$

In the $g-2$ setup, the surface coils sit very close to the iron pole pieces. Image currents of strength

$$I_{image} = \left(\frac{\mu - \mu_0}{\mu + \mu_0}\right) I \tag{4.11}$$

must be accounted for in both the upper and lower pole pieces, where μ is the permeability of the pole material. The image locations in the top and bottom poles can be expressed as

$$y_{image,1} = (-1)^{n+1}\left[2(n+1)a + y_{coil}\right] \tag{4.12}$$

$$y_{image,2} = (-1)^{n}\left[2(n+1)a - y_{coil}\right], \tag{4.13}$$

where a is again the magnet half gap height and $y_{coil} = 8.8\,\text{cm}$ is the vertical distance between the surface coils and the magnet midplane [88, 89]. These image coil locations are used to calculate the $|\vec{r}| = |\vec{r}_{loc} - \vec{r}_{coil}|$ that is an input to Eq. 4.10 when calculating the magnetic field created by the surface coils at any location in the muon storage region.

For each current configuration in Tab. 4.4, a method of images calculation was used to calculate the sum of the magnetic fields created by all 200 coils at each trolley probe location. Good agreement was found between a multipole expansion of these values and the calibration measurement results. This calculation was also used to extract the radial magnetic field contribution from each current configuration, a magnetic field component which can not be measured by the trolley pNMR probes. More discussion of the radial magnetic field is provided in Ch. 5.

Current Optimization

The surface coils are used to minimize the strengths of all azimuthally averaged higher order magnetic field multipole components, including the radial component, present in the muon storage region. This is done by creating magnetic field multipole components of the same

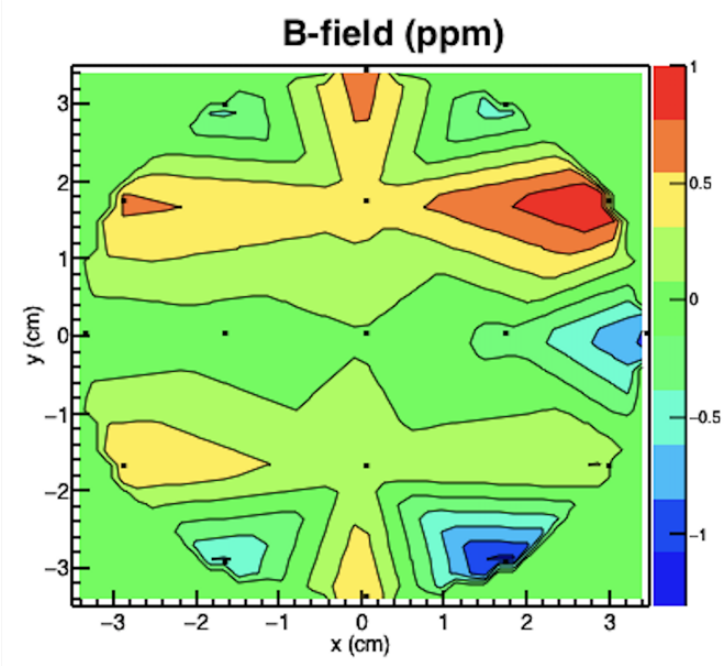

Figure 4.13 – The azimuthally averaged magnetic field in the muon storage region as a function of x and y after surface coil shimming in Spring 2017.

magnitude but opposite sign of those that are present. An optimization program takes the amplitudes of the azimuthally averaged magnetic field multipole components as input and produces suggested currents for the 200 coils. The program minimizes the quantity $|Ax - y|$ using a least squares algorithm, where $|A|$ is a matrix of the magnetic field components produced by each of the current configurations (the values of Tab. 4.5), x is a vector of the strength of each configuration to be used relative to the 2 A that were used for calibration, and y is a vector of the multipoles to be minimized.

Using the post-rough shimming multipole component amplitudes of Tab. 4.2 as input to the optimization program, the amplitudes of the azimuthally averaged magnetic field components were all reduced to less than 300 ppb. An azimuthally averaged magnetic field map from spring 2017 is shown in Fig. 4.13 while the strengths of the azimuthally averaged multipole components are listed in Tab. 4.6.

Multipole	**Normal component amplitude (ppm)**	**Skew component amplitude (ppm)**
Quadrupole	-0.19	0.28
Sextupole	0.05	0.27
Octupole	-0.07	0.25
Decupole	0.23	0.07

Table 4.6 – Amplitudes of the azimuthally averaged magnetic field multipole components after surface coil shimming in Spring 2017. These can be compared to the values in Tab. 4.2.

4.5.2 Power Supply Feedback

The second active shimming tool used in the Fermilab experiment is known as "power supply feedback." Due to temperature variations in the experimental hall, the magnet geometry changes over time. The magnet steel expands and contracts, changing the air gap between the pole pieces and thus the magnitude of the dipole magnetic field component in the muon storage region[2]. To counteract this change, a characteristic subset of 50 fixed probes are used to monitor the average magnetic field. The main magnet current is regulated to keep the fixed probe average constant to within $\pm 10\,\text{Hz}$ ($\pm 160\,\text{ppb}$). Typical performance keeps the fixed probe average stable to within $\pm 1\,\text{Hz}$, as shown in Fig. 4.14.

[2]The magnitudes of the other magnetic field components also change, but the power supply feedback is unable to counteract this.

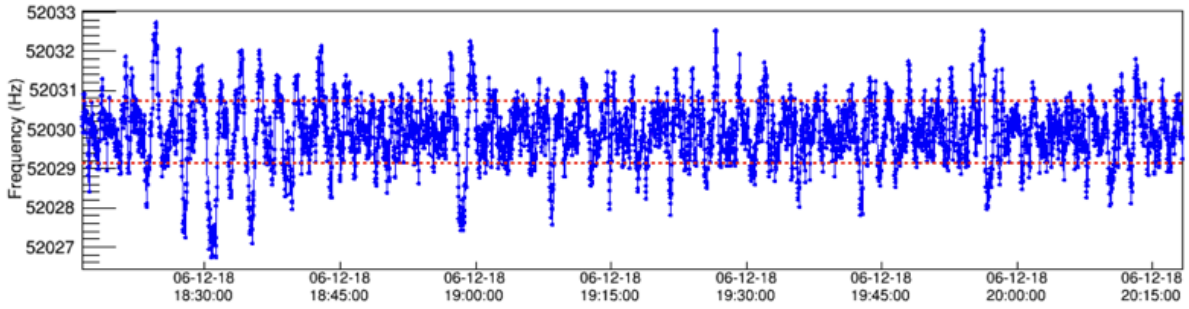

Figure 4.14 – A subset of fixed probes is used to monitor the evolution of the average magnetic field (blue points). With typical performance, the power supply feedback system keeps this average stable to ± 1 Hz (red bands), surpassing the ± 10 Hz goal. Plot credit: [63]

Chapter 5

RADIAL MAGNETIC FIELD MEASUREMENTS

5.1 Motivation

In previous chapters, the magnetic field in the muon storage region has been discussed only as a scalar distribution, ignoring the non-vertical components. However, because these components cause real effects on the motion of the muon beam, they must be understood. A symmetric muon beam centered at the magic radius would be subjected to only a radial force from a magnetic field with no non-vertical components and with the same strength at all locations. The muon beam would be completely contained in the radial direction. This is not the case in the Fermilab $g-2$ experiment. The magnetic field has non-vertical components and is not perfectly homogeneous, and the muon beam distribution is not symmetric or radially centered. Muons experience a vertical force from the non-vertical magnetic field components. For example, in the $g-2$ magnetic storage ring a 50 ppm radial magnetic field component causes a 2.5 mm vertical beam displacement [90]. However, the azimuthally averaged radial magnetic field component can be minimized using the surface correction coils described in Sec. 4.5.1.

As discussed in Ch. 3, pNMR probes are used to both map the magnetic field in the muon storage region and to track the magnetic field evolution from outside of the vacuum chambers. While techniques for extracting frequencies from FIDs allow for magnetic field measurements good to the 10 ppb level, pNMR probes are sensitive only to magnetic field magnitude, not direction. While they are incredible tools for measuring the vertical component of the magnetic field in the muon storage region, they can not be used to measure radial or longitudinal magnetic field components. A different type of magnetometer, a Hall probe, was used instead.

5.2 Hall Effect

Discovered in 1879 by Edwin Hall, the Hall effect is the production of a potential difference across a semiconductor sample, perpendicular to a current flowing in the semiconductor, when exposed to a magnetic field [91]. The measurable voltage is proportional to the component of the magnetic field normal to the semiconductor surface. This principle is the foundation of Hall probes, which are sensitive to both magnetic field magnitude and direction.

A typical Hall probe consists of a semiconductor sample with four contacts: two current contacts and two voltage contacts, as shown in Fig. 5.1. A stable current source is used to provide a current which flows across the semiconductor. With no magnetic field present, electrons in the semiconductor sample move parallel to the electric field $\vec{E}$. In the presence of a magnetic field $\vec{B}$, electrons moving with a velocity $\vec{v}$ feel a Lorentz force given by

$$\vec{F} = e(\vec{E} + \vec{v} \times \vec{B}). \tag{5.1}$$

As a consequence of this force, electrons begin to pile up on one side of the semiconductor sample, creating a charge imbalance. This charge imbalance leads to the production of an electric field perpendicular to the current, known as the Hall field $\vec{E}_H$. The strength of the Hall field stops increasing and equilibrium is achieved when the force on the electrons from the magnetic field is balanced by the force from this induced electric field. The now stable Hall field causes a measurable potential difference, known as a Hall voltage, between the edges of the semiconductor sample [91].

In the presence of an external magnetic field, the electric field in the semiconductor of a Hall probe is given as

$$\vec{E} = \rho\vec{J} + R_h\vec{B} \times \vec{J} - M\rho\vec{B} \times [\vec{B} \times \vec{J}], \tag{5.2}$$

where ρ is the resistivity, $\vec{J}$ is the current density across the semiconductor sample, R_h is the Hall magnetoresistivity, and M is the transverse magnetoresistivity. The induced voltage

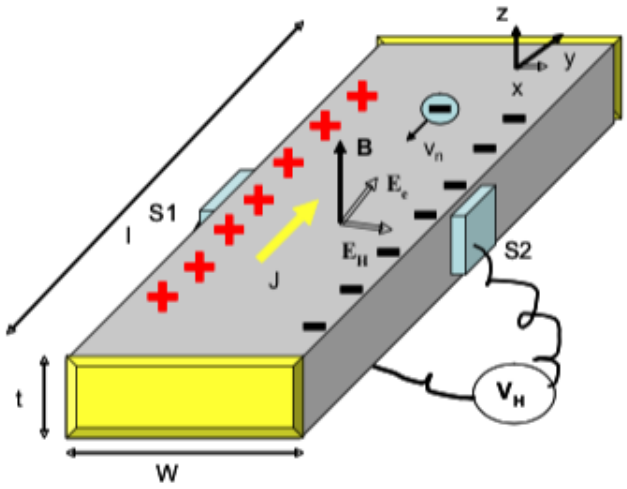

Figure 5.1 – Typical Hall probes consist of a semiconductor sample with four contacts: two current contacts (yellow) and two voltage sensing contacts (light blue). In the presence of a magnetic field, electrons begin to pile up on one side of the sample. In response to this, a Hall field E_H forms to balance the force on the electrons from the magnetic field B and the electric field E_e. The Hall field creates a measurable potential difference across the semiconductor sample, perpendicular to the applied current, which is proportional to the strength of the magnetic field component normal to the semiconductor surface. Image credit: [91]

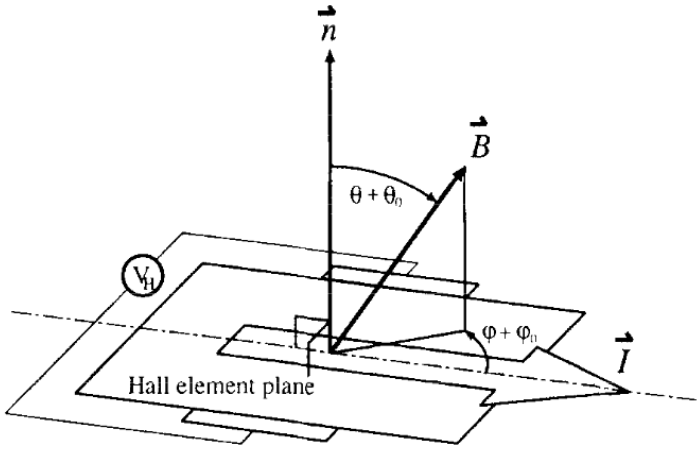

Figure 5.2 – The induced voltage across a Hall probe, given by Eq. 5.3, is proportional to the components of the magnetic field $\vec{B}$ both in the plane of the semiconductor sample and perpendicular to it. It is additionally dependent upon the angle ϕ between the current $\vec{I}$ and the in-plane magnetic field. Image credit: [92]

across the semiconductor sample is given by

$$V = k_1 B_\perp I + k_2 \vec{B}_{||}^2 I \sin(2\phi) + V_{off}, \tag{5.3}$$

where $B_\perp$ is the magnitude of the magnetic field component normal to the semiconductor, $\vec{B}_{||}$ is the in-plane magnetic field, ϕ is the angle between the current and the in-plane magnetic field, V_{off} is the zero magnetic field offset voltage, and k_1 and k_2 are known as the Hall and planar Hall coefficients respectively [90]. This geometry is illustrated in Fig. 5.2.

When a Hall probe is used to measure a particular component of a magnetic field, it is the normal Hall voltage that is desired (the first term in Eq. 5.3). The planar Hall effect and offset voltage (the 2nd and 3rd terms) must be properly accounted for. The voltage offset can be minimized by making measurements with the Hall probe rotated 180° about the vertical axis. This rotation effectively changes the direction of the current (the sign of I) and causes the signs of the normal and planar Hall effects to flip. The offset voltage is unaffected. Taking the difference of the measurements and dividing by 2 cancels the contribution from

this unwanted offset voltage.

Multiple methods can be used to minimize the planar Hall effect, all of which require making multiple measurements and taking differences. From Eq. 5.3, the planar Hall effect is proportional to the sine of twice the angle between the current and the in-plane magnetic field. The sign of the effect can be flipped by changing this angle by 90°. One way to achieve this rotation is to physically rotate the Hall probe. Another is to use two Hall probes, with one rotated by 90° with respect to the other[1]. A third option is to use the "spinning current technique" in which the current and voltage leads are interchanged, effectively changing the current direction by 90°.

Performing physical rotations and making multiple measurements carries with it the possibility for many different alignment issues (details on Hall probe misalignments are presented in [93]). The spinning current technique was therefore chosen for use when making measurements of the radial and longitudinal magnetic field components in the muon storage region.

5.3 Planar Hall Effect Calibration

An Asensor HE244T Hall probe was used to measure the radial and longitudinal magnetic field components in the $g-2$ storage ring [94]. This probe was chosen due to its marketed "ultra low planar hall coefficient." The hope was that the planar Hall effect would be negligibly small and only the offset voltage would need to be mitigated. The planar Hall coefficient needed to be measured to verify this.

As discussed, the planar Hall effect has a $\sin(2\phi)$ dependence. A mount was designed which allowed for varying ϕ over a full 360°. The mount design is shown in Fig. 5.3. The mount consists of a base plate sitting on three ceramic balls which form a 3-point contact system and a large cylinder which can rotate about its central axis. The front face of the cylinder has degree markings and the back face contains a slot to hold an aluminum cube

[1]This method was used to measure the radial magnetic field in the Brookhaven experiment [90].

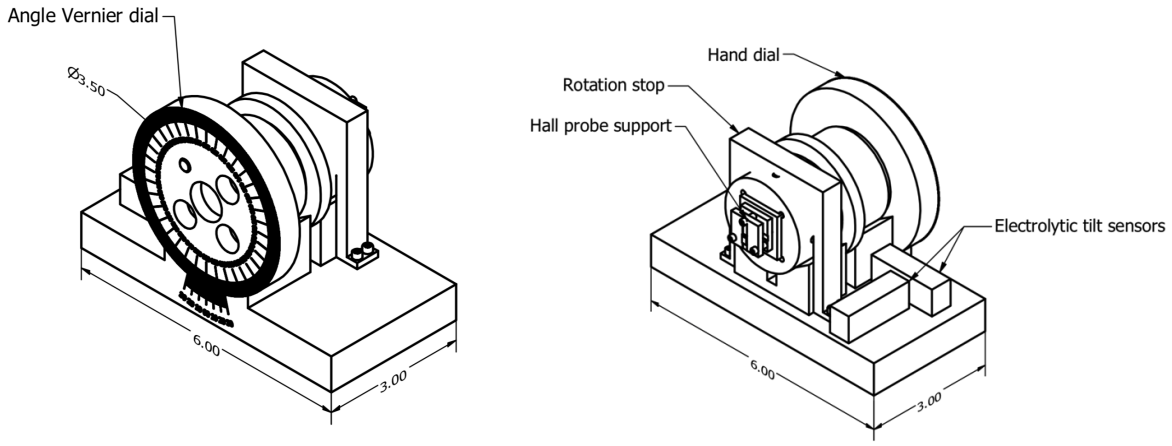

(a) Front view, with degree markings.

(b) Rear view, with a Hall probe mounted on an aluminum cube.

Figure 5.3 – An apparatus was designed for rotating the Hall probe around its normal axis. It was used to measure the planar Hall coefficient of the Hall probe by changing the angle between the current and the in-plane magnetic field component. The front of the apparatus has degree markings while the back contains a slot into which a hall probe mounted to a cube was inserted. Image credit: [61]

onto which a Hall probe is mounted. Two electrolytic tilt sensors were mounted onto the baseplate to measure the platform tilt in two orthogonal directions during the planar Hall coefficient measurement.

In fall 2016, after rough shimming but before vacuum chamber installation, the planar Hall effect was measured by rotating the cylinder in 10° steps. The voltage was measured for each rotation angle. This process was repeated four times with the measurement platform at different radial tilts. In the first trial, the three ceramic balls sat directly on the bottom pole surface. For the other three trials, a 10, 33, or 65 mil thick piece of aluminum was inserted under one of the balls. Fig. 5.4 shows the recorded voltages as a function of rotation angle with the no shim data in red, 10 mil shim data in blue, 33 mil shim data in black, and 65 mil shim data in brown. The data were fit using two sinusoids with periods of π

and 2π. The amplitude of the π component was negligible for all data sets . Fitting for only a 2π signal resulted in non-sinusoidal residuals at the 50 µV level, which is compared to the 5 mV amplitude of the sinusoid. The lack of a π component confirmed that the planar Hall coefficient of the chosen Hall probe is negligibly small and that the use of the spinning current technique was unnecessary.

5.4 Measurement Platform

The rotating cylinder platform was specifically designed for measuring the size of the planar Hall effect. It is not well suited for measurements of the radial and longitudinal magnetic field components in the muon storage region. A second platform was therefore designed which allowed for easy tilt adjustments and 180° rotations of the Hall probe. The design of this platform is shown in Fig. 5.5. The Hall probe is still mounted to an aluminum cube, but in this setup the cube is clamped onto a platform with the Hall probe face sitting parallel to the vertical axis. The small platform holding the cube also holds the two tilt sensors, oriented to measure the tilt of the platform in the radial and azimuthal directions. This small, Hall probe carrying platform has three ceramic balls in its base which sit in milled out holes on the uppermost plate of the entire measurement platform. Holes are provided for four measurement orientations: two radial and two longitudinal. The uppermost plate can slide vertically along three rods, with its height fixed using aluminum spacers. The spacers sit around the rods between the top plate and an additional bottom plate. The bottom plate sits on radially-oriented rails, allowing the radial position of the Hall probe to be varied. The radial position is also fixed using aluminum spacers.

The entire platform is supported by three ultra-finely threaded screws: Proforma ultra-fine hex adjusters 3/16"-100 [95]. These screws both define the plane of the apparatus and are used to make microradian level adjustments to the platform tilt in the radial and azimuthal directions. One screw is located at the azimuthal center of the platform, 2.5 cm radially inwards, while the other two are located on the left and right edges of the radially outwards side of the platform. These two screws are symmetrically positioned around the

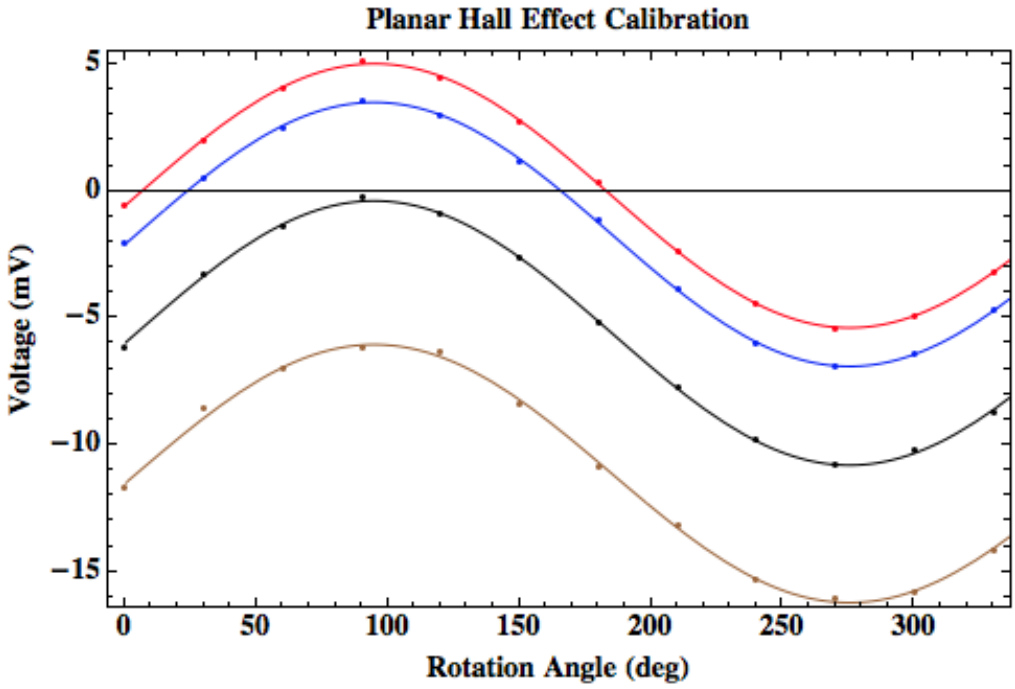

Figure 5.4 – The cylinder into which the Hall probe was mounted was rotated through a full 360° with the platform sitting at four different radial tilts. The recorded voltages are plotted as a function of rotation angle. The red data was collected with all three balls on the bottom of the measurement apparatus sitting directly on the bottom pole surface. The blue, black, and brown data sets were collected with one of the balls sitting on a 10 mil, 33 mil, or 65 mil thick piece of aluminum respectively. The data were fit with two sinusoids of periods π and 2π. The negligible amplitudes of the π components led to the conclusion that the planar Hall coeficient is negligibly small in the chosen Hall probe.

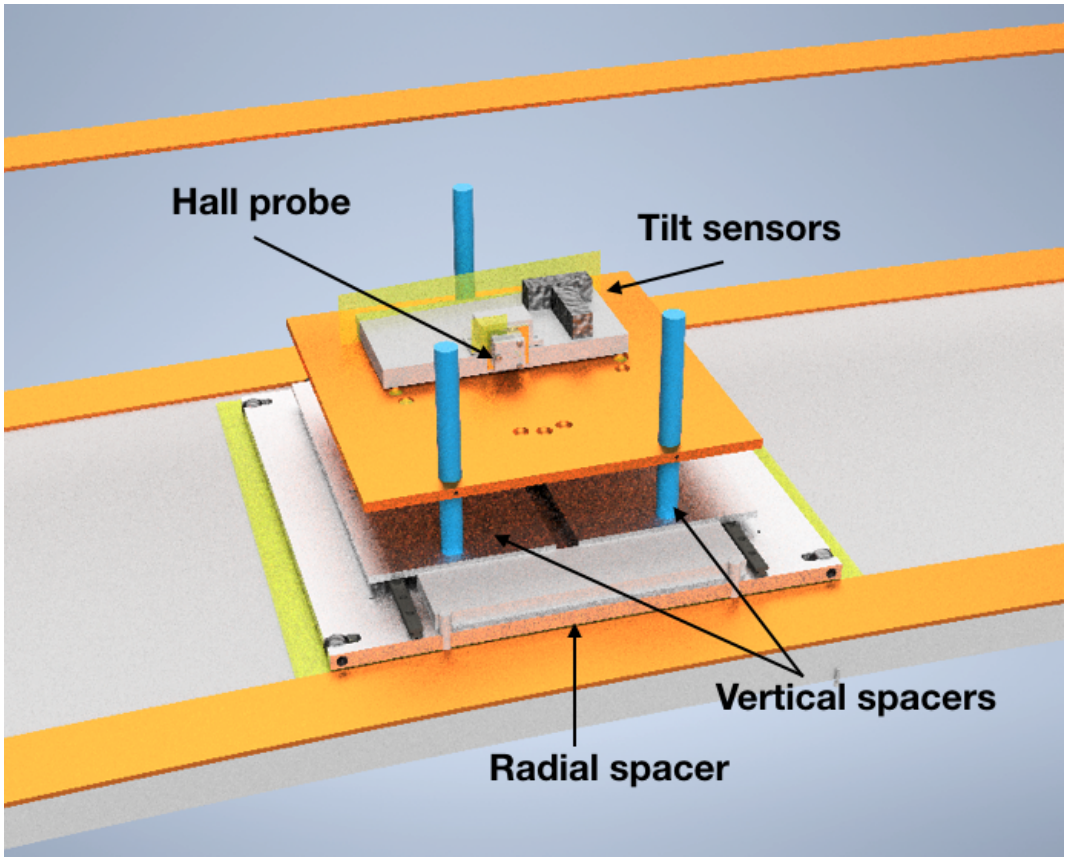

Figure 5.5 – A Hall probe was used to measure the radial and longitudinal magnetic field components in the $g-2$ muon storage region. The hall probe is attached to an aluminum cube which is held in place on a platform which also holds two tilt sensors, oriented to measure tilts in the radial and azimuthal directions. This small platform has three ceramic balls in its base, which sit in milled out holes on the top plate of the complete platform. The height and radial position of the Hall probe can be adjusted using two sets of aluminum spacers. Image credit: [61]

platform's azimuthal center, with a spacing of 22.1 cm. They are located 27.2 cm radially outwards from the front screw. The front edge of the platform base holds two alignment pins which are used for radial alignment against an inner edge shim.

5.5 Measurement Procedure

The radial and longitudinal magnetic field components in the muon storage region were measured at over 100 azimuthal locations in fall 2016. Before the measurements began, a laser tracker was used to locate the desired positions, which were then marked on the pole pieces. The measurement platform was brought to each azimuthal location and a mark on the base plate was aligned with the pole mark. The base plate mark indicates the azimuthal location of the Hall probe.

At each azimuthal location two measurements were made: one with the Hall probe in its nominal orientation and one with the Hall probe rotated 180° about the vertical axis. Data were collected for 90 seconds in each orientation. After a rotation, the platform tilts in both the radial and azimuthal directions were adjusted using the finely threaded screws to be within 5 µrad of their pre-rotation values (2-3 µrad was often achieved). To minimize the required tilt adjustments after a rotation, each measurement began with the platform oriented such that the two tilt sensors reported tilts close to their "zero" tilt values. These values were determined by allowing the tilt sensors to settle in one orientation[2], recording the tilts, performing a 180° rotation, and then again recording the tilts after the tilt sensors had settled. The average of the tilt sensor readings in the two orientations was interpreted as the "zero" value.

In practice, due to the settling time of the tilt sensors after a rotation, performing all four required measurements (radial and longitudinal magnetic field components, both before and after a rotation) in series at the same location was not the most time effective strategy. Instead, one type of measurement was taken at multiple azimuthal locations. Each location

[2]Because the tilt sensors are electrolytic, movement causes the liquid to coat the inner pads. This leads to false measurements until all of the liquid has settled at the bottom of the vessel.

was later revisited, this time making measurements with the Hall probe in the reverse orientation. The radial and longitudinal magnetic field components were measured multiple times, on multiple days, at several specific azimuthal locations, verifying that the components were stable at the sub-10 ppm level.

5.6 Measurement Results and Effects

The measured radial and longitudinal magnetic field components are pictured in Fig. 5.6 as a function of azimuthal location in the storage ring magnet. An average radial magnetic field of 68.5±68.9 ppm and an average longitudinal magnetic field of 0.14±36.9 ppm were measured, where a positive radial magnetic field is defined as pointing towards the center of the storage ring (outer to inner radius) and a positive longitudinal magnetic field is defined as pointing downstream. While the longitudinal magnetic field in the muon storage region was not measured in the Brookhaven experiment, the Fermilab radial magnetic field measurements can be compared to the 28.2±117.1 ppm average radial magnetic field measured at Brookhaven [90]. The uncorrected-for average radial magnetic field at Fermilab is higher than it was at Brookhaven, but azimuthal variations are reduced by a factor of almost two.

The effects of these non-vertical magnetic field components on the motion of the muon beam can be estimated using equations of motion. The main conclusions from [96] are reproduced here. Working in cylindrical coordinates with $\hat{z}$ the vertical direction and $\hat{x} = \hat{r}$, the equation of motion for muons in the $g-2$ storage ring is

$$\frac{\partial^2 z}{\partial \theta^2} + \left(\frac{r_0}{\beta B_0} k - \frac{r_0}{B_0} \frac{\partial B_z}{\partial x}|_0 \right) z = r_0 \frac{B_x(\theta)}{B_0}, \tag{5.4}$$

where r_0 is the equilibrium radius of the muon orbit, $\beta = v/c$, B_0 is the average vertical magnetic field strength, and k is associated with the quadrupole electric field contribution ($\vec{E} = k(x\hat{x} - z\hat{z})$). x and z are measured with respect to the equilibrium radius at the storage region midplane, while the term in parentheses is known as the effective field index, n_{eff}.

The azimuth-dependent radial magnetic field can be expressed as a Fourier series

$$B_x(\theta) = \sum_{N=0}^{\infty} R_N \cos\left(N\theta + \phi_N\right), \tag{5.5}$$

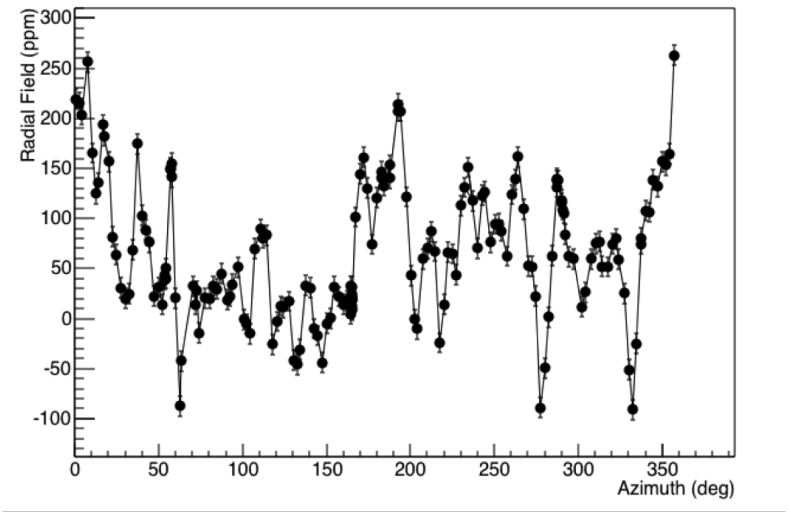

(a) Radial magnetic field as a function of azimuthal position.

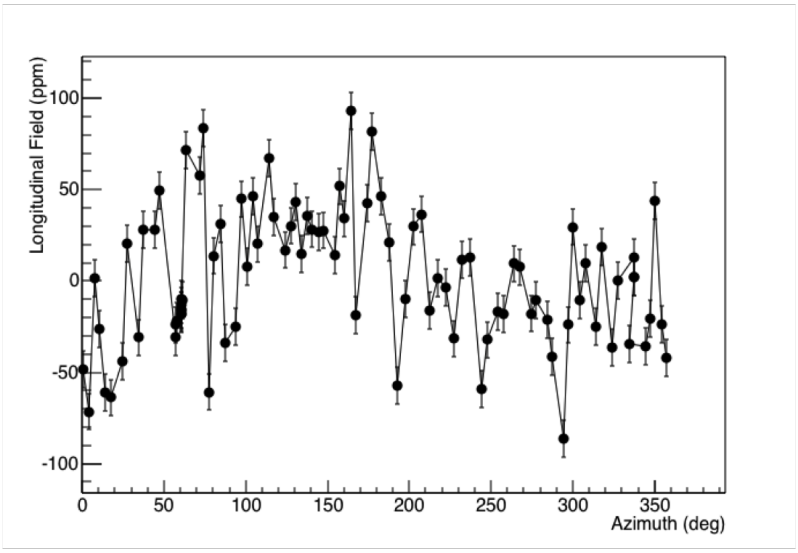

(b) Longitudinal magnetic field as a function of azimuthal position.

Figure 5.6 – The radial and longitudinal magnetic field components were measured at over 100 azimuthal locations around the $g-2$ magnetic storage ring. The measurements are pictured as a function of azimuthal position. An average radial magnetic field of 68.5±68.9 ppm and an average longitudinal magnetic field of 0.14±36.9 ppm were measured.

where R_N (ϕ_N) is the amplitude (phase) of the Nth harmonic of the radial magnetic field. Inserting Eq. 5.5 into Eq. 5.4, the equation of motion becomes

$$\frac{\partial^2 z}{\partial \theta^2} + n_{eff} z = \frac{r_0}{B_0} \sum_{N=0}^{\infty} R_N \cos\left(N\theta + \phi_N\right). \tag{5.6}$$

Solving this differential equation, muons oscillate vertically according to

$$z(\theta) = A_z \cos(\nu_z \theta + \phi_z) + \sum_{N=0}^{\infty} \frac{r_0}{\nu_z^2 - N^2} \frac{R_N}{B_0} \cos(N\theta + \phi_N), \tag{5.7}$$

where $\nu_z = \sqrt{n_{eff}}$ is the known as the vertical tune and A_z and θ in the betatron motion term are determined from initial conditions.

Expanding the radial field magnetic field measurements of Fig. 5.6a in a Fourier expansion and using an effective field index of $n_{eff} = 0.17$, the amplitude of the vertical oscillation caused by each Fourier term can be calculated. The amplitudes due to the first six terms are listed in Tab. 5.1, with higher order terms leading to even smaller amplitudes. The $N = 0$ term, caused by the azimuthally averaged radial magnetic field, has the largest effect on the muon beam motion by a factor of 10. However, its effect is minimized by using the surface coils to create a radial magnetic field of the same magnitude but opposite sign.

5.7 Canceling the Average Radial Magnetic Field

A method of images calculation[3] was used to determine the radial magnetic field produced by the surface coil current configurations of Tab. 4.4. However, creating a radial magnetic field of the same magnitude but opposite sign of the average measured field did not lead to a vertically centered muon beam. This is because the radial magnetic field was not measured over the full 360° of the muon storage region. Instead, the muon beam itself was used to determine the actual azimuthally averaged radial magnetic field present in the muon storage region. This was done by observing the average decay positron height, a proxy for the muon beam height, measured by the 24 calorimeters.

[3]The method of images calculation is described in Sec. 4.5.1.

Fourier term	Vertical oscillation amplitude (mm)
0	2.702
1	0.267
2	0.088
3	0.017
4	0.018
5	0.005

Table 5.1 – The presence of an azimuth-dependent radial magnetic field in the muon storage region causes the muon beam to oscillate vertically. Expanding the data of Fig. 5.6a in a Fourier expansion, the oscillation amplitude caused by each Fourier component can be calculated using Eq. 5.7. The amplitudes caused by the first six Fourier components are listed.

Using a radial magnetic field surface coil configuration[4], the strength of the radial magnetic field produced by the surface coils was varied. The average muon beam height was later extracted for each setting. The effect of the magnitude of the surface coil currents on the beam height is shown in Fig. 5.7, where a magnitude of 100 mA produces a 29.7 ppm radial magnetic field. Using a current magnitude of 260.12 mA in all surface coils centered the decay positron distribution vertically. This current setting produces a 77.2 ppm radial magnetic field. The average radial magnetic field extracted from this study was combined with trolley measurements as the input to the surface coil current optimization program. This produced a current configuration which both vertically centers the muon beam and minimizes the azimuthally averaged magnetic field multipoles.

[4]A radial magnetic field is created by setting the currents in all top coils to one value and the currents in all bottom coils to the same value but with the opposite sign.

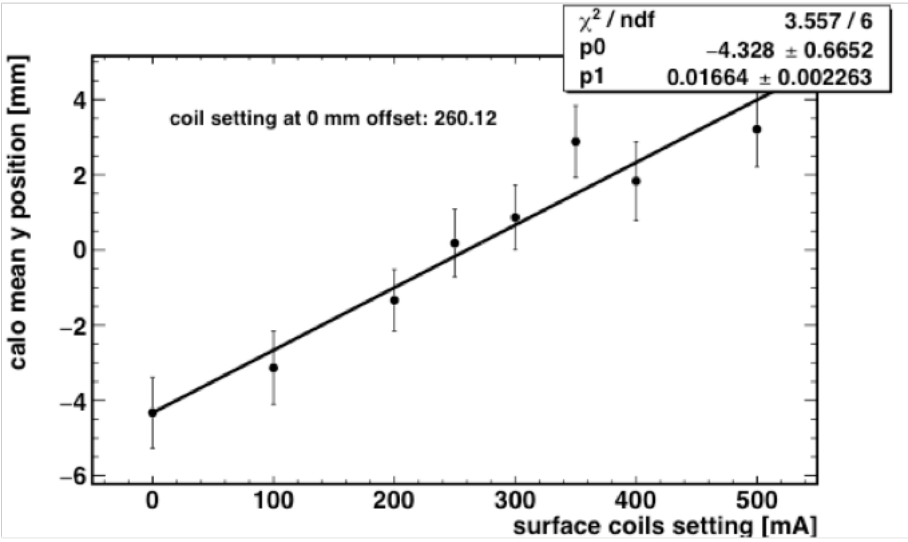

Figure 5.7 – A radial magnetic field can be produced with the surface coils by using the same current in all top coils, and the same current but of opposite sign in all bottom coils. Varying the magnitude of the current causes the equilibrium muon beam height to change. The mean vertical positron position measured by the calorimeters, a proxy for the muon beam height, is shown as a function of surface coil current. A current magnitude of 260.12 mA, corresponding to a radial magnetic field of 77.2 ppm, was found to center the muon beam vertically in the muon storage region.

Chapter 6

MAGNETIC FIELD ANALYSIS

The magnetic field in the muon storage region of the $g-2$ magnetic storage ring is mapped approximately every three days by a trolley carrying an array of 17 pNMR probes (henceforth referred to as "probes"), as described in Sec 3.4.1. While muons are present in the storage region, the trolley is parked outside of the storage region in a "garage" and the magnetic field evolution is tracked using a suite of probes embedded in grooves on the outsides of the vacuum chambers, the fixed probe array. The process of tracking the magnetic field evolution is called "interpolation." There are two separate interpolation teams, Bloch and Purcell, with the Bloch interpolation steps and associated uncertainties discussed in the following sections, as well as in [97]. The author of this dissertation is the lead analyzer of the Bloch team. Details of the Purcell interpolation can be found in [98].

The description of team Bloch interpolation begins with a short discussion of magnetic field multipole moments in Sec. 6.1 and a discussion of magnetic field evolution in Sec. 6.2. Sec. 6.3 provides a brief introduction to the interpolation process, while data quality considerations are presented in Sec. 6.4. Sec. 6.5 and its associated subsections provide detailed information on each step of magnetic field interpolation, while Sec. 6.6 presents information on the systematic uncertainties associated with interpolation. Run 1 uncertainty tables are presented in Sec. 6.7, with combined uncertainties on the tracking of the evolution of all magnetic field multipole components at the sub-100 ppb level.

In the following sections, the strengths of the magnetic field multipole moments may be referred to by their multipole names, ie "the normal quadrupole magnetic field multipole moment" may be referred to as "the normal quadrupole." When referring to multipole moments calculated from measurements of either the trolley probes or the fixed probes, the

formulation "trolley/fixed probe normal quadrupole" will be used.

6.1 Magnetic Field Multipole Moments

As discussed in Sec. 3.6, the magnetic field in the muon storage region is expressed in terms of magnetic field multipoles, described by Eq. 3.11 and reproduced here

$$B(r,\theta) = B_0 + \sum_{n=1}^{N} \left(\frac{r}{r_0}\right)^n [a_n \cos(n\theta) + b_n \sin(n\theta)], \tag{6.1}$$

where a_n values represent normal magnetic field multipole strengths and b_n values represent skew magnetic field multipole strengths.

Magnetic field multipoles through $n = 4$, or the skew decupole, were used to describe the magnetic field distribution during the process of rough shimming (Ch. 4). For interpolation analysis, a study looking at magnetic field residuals after fitting the trolley probe measurements through various multipole moments showed that the normal duodecapole ($n = 6$) is the last significant multipole component present in the azimuthally averaged magnetic field in the muon storage region [99]. Magnetic field multipoles through this order are thus fit for in the team Bloch analysis. Magnetic field residuals remaining after fitting the azimuthally averaged magnetic field from a characteristic trolley run through the normal duodecapole are shown in Fig. 6.1. No additional higher order magnetic field multipole moments can be seen.

As discussed in Ch. 5, pNMR probes are sensitive only to magnetic field magnitude, not direction. For this reason, the multipole expansion of Eq. 6.1 assumes that no radial or longitudinal magnetic field components are present in the muon storage region, an incorrect assumption. While the azimuthally averaged magnetic field components in the radial and longitudinal directions are at the sub-1 ppm level (the geometry of the magnetic storage ring leads to the longitudinal magnetic field component being naturally small, while the surface coils are used to minimize the radial magnetic field component), local radial and longitudinal magnetic field components remain. Because the present analysis concentrates on interpolation of the azimuthally averaged magnetic field experienced by muons, and because

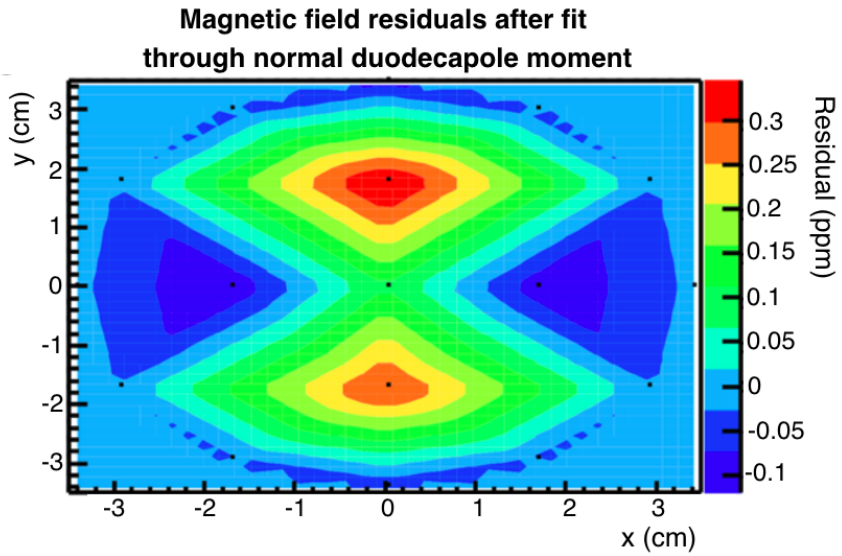

Figure 6.1 – The magnetic field in the muon storage region is described in terms of multipole moments. Fitting the azimuthally averaged magnetic field through various multipole moments, magnetic field residuals were used to determine that the normal duodecupole is the highest order magnetic field multipole moment necessary to describe the azimuthally averaged magnetic field present in the muon storage region. While structure remains after fitting through this order, the structure does not correspond to any higher order multipole moments and instead informs how well a multipole expansion of trolley data describes the magnetic field experienced by muons. Image credit: [100]

the radial and longitudinal magnetic field components add quadratically to the main vertical magnetic field and thus make a negligible contribution, these local variations are ignored[1].

6.2 Magnetic Field Changes and Features

Between trolley runs, the local magnetic field in the muon storage region can drift by parts per million due to temperature changes in the experimental hall. Fig. 6.2 shows the dipole as a function of azimuth for the two trolley runs bracketing a three day period of data collection (4/22/18-4/25/18), as well as the difference between them. Fig. 6.3 shows the dipole-subtracted azimuthally averaged magnetic field maps for the two trolley runs. The total range of the dipole azimuthal differences lies within a 16 ppm band. It is the job of the interpolation analyzers to determine the magnetic field at all times between trolley runs.

The evolution of the dipole at a characteristic fixed probe station is shown in Fig. 6.4. In addition to typical magnetic field drifts, this plot also reveals characteristic magnetic field features that the interpolation analyses must take into account, such as the magnetic field spike just before 7:00 am on 4/22/18. As discussed in Sec. 4.5.2, a subset of fixed probes is monitored in order to keep the dipole magnetic field component in the muon storage region constant. A feedback system adjusts the current of the main magnet coils to compensate for detected instabilities in the average of the measurements of these probes. At the time of this spike, the power supply feedback control was accidentally turned off and then back on. When turned off, the output current of the feedback system ramped to 0 A, causing a real magnetic field change. In addition to the spike, six "field jumps" can be seen. In a field jump event, the magnetic field suddenly "jumps" to a new value. This effect can be measured at all azimuthal locations, but with different amplitudes, as shown in Fig. 6.5. Each field jump creates a maximum positive magnetic field change at a particular azimuthal location, while the change is negative far away. The origin of these field jumps is not currently understood, but motion of the superconducting coils is suspected.

---

[1]The effects of these variations are described in Sec. 5.6.

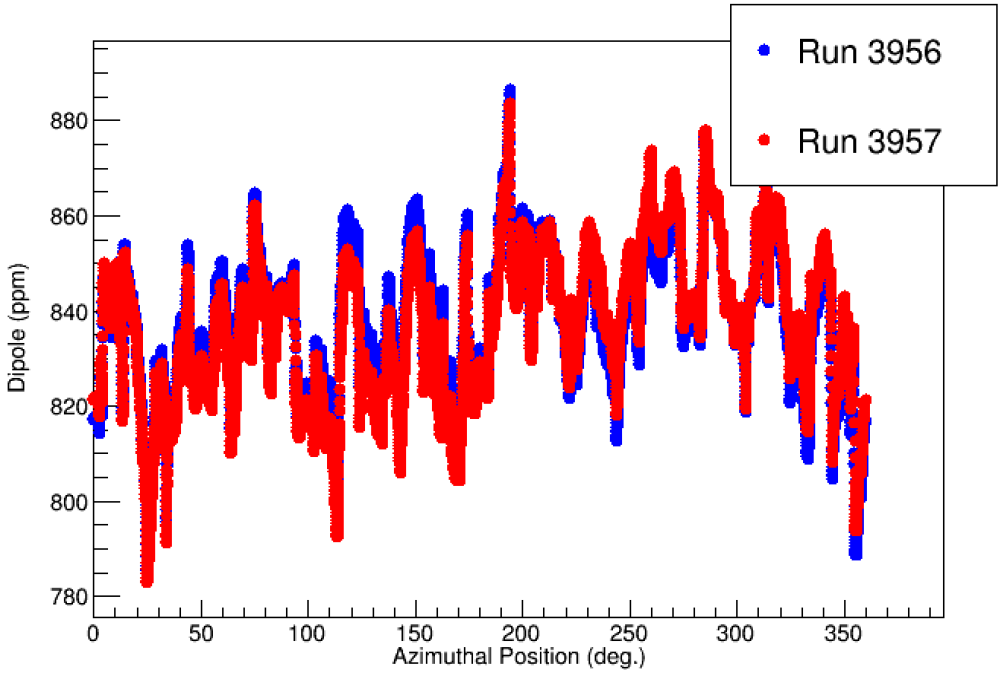

(a) Dipole vs. azimuth.

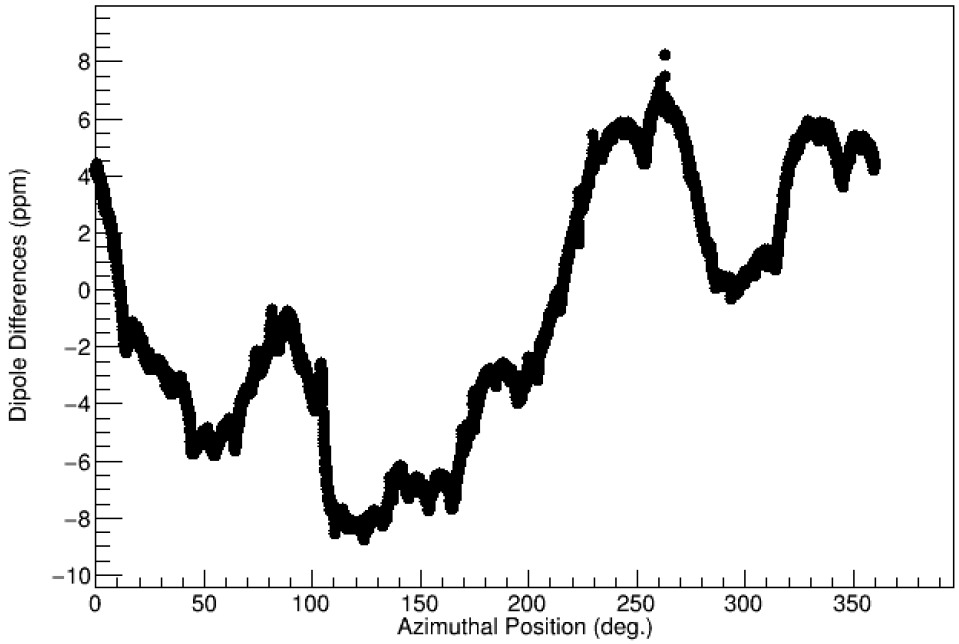

(b) Dipole difference vs. azimuth.

Figure 6.2 – The magnetic field in the muon storage region can drift by parts per million over the course of time between two trolley runs. The dipole magnetic field component is shown as a function of azimuth for two trolley runs separated by three days (4/22/18-4/25/18) in (a) while the difference of the two curves is shown in (b).

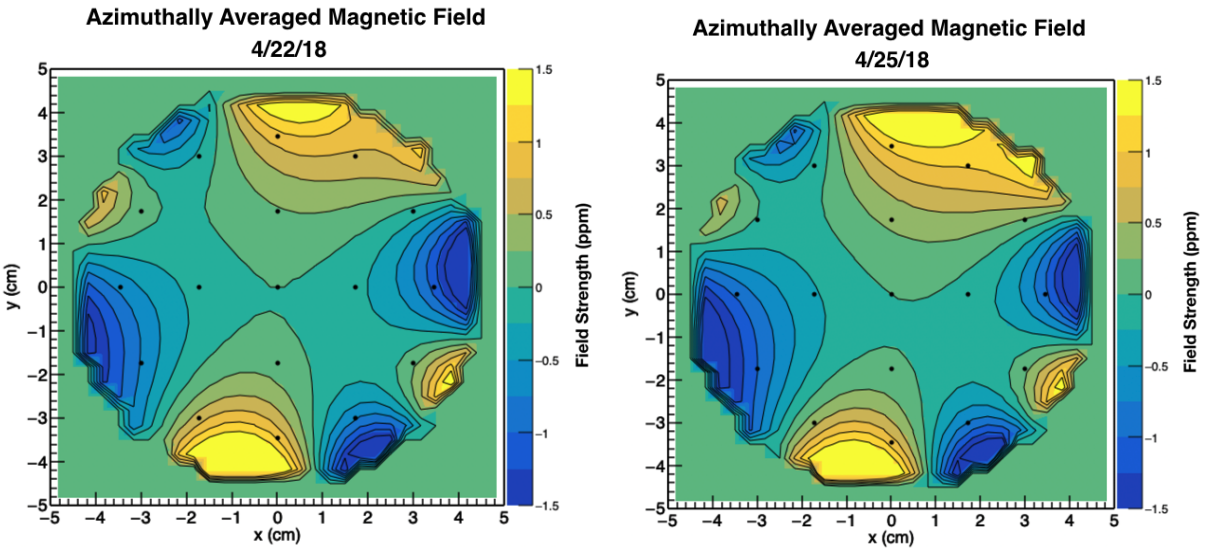

(a) Trolley run 1.

(b) Trolley run 2.

Figure 6.3 – All magnetic field multipole components evolve between trolley runs. The dipole-subtracted azimuthally averaged magnetic field maps for the two trolley runs shown in Fig. 6.2a are pictured.

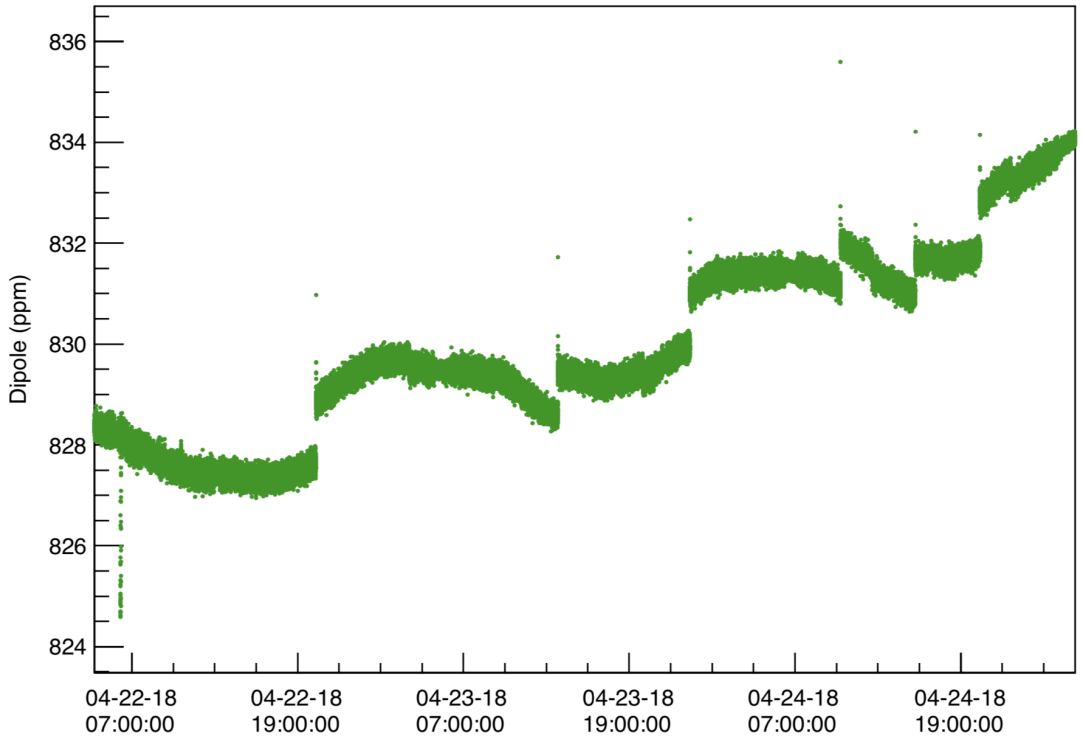

Figure 6.4 – The evolution of the fixed probe dipole magnetic field component from a characteristic fixed probe station. Multiple field steps are seen, as is a magnetic field spike due to an accidental power cycle of the power supply feedback system that occurred just before 7:00am on 4/22/18.

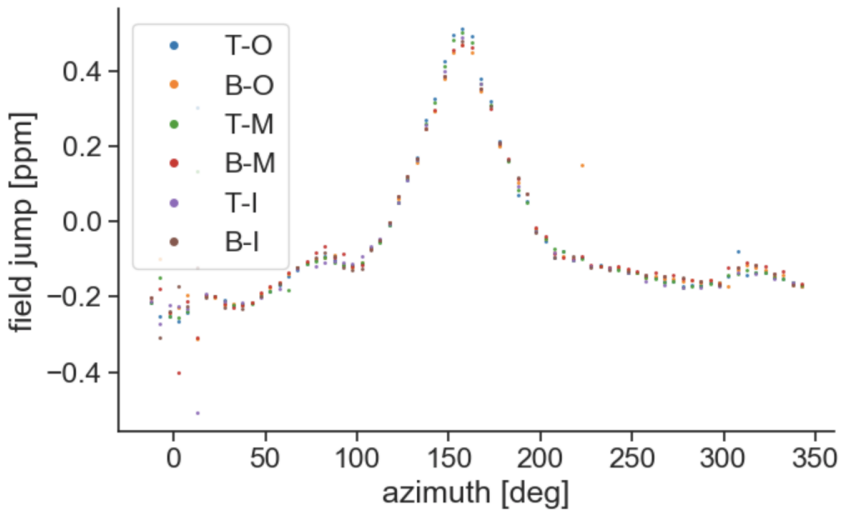

Figure 6.5 – In a field jump event, the magnetic field suddenly "jumps" to a new value. The jump is always centered around an azimuthal location, although the effect can be seen with varying amplitudes at all azimuthal locations. Fixed probes at all radial and vertical locations (top/bottom [T/B], and inner/middle/outer [I/M/O]) see the same effects. Image credit: [101]

The magnetic field data quality group flags periods of time when something other than typical magnetic field evolution occurs which causes the magnetic field to rapidly change, such as a field jump or a magnetic field change caused by the power supply feedback being operated incorrectly. Because the magnetic field distribution is convoluted with the muon beam distribution for the a_μ calculation (Sec. 3.7), these time periods are given to the ω_a data quality control group and are subsequently ignored by ω_a analyzers. However, while this data is not included in the a_μ calculation, interpolation analyzers must understand the magnetic field evolution during these periods, as they represent real magnetic field changes.

6.3 Magnetic Field Interpolation Overview

The fixed probes are used to track the evolution of the dipole, normal quadrupole, skew quadrupole, and normal sextupole magnetic field multipole components at all times between trolley runs. As the trolley passes underneath each fixed probe station during a trolley run, the 17 trolley probes and four or six fixed probes sample the magnetic field at the same time and azimuthal location. A calibration can be done at this time, relating the magnetic field components measured by the two systems. After this time, only the fixed probes can be used to track the magnetic field evolution at that azimuthal location until the trolley returns, typically three days later.

The basic interpolation process is as follows:

1. Determine the time at which the sensitive regions (petroleum jelly samples) of the trolley probes are directly underneath the sensitive regions of the fixed probes at all fixed probe stations.

2. Determine the trolley dipole, normal quadrupole, skew quadrupole, and normal sextupole at this time.

3. Determine the fixed probe dipole, normal quadrupole, skew quadrupole, and normal sextupole at this time.

4. Track changes of the magnetic field using only the fixed probes.

5. Evaluate the magnetic field predictions against new trolley measurements at the time of the second trolley passing.

6. Use the two trolley measurements to correct the fixed probe predictions at times between the trolley runs in order to provide the best estimates of the magnetic field.

Interpolation is done for each fixed probe station individually. Additionally, an azimuthally averaged magnetic field is predicted. Details on each step listed above are provided in the following subsections. Tracking of the higher order magnetic field multipole moments relies upon trolley measurements and simulations, and is discussed in Sec. 6.6.2.

6.4 Data Quality

Data quality must be taken into account before beginning interpolation. The quality of an FID recorded from a pNMR probe depends on many factors. For both the trolley probes and the fixed probes, large magnetic field gradients lead to very short FID signals due to spin decoherence. Such FIDs are difficult to reliably extract frequencies from and are flagged as problematic by the magnetic field data quality group based on amplitude, length, and power. Additionally, the fixed probe system occasionally experienced false triggers which led to nonphysical FIDs, which are also flagged based on amplitude, length, and power. Finally, the trolley is constantly in motion, and as it moves it occasionally experiences jolts (it jerks/pitches/rolls). This sudden movement generates eddy currents in the trolley shell, creating a real, additional magnetic field at the location of the probes which is not experienced by muons. This additional magnetic field leads to a "spike" in extracted trolley frequencies.

Considering the trolley first, spikes are the most common issue. These anomalies, which each affect only one trolley measurement (event), can be detected by comparing each trolley event to a subset of events taken immediately before and after. The mean and RMS of the extracted frequencies from a given trolley probe near the event in question are calculated.

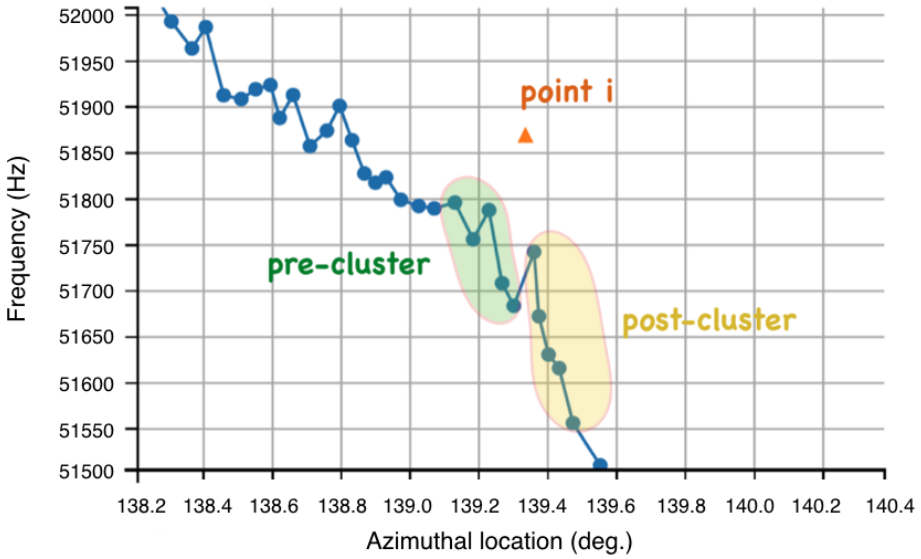

Figure 6.6 – To determine whether a trolley measurement (orange point) has been affected by eddy currents in the trolley shell, the measurement in question is compared to clusters of measurements taken immediately before and after (green and yellow groups). If the extracted frequency is either above or below the mean of both neighboring clusters by greater than 10 Hz, it is considered a spike event and is replaced by a linearly interpolated value. Image credit: [99]

If a measured frequency is either higher or lower than the mean of both of its neighboring clusters by a given threshold (10 Hz was chosen), it is considered a spike event and is replaced by a linearly interpolated value. Fig. 6.6 shows a graphical representation of a suspected trolley spike event and its neighboring clusters, while Fig. 6.7 shows that the choice of spike detection threshold has a sub-10 ppb effect on the azimuthally averaged trolley dipole [99].

Each fixed probe is different and must be characterized. Fixed probe resolution is calculated as the RMS of frequency differences between consecutive measurements. The resolutions of all 378 fixed probes over a 12 hour period are shown in Fig. 6.8 [102]. While the magnetic field changes as a function of time, this characterization assumes that it does not change significantly in the two seconds between fixed probe measurements.

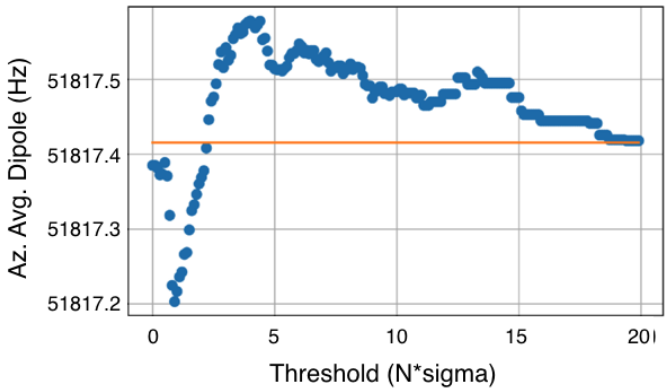

Figure 6.7 – The effect of the spike detection threshold on the azimuthally averaged trolley dipole. Sigma represents the average RMS of trolley measurements, typically on the order of 30 Hz. A factor of 20 in the threshold has a 0.4 Hz, or 6 ppb, effect. Image credit: [99]

The majority of fixed probes with poor resolution, defined as >20 Hz, are located in the inflector vacuum chamber, between 345°-15°. Of the six fixed probe stations in this vacuum chamber, three stations contain probes with good resolutions, while the probes at the other three stations are affected by large magnetic field gradients. Rather than including data from these poorly performing fixed probes in an azimuthal average, an average of the fixed probe measurements from the neighboring stations is used instead. The probes at these stations do a better job of tracking the magnetic field evolution measured by the trolley, which will be discussed in Sec. 6.5.5.

Finally, there were periods of time when the fixed probes suffered from interference with an external system. The pulser cabinet for the quadrupoles (Sec. 2.4) faces the electronics rack holding the fixed probe NMR pulsing hardware. Due to inadequate shielding of both systems, the pulser cabinet occasionally radiated a signal which initiated the generation of spurious $\pi/2$ pulses in the fixed probe system. These spurious pulses led to distorted FID signals, two examples of which are shown in Fig. 6.9, which the frequency extraction algorithm cannot properly handle. Improperly extracted frequencies manifest as spikes when

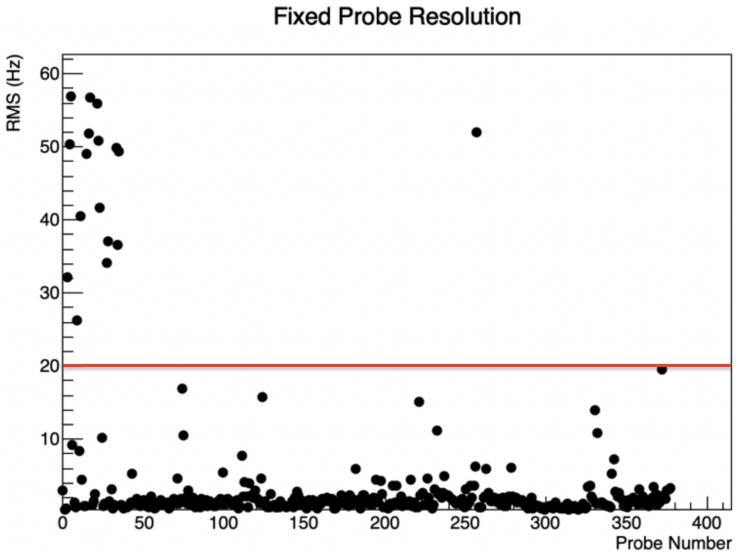

(a) Probe resolution.

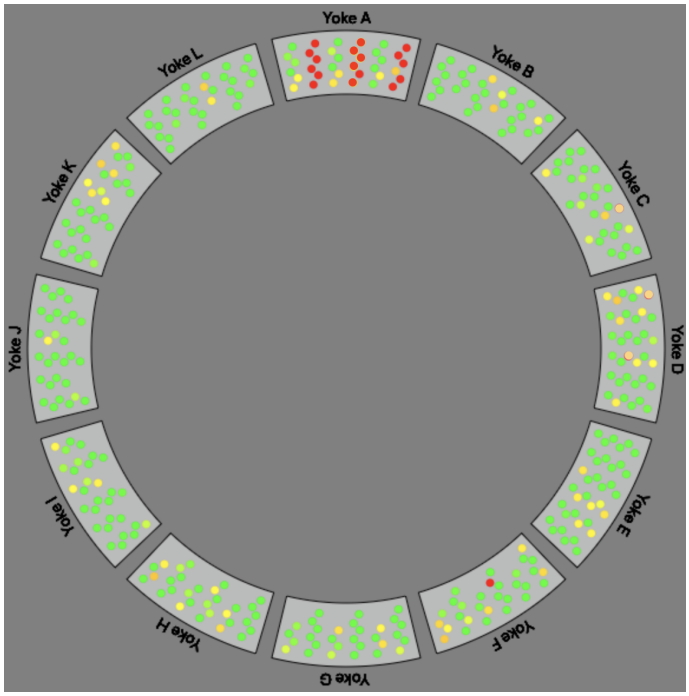

(b) Probe resolution distribution.

Figure 6.8 – a) Fixed probe resolution is defined as the RMS of frequency differences between consecutive measurements. 12 hours of data (∼25,000 measurements) were analyzed to calculate the resolutions of all 378 probes. A resolution >20 Hz is considered bad. b) The distribution of probe resolutions. Green probes perform well, while red probes perform poorly. Orange probes have resolutions in the range 2-20 Hz. For the interpolation analysis, data from the fixed probes at the three bad stations (1, 3, and 5) in Yoke A are not used, while all other fixed probes are included in the analysis.

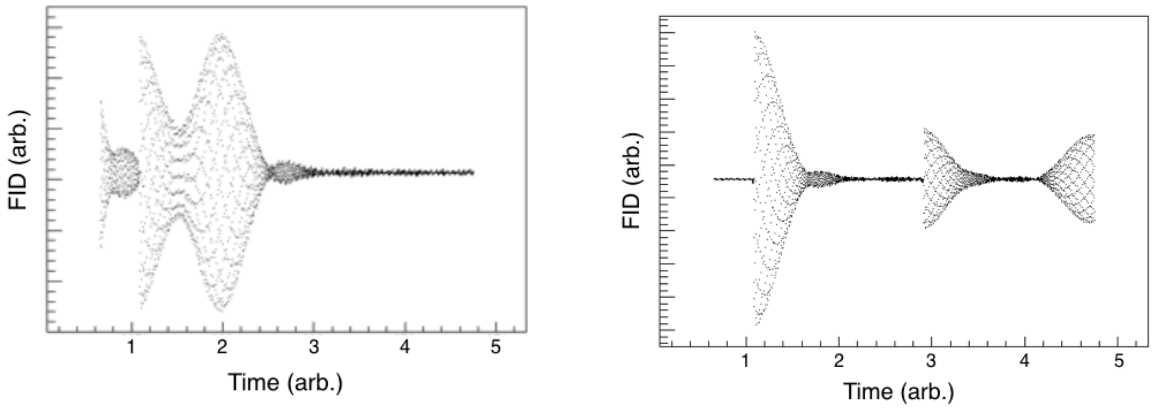

(a) (b)

Figure 6.9 – Throughout run 1, there was interference between the fixed probe system and the quadrupole pulser cabinet. The pulser cabinet occasionally radiated signals which caused the generation of spurious $\pi/2$ pulses in the fixed probe system. This led to unphysical FIDs, two examples of which are shown with axes of arbitrary units.

compared to neighboring measurements. This interference was mitigated at the end of run 1 and will not be an issue in the analysis of future datasets.

The magnetic field data quality team flags suspicious FIDs based on their amplitude, length, and power. Because flagged events do not correspond to real magnetic field changes, these frequency spikes are replaced by interpolated values, using measurements taken immediately before and after the interference event. Fig. 6.10 shows an example of fixed probe frequency spikes and their replacement values.

6.5 Interpolation Steps

6.5.1 Alignment of the Fixed Probes and Trolley Probes

The first step in magnetic field interpolation is calibrating the fixed probes to the trolley probes, relating the measurements of the two systems. This process must be done at the

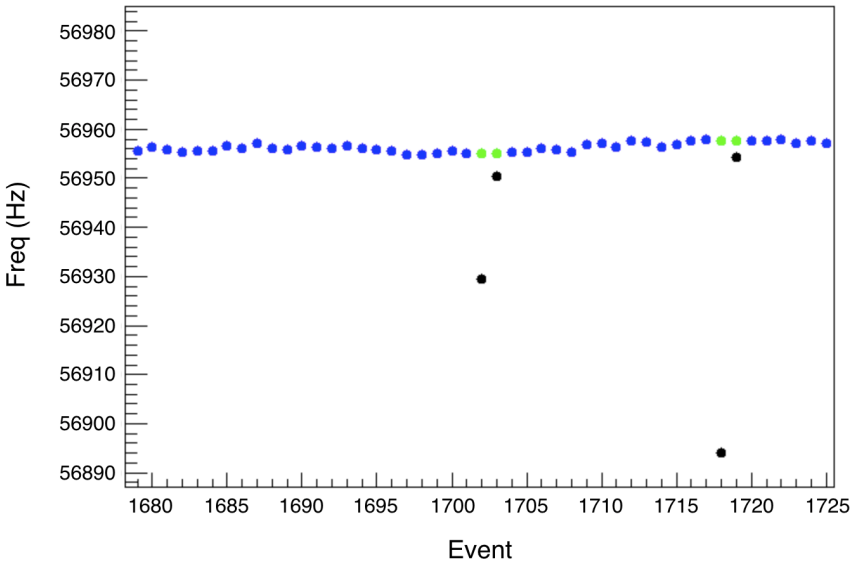

Figure 6.10 – Fixed probe spikes do not correspond to real magnetic field changes, but rather to events that were affected by interference between the fixed probe and quadrupole pulser systems. The incorrect frequency values (black points) are replaced with linearly interpolated values (green points), where good, neighboring measurements (a subset of blue points) are used for interpolation.

time when the pNMR probe active regions (the petroleum jelly samples) are at the same azimuthal location[2]. This calibration is repeated during each trolley run.

The trolley itself perturbs the magnetic field in the muon storage region, and as such its magnetic footprint is seen by the fixed probes as it passes by. The trolley magnetic footprint, shown in Fig. 6.11, was measured at Argonne National Laboratory in an MRI magnet repurposed for use in the $g-2$ experiment. A pNMR probe, identical to the fixed probes, was scanned along the length of the trolley at a distance of 7 cm below the trolley shell, comparable to the distance between the trolley and the fixed probes. The magnetic field perturbation caused by the trolley was computed as the difference between these measurements and measurements taken in an identical scan without the trolley present [101]. The distance between the plane of trolley probe active regions, determined by applying alternating magnetic field gradients (the delta-B method described in Sec. 3.5), and the location on the trolley that produces the maximum magnetic field perturbation is 339.5±2.0 mm, corresponding to 2.70±0.02° in the storage ring.

In order to determine the time of overlap of the trolley and fixed probe active regions at each fixed probe station, the trolley's position at the time of maximum perturbation on each fixed probe is first found. In a typical trolley run, the trolley is pulled around the storage ring circumference in the counterclockwise, or upstream, direction, while the 17 pNMR probes are housed in the downstream end of the trolley. The overlap thus occurs when the trolley is 2.70° upstream of this location.

The trolley position at the time of maximum perturbation is determined by fitting each fixed probe's measurement of the trolley footprint to a sum of three Gaussian curves

$$y = [0] + [1]\left(e^{-a[2](x-[3])^2} + be^{-c[2](x-[3]-d)^2} + fe^{-g[2](x-[3]-h)^2}\right), \tag{6.2}$$

where [0], [1], [2], and [3] are fit parameters and the values of a, b, c, d, f, g, and h are listed in Tab. 6.1. The values of a, b, c, f, and g were determined by fitting characteristic trolley perturbations in many fixed probes and serve to keep the ratios of the widths and heights of

[2]This time will be referred to as the time of active region overlap.

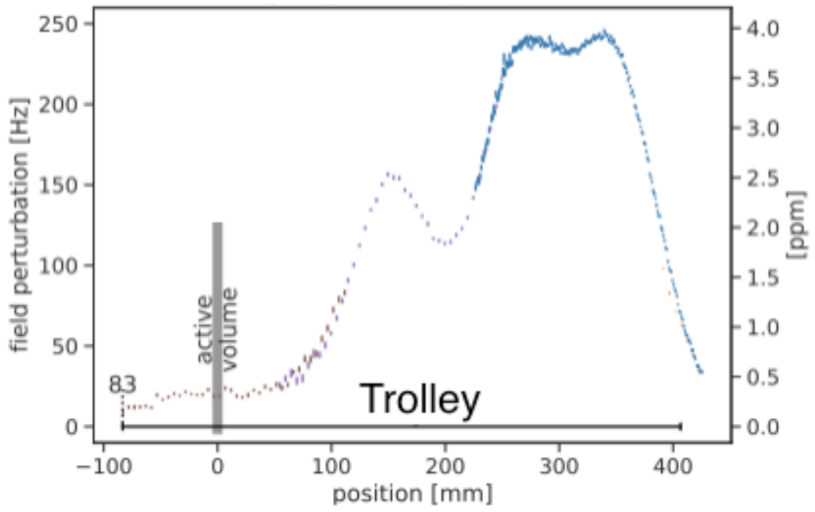

Figure 6.11 – The trolley itself perturbs the storage region magnetic field. A pNMR probe was scanned along the trolley's length in an MRI magnet located at Argonne National Laboratory. The trolley's magnetic footprint was extracted by comparing these measurements to measurements taken without the trolley present. The difference is shown as a function of distance from the plane of trolley probe active regions. Image credit: [101]

the three Gaussian curves constant. The values of d and h help with the fitting procedure, ensuring the proper spatial ordering of the three Gaussian curves [103]. Fit parameter [3] is the time corresponding to the maximum of the tallest Gaussian curve, the time when the most magnetic part of the trolley is azimuthally aligned with the fixed probe. Due to installation variations, the active regions of each probe in a fixed probe station are not at the exact same azimuthal locations, leading to different active region overlap times. Each station is thus assigned an active region overlap time that is the average of the overlap times of all of the probes at this location. A fit of the trolley magnetic footprint as seen by a fixed probe is shown in Fig. 6.12.

This method for determining the active region overlap time relies on knowing the trolley position at all times during a given trolley run, but assumes nothing about the repeatability of position determination during different trolley runs. While the repeatability is good for the

Parameter	a	b	c	d	f	g	h
Value	0.0118	0.48	0.0326	15	0.13	0.0112	30
Purpose	Gaussian 1 width (sec)	Gaussian 2 relative amplitude (Hz)	Gaussian 2 width (sec)	Gaussian 2 spatial offset (sec)	Gaussian 3 relative amplitude (Hz)	Gaussian 3 width (sec)	Gaussian 3 spatial offset (sec)

Table 6.1 – Parameters of the trolley magnetic footprint fit function, Eq. 6.2.

method which uses the barcode reader (Sec. 3.4.1), the trolley positions determined using the motor encoders are not consistent between trolley runs. Determining the time and associated trolley position of active region overlap during every trolley run, as opposed to determining active region overlap positions one time and evaluating the trolley measurements at the same positions for all subsequent trolley runs, is robust to all trolley position extraction methods.

6.5.2 Determining the Trolley Magnetic Field Components

After determining the time and trolley position during active region overlap, the trolley multipole components at this time are extracted. Rather than using only the one measurement corresponding to the time of active region overlap, multiple measurements are averaged.

The "interpolation discontinuity" of a fixed probe station is defined as the difference between the predicted magnetic field at the time of a second trolley passing and the actual magnetic field as measured by the trolley:

$$\text{discontinuity} = \mathrm{B}_{\text{actual}}\left(\mathrm{t}_{\text{trolley}}\right) - \mathrm{B}_{\text{predicted}}\left(\mathrm{t}_{\text{trolley}}\right). \tag{6.3}$$

The means and standard deviations of interpolation discontinuity distributions as a function of the number of trolley measurements averaged were used to determine how many trolley measurements to average at each fixed probe station location. Fig. 6.13 shows a characteristic

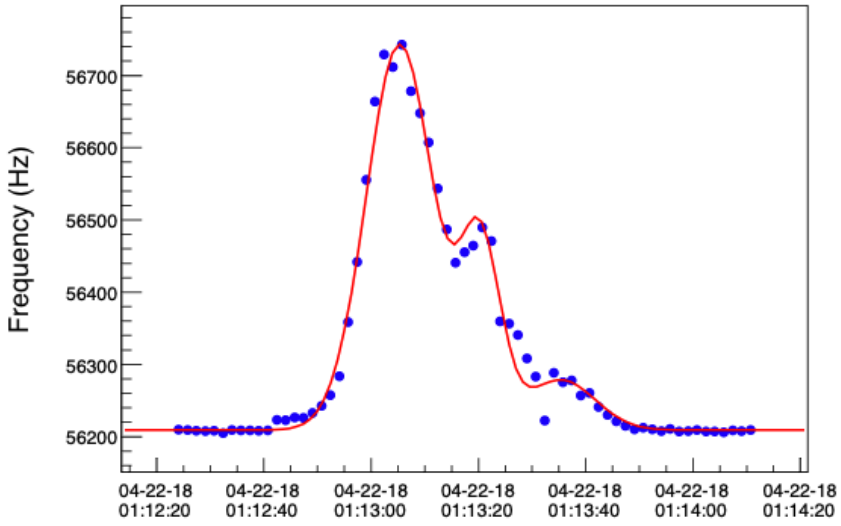

Figure 6.12 – As the trolley passes a fixed probe, it perturbs the magnetic field measured by the probe. The perturbation is fit to a sum of three Gaussian curves to extract the time of maximum perturbation.

dipole interpolation discontinuity histogram, while Fig. 6.14 shows the means and standard deviations of the interpolation discontinuity distributions for a characteristic pair of trolley runs when different numbers of trolley measurements were averaged together.

The ideal number of trolley measurements to average was chosen to be 49 (the measurement closest to active region overlap, in addition to 24 measurements on either side). The trolley moves approximately 0.04° in the time it takes to make measurements with the 17 probes, such that averaging 49 trolley measurements is equivalent to averaging data over an angular extent of approximately 2°. Although the standard deviations of the distributions continue to decrease as the azimuthal extent of trolley measurements averaged increases, the means of the distributions (particularly the dipole and normal quadrupole) begin to increase as more measurements are used and the magnetic field predictions become worse. The choice of 49 measurements represents the best balance of statistics and correlation between

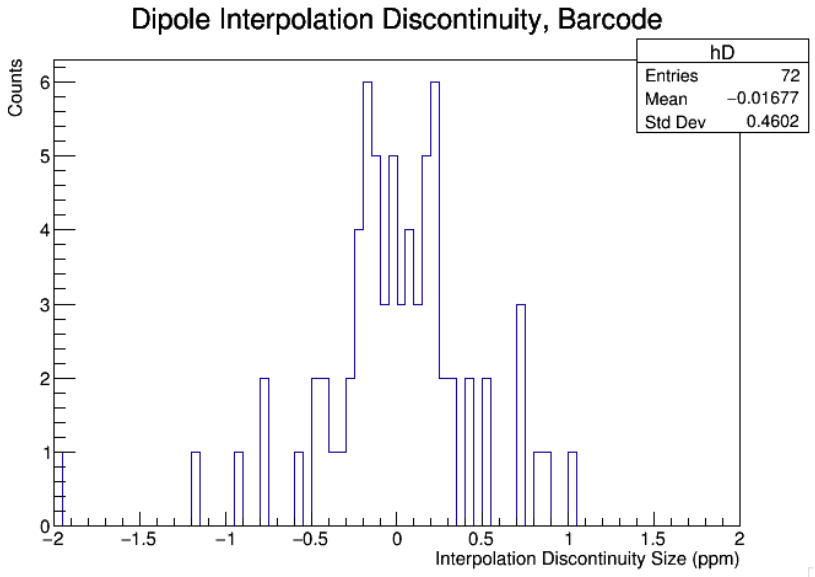

Figure 6.13 – The interpolation discontinuity is defined as the difference between the predicted magnetic field component from fixed probe tracking and the measured trolley magnetic field component at the time of a second trolley run. A characteristic histogram of the dipole interpolation discontinuities for all fixed probe stations from one trolley run pair is pictured. The distribution is described by -0.017±0.46 ppm

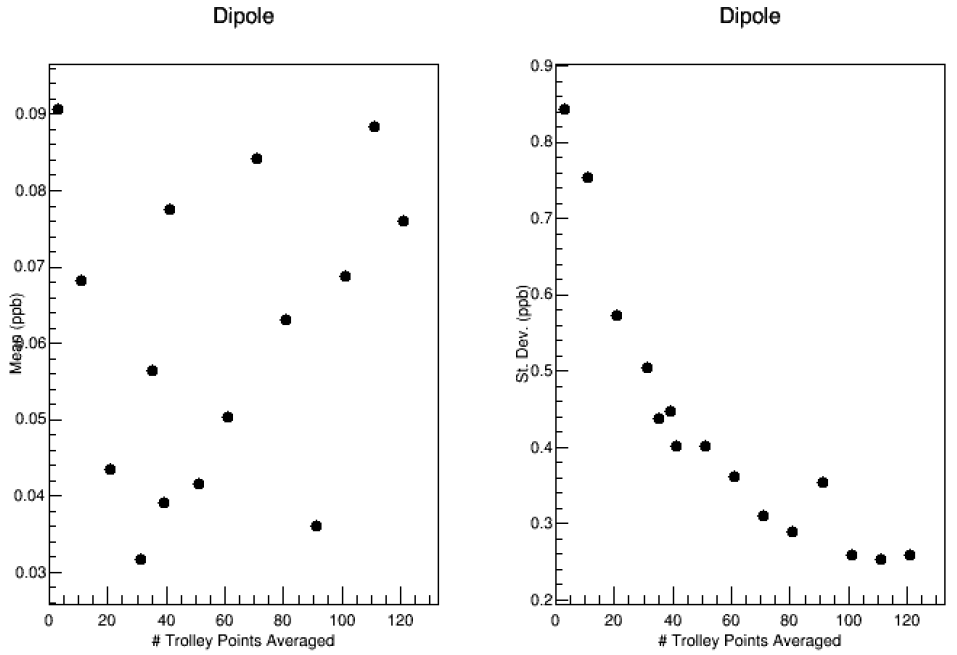

(a) Dipole.

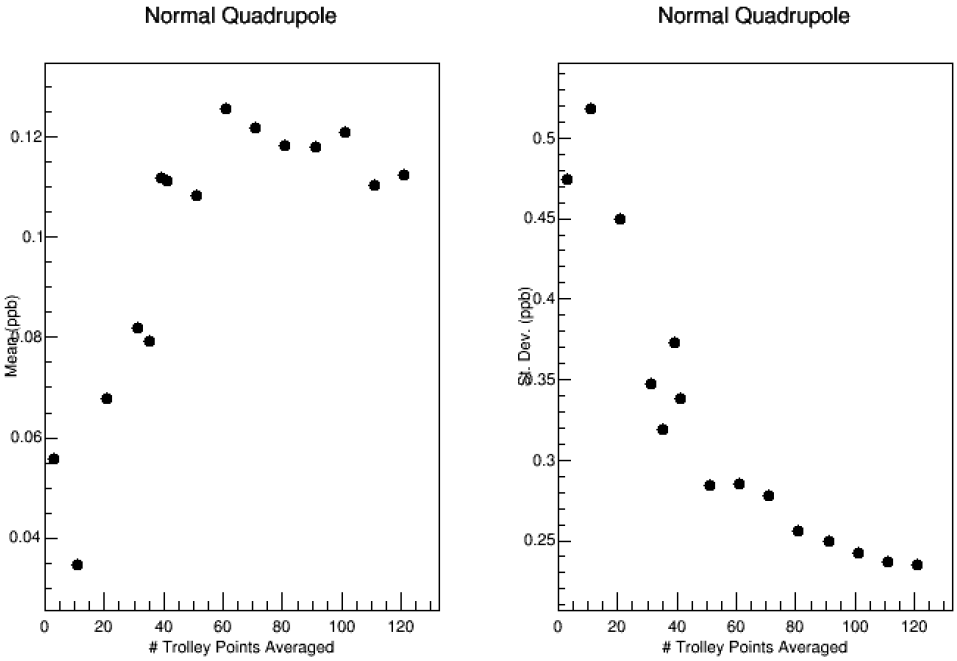

(b) Normal quadrupole.

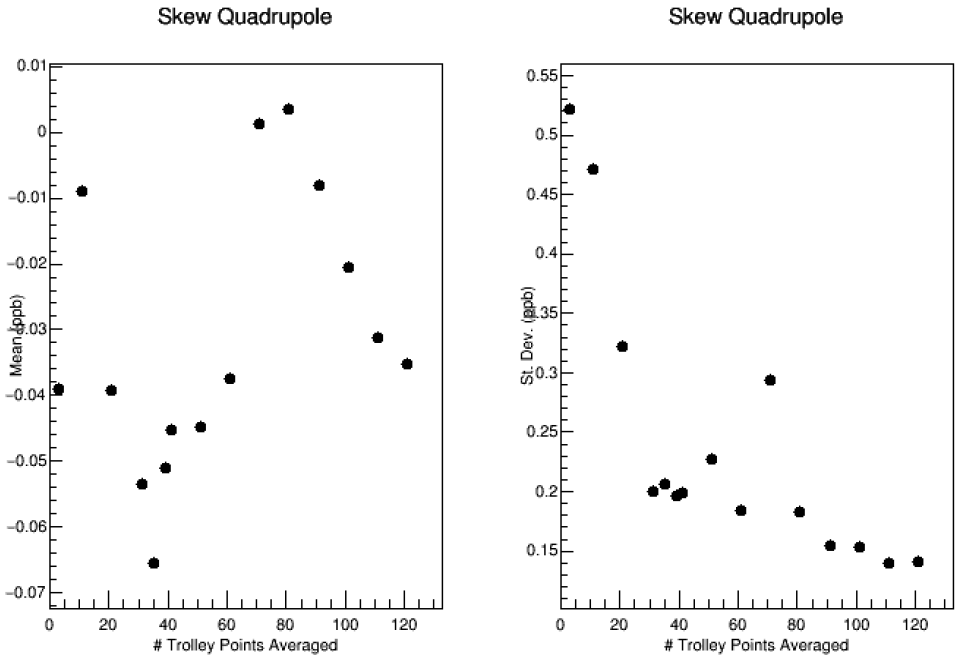

(c) Skew quadrupole.

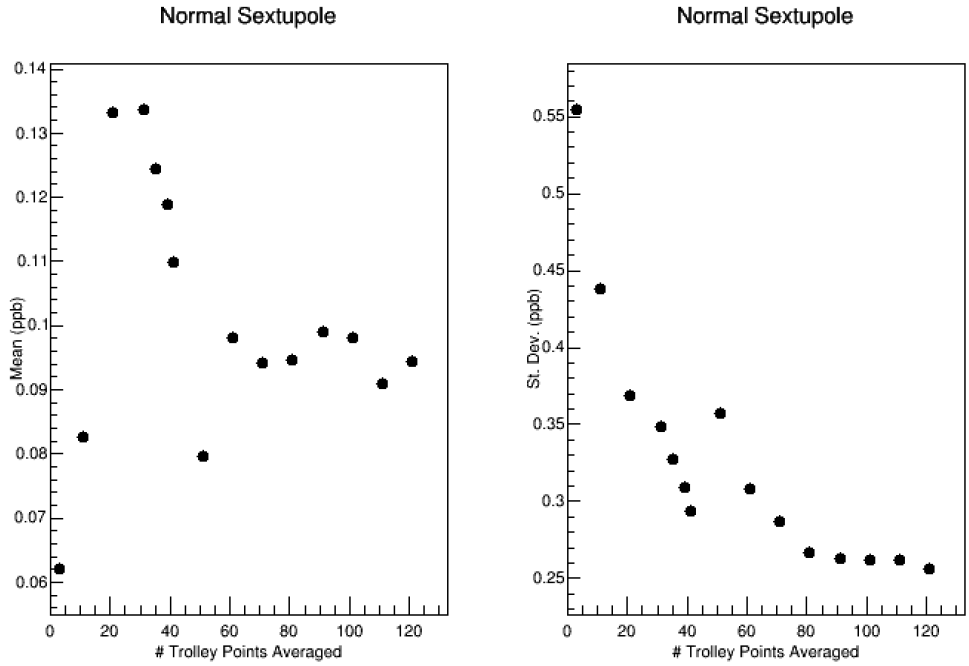

(d) Normal sextupole.

Figure 6.14 – The means and standard deviations of the interpolation discontinuity distributions when different numbers of trolley measurements are averaged together to extract the trolley magnetic field multipoles when the trolley passes a fixed probe station.

the trolley and fixed probe measurements, despite the fact that the fixed probes are sensitive to magnetic field changes over an azimuthal extent greater than 2°.

6.5.3 Determining the Fixed Probe Magnetic Field Components

Due to their locations and small numbers[3] the fixed probes are not as well suited to a multipole expansion of the magnetic field as the trolley probes. However, analogous magnetic field moments can still be calculated from their measurements (recall that the magnetic field multipole moments are pictured in Fig. 3.9). The dipole magnetic field component is a measure of the average vertical magnetic field in the muon storage region and can be calculated using the fixed probes at a given azimuthal location by taking an average. For fixed probe stations with six probes, the frequencies measured by all six probes are averaged. For stations with four probes, only the two probes at the radially centered location are used, because using all four probes would introduce a bias due to the asymmetric sampling.

The normal quadrupole magnetic field component is a linear variation in magnetic field strength as a function of radial position. It can be calculated from fixed probe measurements as radial differences (outer-inner measurements for stations with six probes and outer-middle for stations with four). The skew quadrupole magnetic field component is a linear variation in magnetic field strength as a function of vertical position. It can be calculated as the average of top probe - bottom probe measurement differences. Finally, the normal sextupole magnetic field component can be calculated from measurements at six probe fixed probe stations as (outer + inner - 2×middle), but can not be tracked by four probe stations. All calculated differences are scaled to be relative to 4.5 cm, the same as is done for the trolley multipoles.

Unlike the trolley multipoles, the fixed probe multipoles are not independent of one another. In particular, the presence of a normal sextupole causes the fixed probes to sense an additional dipole magnetic field component. This is because, in the presence of a normal

[3]Recall, each fixed probe station contains either four or six probes.

sextupole magnetic field component, the fixed probes all sense a magnetic field of the same sign, as can be seen in the normal sextupole image of Fig. 3.9. This can be compared to the skew sextupole, where the average of the contributions to the fixed probes cancel. This mixing of multipole moments is corrected for by calculating the normal sextupole contribution to the calculated fixed probe dipole and then subtracting it. Additionally, all fixed probes at the six stations in the inflector vacuum chamber are radially offset from their nominal positions by 1 cm, which causes the normal quadrupole to mix into the fixed probe dipole. This is corrected for in the same manner as the normal sextupole.

These schemes for calculating the fixed probe multipoles can be tested using studies where the trolley sits stationary under a fixed probe station for a long period of time. The trolley and fixed probe multipoles during a five hour long stationary trolley run are shown in Fig. 6.15. The differences between the multipoles of the two systems are shown in Fig. 6.16. The fixed probes do not perfectly track the magnetic field changes measured by the trolley probes, which is attributed to multiple effects. The most dominant effect is the evolution of higher order magnetic field multipole components that can not be tracked which affect the calculation of fixed probe multipoles.

During a non-stationary trolley run, fixed probe multipoles can be easily calculated at times before and after the trolley passing. However, while the trolley magnetic footprint is visible to a fixed probe, special care must be taken, as it is the magnetic field that the fixed probe would have measured without the trolley present that must be known. Rather than using the fit described above, this is determined by fitting the fixed probe trends before and after the trolley passing to a linear line and doing linear interpolation, as shown in Fig. 6.17.

When doing such a fit, a number of measurements on either side of the trolley perturbation are used for the linear interpolation. The collections of measurements are known as "sidebands." The extracted fixed probe frequency at the time of active region overlap is shown in Fig. 6.18 as a function of the distance between the sidebands. The extracted frequency flattens out when the sidebands are chosen to be greater than 22° apart [102]. As discussed in Sec. 6.5.1, the angular distance between the most magnetic part of the trolley

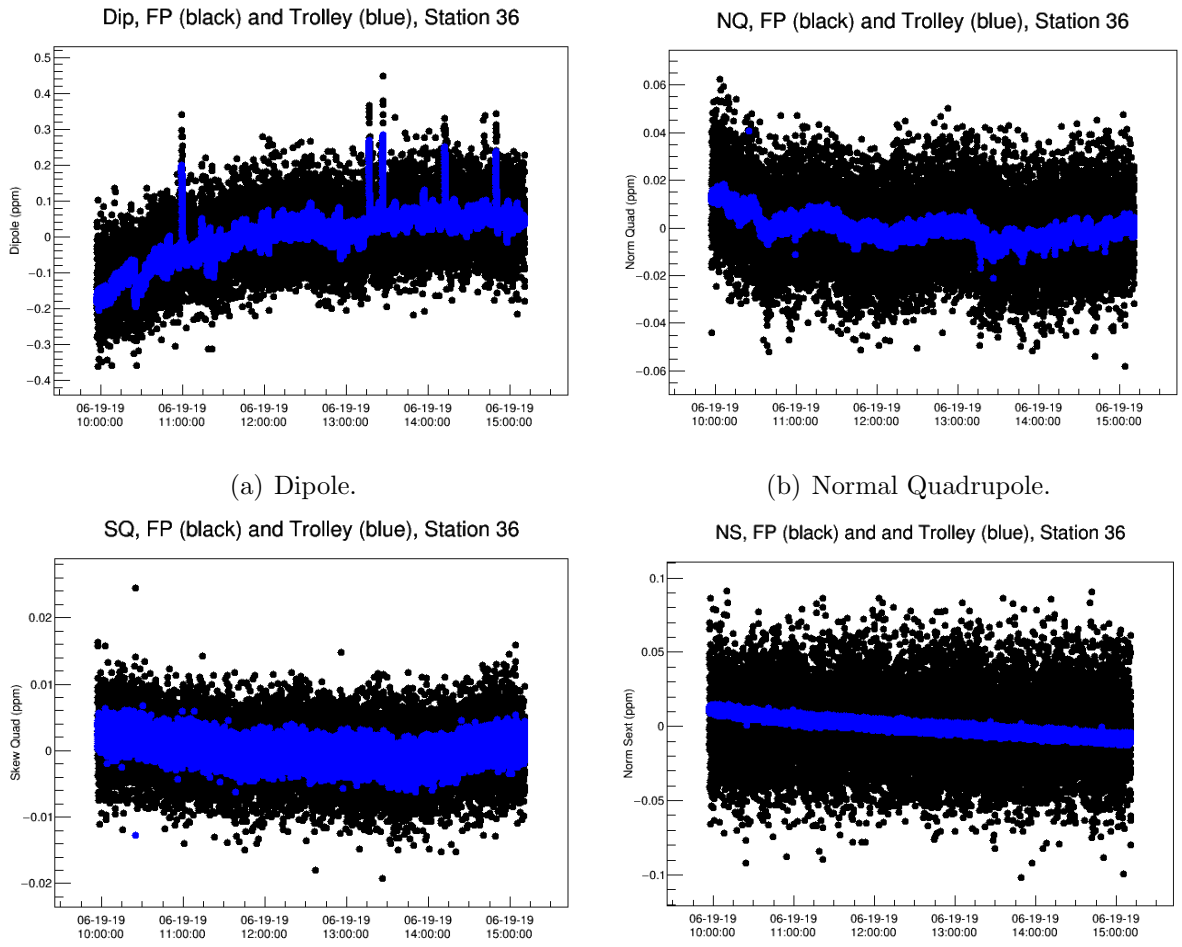

(a) Dipole.

(b) Normal Quadrupole.

(c) Skew Quadrupole.

(d) Normal Sextupole.

Figure 6.15 – A comparison of the trolley and fixed probe dipole, normal quadrupole, skew quadrupole, and normal sextupole during a five hour run where the trolley was parked stationary underneath a fixed probe station. The trolley multipoles are drawn in blue while the fixed probe multipoles are drawn in black. For all curves, the average value has been subtracted from each point.

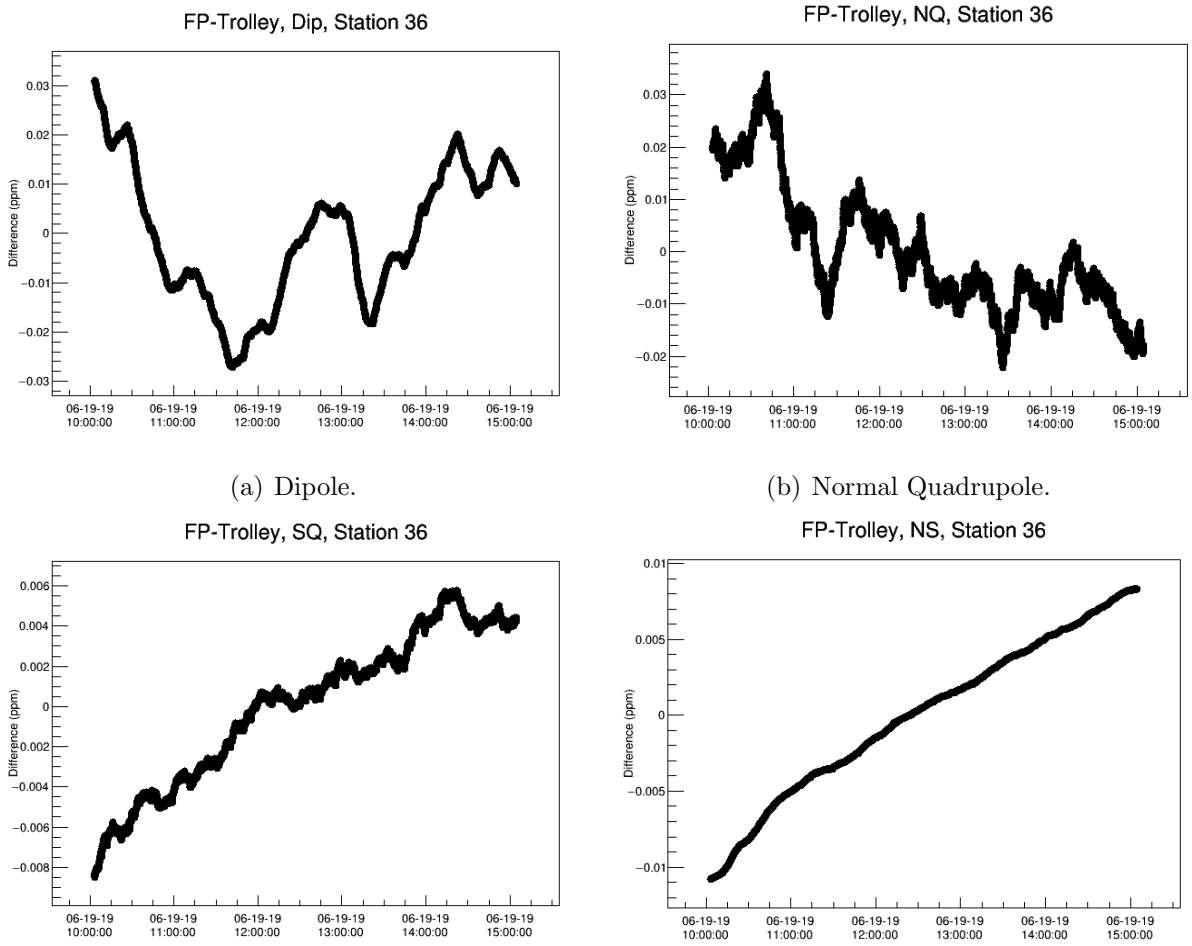

(a) Dipole.

(b) Normal Quadrupole.

(c) Skew Quadrupole.

(d) Normal Sextupole.

Figure 6.16 – The evolution of the difference between the trolley and fixed probe dipole, normal quadrupole, skew quadrupole, and normal sextupole during a five hour run where the trolley was parked stationary underneath a fixed probe station (the data of Fig. 6.15). All curves have been shifted to be centered approximately around zero and a 1000 second moving average is used to reveal finer details. The differences between the measurements of the two systems are attributed to multiple effects, the most dominant of which is changing higher order magnetic field multipole components which affect the calculation of fixed probe multipoles, but that the fixed probes can not track.

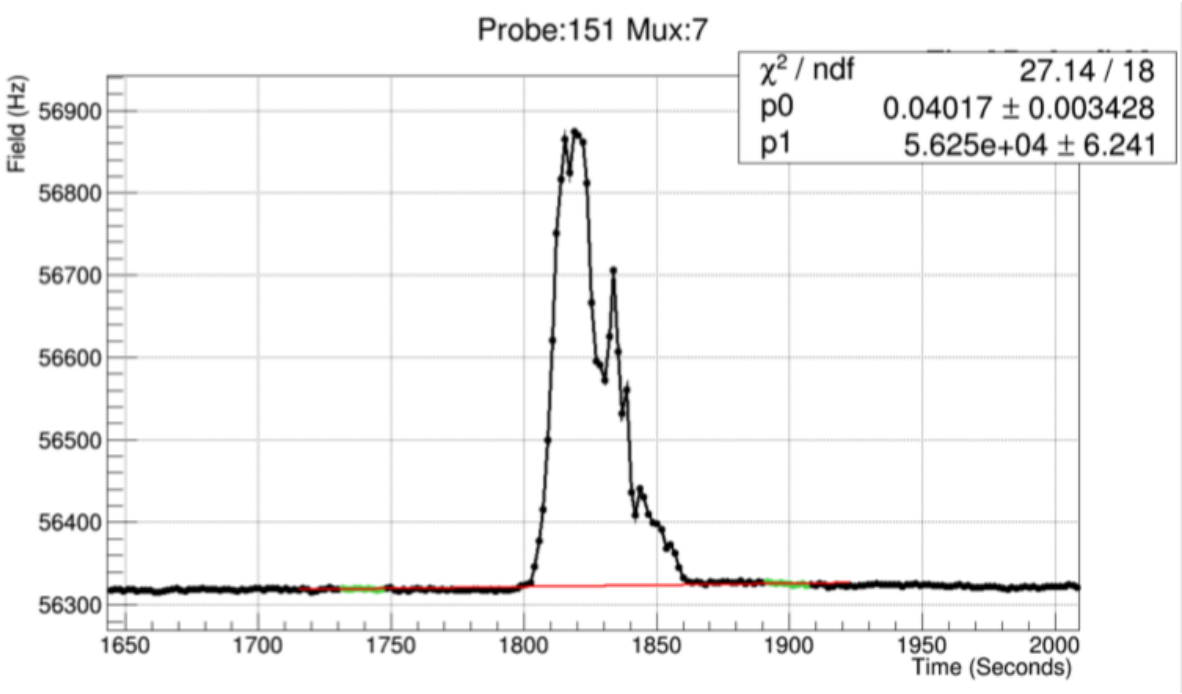

Figure 6.17 – As the trolley passes underneath a fixed probe, the magnetic field measured by the fixed probe is perturbed. The fixed probe trends before and after the trolley passing (green points, referred to as "sidebands") are fit to a linear line, allowing for linear interpolation of the frequencies the fixed probe would have measured without the trolley present.

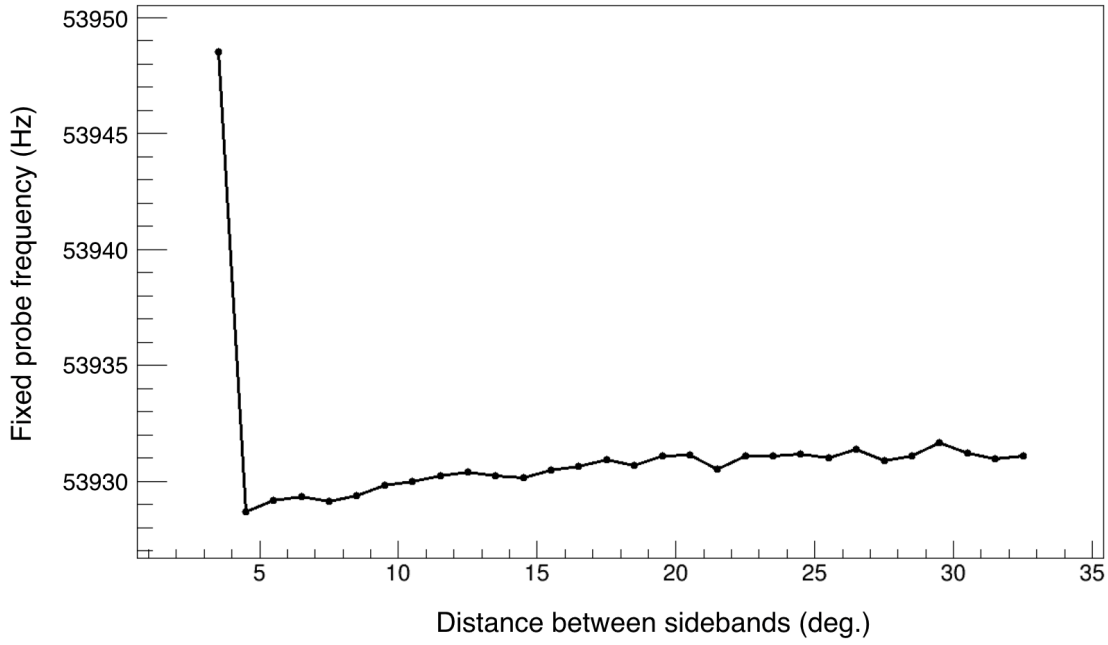

Figure 6.18 – Linear interpolation is used to remove the effect of the trolley magnetic footprint on fixed probe measurements during trolley runs (Fig. 6.17). In this process, special care must be taken to use measurements ("sidebands") far enough away from the trolley's magnetic footprint. The extracted frequency for a characteristic fixed probe is shown as a function of the distance between the measurements used for linear interpolation. The plot gets asymptotically flat when the sidebands are 20° apart. Image credit: [102]

and the plane of trolley pNMR probe active regions is small, only 2.70°. However, trolley motion creates a much larger footprint, which is about 20° wide. The mechanism which causes this large footprint is not fully understood. Overall, the choice of sidebands used for linear interpolation creates a 2 Hz, or 32 ppb, uncertainty on the fixed probe multipoles calculated when the trolley is present.

6.5.4 Making Magnetic Field Predictions

The magnetic field interpolation process begins at each fixed probe station when the trolley passes by and the station's fixed probes are calibrated to the trolley probes. At the time of active region overlap, the fixed probe and trolley measurements do not agree, because the two sets of probes are located at different places within the storage ring. Despite these physical offsets, the two sets of probes measure the magnetic field at the same azimuthal location at the same time, so the differences are treated as offsets.

Calibrated trolley measurements are used as the absolute starting point for magnetic field interpolation because the trolley probes directly sample the magnetic field in the muon storage region. The evolution of the fixed probe multipoles are tied to these measurements. At any time i after a trolley passing, the magnetic field prediction is calculated as

$$B[i] = B[i-1] + \left(B_{FP}[i] - B_{FP}[i-1]\right), \tag{6.4}$$

where $B[i-1]$ is the last calculated magnetic field value ($B[0]$ is the trolley measurement), and $B_{FP}[i]$ and $B_{FP}[i-1]$ are the current and most recently calculated fixed probe multipoles.

If magnetic field interpolation worked perfectly, the interpolation discontinuities for all fixed probe stations (Eq. 6.3) would be on the order of the average fixed probe resolution. However, this is not the case. A dipole interpolation plot for one fixed probe station is shown in Fig. 6.19, with a zoomed view of the time of the second trolley passing shown in Fig. 6.20. A 200 ppb interpolation discontinuity is visible.

With trolley measurements taken as truth values, interpolation uncertainties should scale with temporal distance from the nearest trolley run. The largest uncertainty should occur directly between trolley runs. The previous discussion used only the first trolley run to make magnetic field evolution predictions. The same process can be followed in reverse, using the second trolley run as the starting point and using the fixed probes to backtrack the magnetic field evolution. To remove the interpolation discontinuity from a fixed probe station prediction and produce a prediction that is tied to measurements from both trolley runs, the prediction at all times between trolley runs is calculated as a time-weighted average

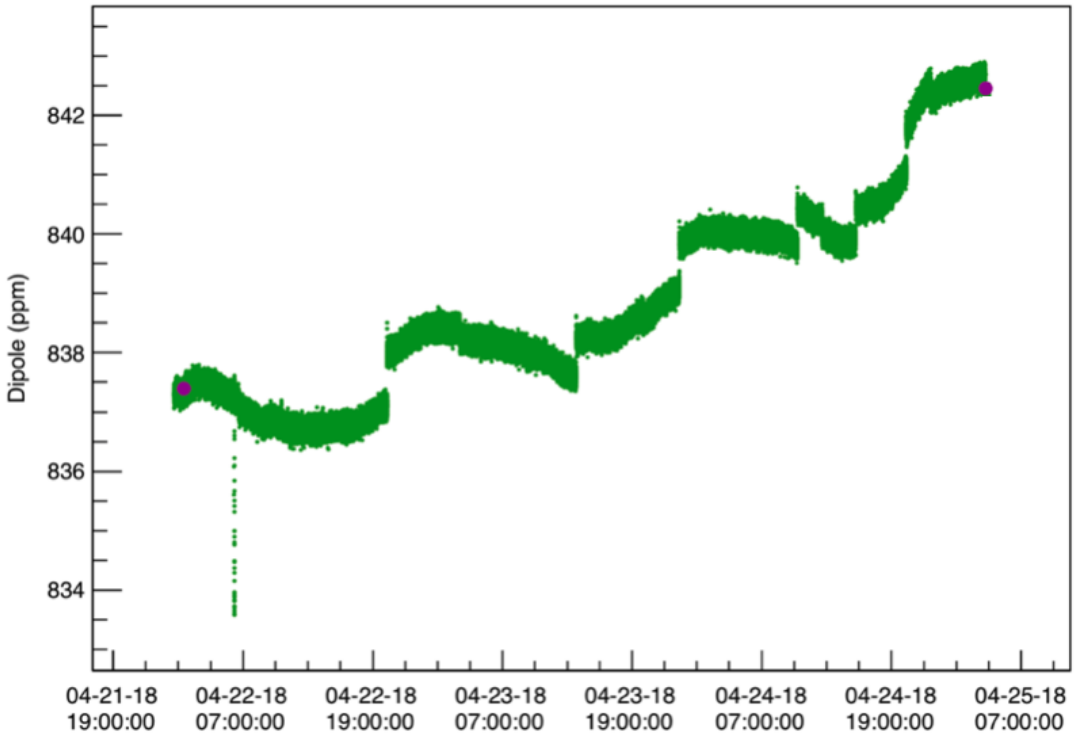

Figure 6.19 – A representative dipole interpolation plot for one fixed probe station. Purple points represent the trolley dipole during consecutive trolley runs while green points are the interpolated magnetic field evolution, calculated using fixed probe measurements.

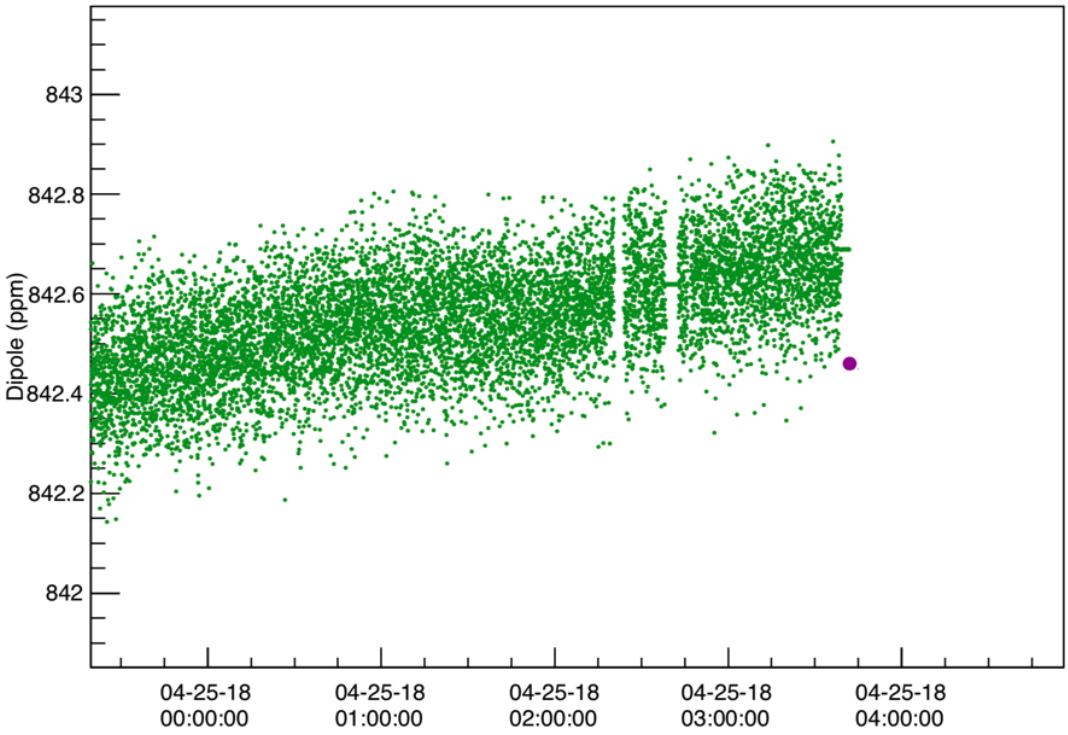

Figure 6.20 – A zoomed in view of the second trolley passing shown in Fig. 6.19. There is an approximately 200 part per billion difference between the predicted magnetic field (green points) and the magnetic field measured by the trolley (purple point) at the time of active region overlap, known as the interpolation discontinuity.

of the two predictions (forward and backward tracking). This calculation assumes a smooth, linear growth of the interpolation discontinuity during one-directional tracking. Details of this tying process are discussed in Sec. 6.5.5, in the context of the azimuthally averaged magnetic field. In cases where there is only one good trolley run associated with a dataset, tracking is done in only the forward or backward direction, leading to higher uncertainties as discussed in Sec. 6.6.3.

6.5.5 Azimuthal Averaging

Run 1 magnetic field interpolation analysis concentrates on tracking the azimuthally averaged magnetic field, which in practice requires doing two separate azimuthal averages: one of the trolley multipoles and one of the fixed probes multipoles. These will be discussed separately.

Trolley Averaging

The trolley traverses the full 360° of the storage ring magnet during each trolley run, sampling the magnetic field along the way. However, the trolley step size as it is pulled around the storage ring is not constant, complicating azimuthal averaging. Before averaging begins, the data is sorted by azimuthal position. There is approximately half of a degree of the storage ring, at the trolley drive (the location of the motors which pull the trolley), that gets measured at both the beginning and end of each trolley run. Were the data not sorted, the magnetic field in this region of the storage ring would enter twice into two of the averages described below.

The most naive averaging method gives equal weight to each trolley measurement. In this method, referred to as the "straight average" method, an average is calculated by computing the sum of all trolley measurements and then dividing by the total number of measurements. Because of the uneven trolley step sizes, this method more heavily weights the magnetic field in areas of the storage ring where the trolley moved with smaller steps. This method therefore isn't used in Bloch interpolation.

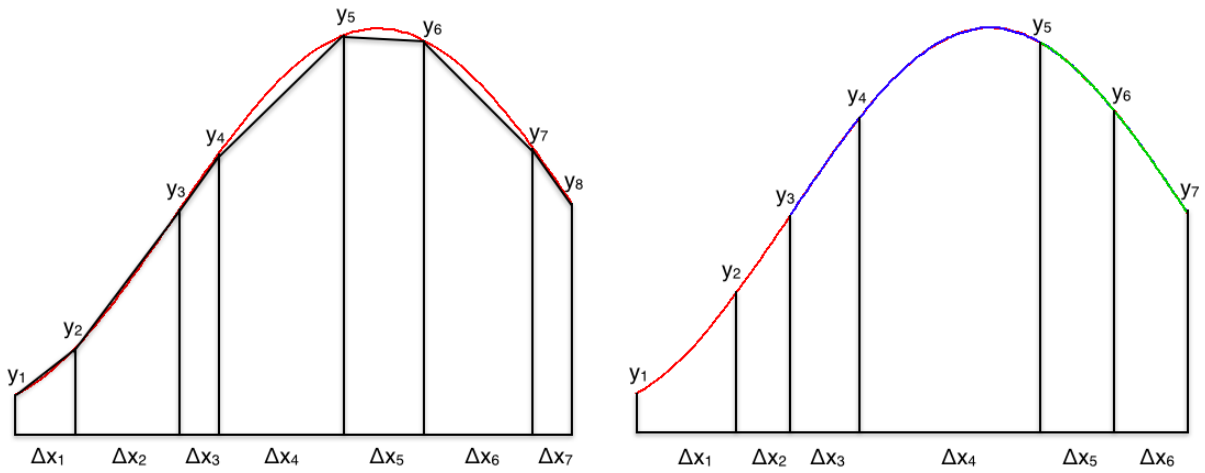

(a) Trapezoidal Integration.

(b) Simpson's Integration.

Figure 6.21 – In trapezoidal averaging, the area under a curve is determined by connecting adjacent points with a linear line and calculating the sum of the areas of the resultant trapezoids. In Simpson's averaging, three adjacent points are connected by a parabola, and the area of the resultant shapes are summed. The implementations of both methods are robust to uneven distances between points. To compute an average value using either method, the calculated area is divided by the total width of all measurements.

Two alternative averaging methods were tested: trapezoidal averaging and Simpson's averaging. In the trapezoidal method, the area under the curve between two points is approximated by connecting the two points with a straight line and calculating the area of the resultant trapezoid. The total area is divided by the total width, resulting in an average value. The Simpson's method is similar, but rather than connecting two adjacent points with a line, a quadratic curve is used to connect three consecutive points. Graphical representations of these two methods are shown in Fig. 6.21. The implementations of both methods are robust to uneven trolley step sizes.

For a typical trolley run, the trapezoidal and Simpson's averaging methods produce the same value for the azimuthally averaged trolley multipoles at the sub-1 ppb level. The naive

Multipole Moment (ppm)	**Straight Average, Run 1**	**Trapezoidal Average, Run 1**	**Simpson's Average, Run 1**	**Straight Average, Run 2**	**Trapezoidal Average, Run 2**	**Simpson's Average, Run 2**
Dipole	842.592	842.545	842.545	841.643	841.613	841.613
Normal Quadrupole	-0.079	-0.078	-0.078	0.195	0.194	0.194
Skew Quadrupole	0.212	0.195	0.195	0.422	0.411	0.411
Normal Sextupole	-1.269	-1.258	-1.258	-1.363	-1.354	-1.354

Table 6.2 – Three averaging methods were tested for calculating the azimuthally averaged trolley dipole, normal quadrupole, skew quadrupole, and normal sextupole. The trapezoidal and Simpson's averaging methods produce the same results at the sub-1 ppb level, while the straight average can differ by up to 50 ppb.

straight averaging method can differ by up to 50 ppb. Analyses by different analyzers agree at the sub-5 ppb level. Azimuthally averaged trolley values for the dipole, normal quadrupole, skew quadrupole, and normal sextupole for one pair of consecutive trolley runs are given in Tab. 6.2. For run 1 analysis, Simpson's averaging is used.

An important caveat to the above discussion is that it takes approximately 80 minutes to complete a full 360° trolley run. During this time, the power supply feedback system attempts to keep the azimuthally averaged dipole stable, but it is not perfect. Additionally, it is incapable of minimizing the drift of higher order magnetic field components. An azimuthally averaged magnetic field, calculated as just discussed, includes magnetic field drift. This must be corrected for.

The first trolley run in a pair is considered first. It is not until the end of the trolley

run that all fixed probe stations are calibrated to the trolley, but magnetic field drift can be tracked locally beginning immediately after the trolley passes each station. For each station, the magnetic field drift between the time of the trolley passing and the end of the trolley run is calculated. The dipole drift is shown as a function of the order in which the trolley passes the fixed probe stations (ie, station 0 corresponds to station 54, the first station upstream of the trolley drive, while station 71 corresponds to station 55, the first fixed probe station downstream of the trolley drive) in Fig. 6.22. An average of these drifts is used to determine the overall contribution of magnetic field drift to the trolley azimuthal average. The average normal quadrupole, skew quadrupole, and normal sextupole drifts are calculated in the same way. Typical corrections for all multipole moments can be up to 50 ppb. These corrections are added to the trolley azimuthal averages, providing predictions of the azimuthally averaged magnetic field the trolley would measure, if it were able to measure the magnetic field in all 360° of the storage ring at the same time.

For the second trolley run in a pair, a similar process is used to make a drift correction to the trolley azimuthal average. However, rather than tracking the magnetic field drift between the time of trolley passing and the end of the trolley run, the magnetic field drift between the start of the trolley run and the time of the trolley passing each fixed probe station is tracked. An average of these drift values is subtracted from the trolley azimuthal average. The uncertainty on these corrections is calculated using the random walk model discussed in Sec. 6.6.3.

Fixed Probe Averaging

Trapezoidal averaging is used for calculating fixed probe azimuthal averages. As discussed in Sec. 6.4, all probes at three fixed probe stations in the inflector vacuum chamber have very poor resolution (>20 Hz). Measurements from these probes are excluded from the azimuthal average and a distance-weighted average of the magnetic field evolution predicted by the neighboring stations is used as a replacement. The trolley multipoles at these bad stations are still used for the fixed probe calibration of the weighted average of the neighbors.

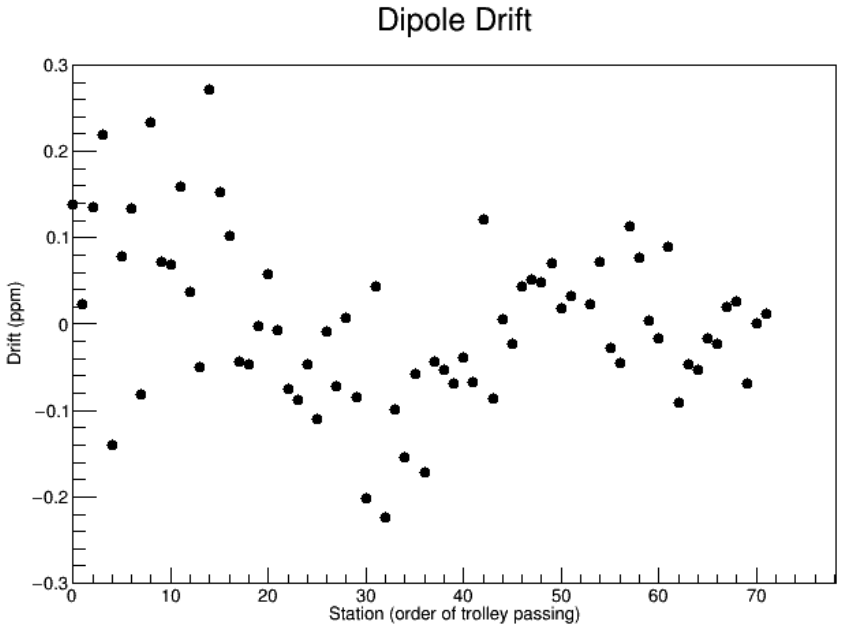

Figure 6.22 – During a trolley run, each fixed probe station is calibrated as the trolley passes underneath it. When calculating an azimuthally averaged trolley magnetic field value, the average includes the effect of magnetic field drift during the time it takes the trolley to traverse the full 360° of the magnetic storage ring. This drift is corrected for by tracking the magnetic field drift at each fixed probe station from the time of the trolley passing to the end of the trolley run. The drift of the fixed probe dipole is pictured as a function of the order in which the trolley passes the fixed probe stations in a 360° counterclockwise trolley run.

Fig. 6.23 shows the evolution of the difference of the trolley and fixed probe dipoles during a stationary trolley run with the trolley parked underneath a poor resolution fixed probe station. The difference is calculated using both the poor resolution fixed probes and using an average of the tracking from the two neighboring stations. The neighboring stations do a significantly better job at tracking the dipole evolution measured by the trolley. The same is true for the other tracked magnetic field multipole components.

After calculating the azimuthally averaged fixed probe multipoles at all times, the fixed probe averages at the times of the two trolley runs are not equal to the azimuthally averaged trolley multipole components. However, the causes of these differences are well understood. As discussed in Sec. 6.5.2, the tracking at each fixed probe station is tied to an average of 2° of trolley data. The azimuthally averaged fixed probe data should thus only be expected to be equal to an average of 144° of trolley data. To remove this difference and properly track the azimuthally averaged magnetic field, the azimuthally averaged fixed probe predictions are shifted in the same manner as was described for removing the interpolation discontinuities from individual fixed probe station predictions (Sec. 6.5.4).

The resolutions of the fixed probe azimuthal averages must be understood in order to determine how much to shift the azimuthally averaged fixed probe data at the times of the two trolley runs. This is important for minimizing the interpolation uncertainty. For example, if the resolution is 5 Hz, tying the fixed probe data to the trolley measurements using only one fixed probe measurement could lead to an error of up to 2.5 Hz (40 ppb). When calculating the azimuthally averaged fixed probe resolution, both inherent measurement fluctuations and real magnetic field drift contribute.

The Allan standard deviation gives the resolution of a signal as a function of averaging time. Fig. 6.24 shows a plot of the azimuthally averaged fixed probe dipole and a plot of the Allan standard deviation as a function of averaging time. The time of the minimum of the Allan standard deviation plot represents the averaging time for which the best resolution can be achieved, before magnetic field drift starts to become the dominant effect. Because of power supply feedback, the azimuthally averaged dipole does not drift significantly over

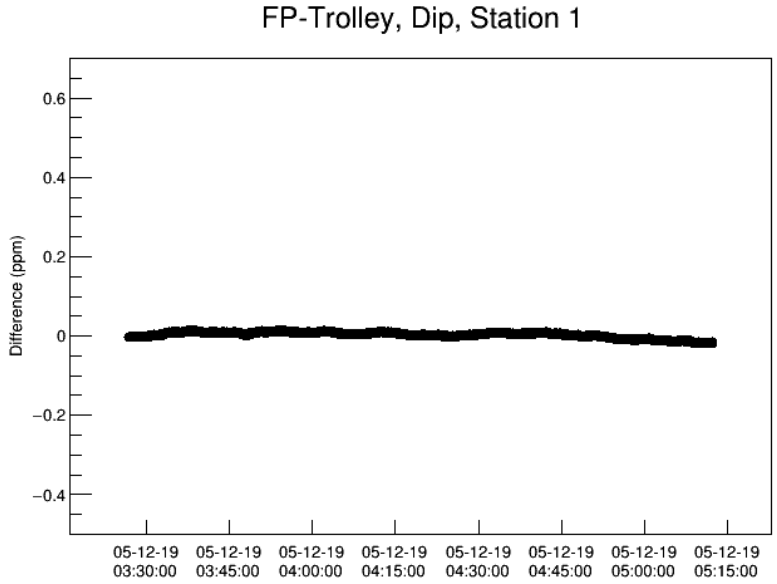

(a) Average of neighboring stations.

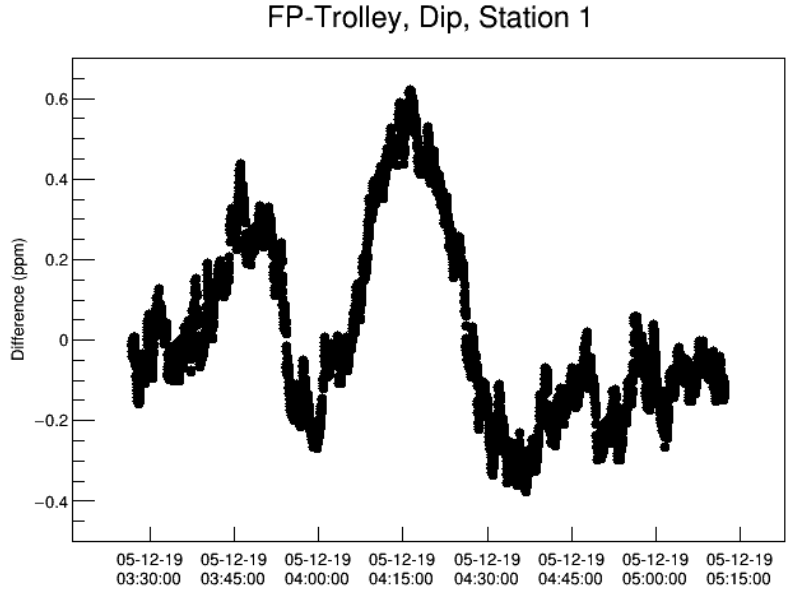

(b) Poor resolution fixed probes.

Figure 6.23 – The probes at three of the fixed probe stations in the inflector vacuum chamber have very poor resolution. Fixed probe and trolley measurement differences (for all tracked multipole moments, but pictured for the dipole) from long runs with the trolley parked stationary under these stations show that a distance-weighted average of the measurements from fixed probes at the two neighboring stations (a) tracks the magnetic field evolution measured by the trolley better than the poor resolution fixed probes (b).

short times compared with the inherent fixed probe resolution, so the ideal averaging time is approximately 1500 seconds. Using this averaging time yields an azimuthally averaged fixed probe dipole resolution of 13 ppb.

The azimuthally averaged fixed probe dipole is thus shifted, at the time of the first trolley run, by an amount equal to the difference between the azimuthally averaged trolley dipole and an average of the first 1500 seconds of fixed probe data. At the time of the second trolley run, the same process is followed using the last 1500 seconds of fixed probe data. At all times between the trolley runs, the azimuthally averaged fixed probe predictions are shifted by a temporally weighted combination of the shifts at the times of the two trolley runs. This same procedure is used to correct the predictions of the normal quadrupole, skew quadrupole, and normal sextupole, but with averaging times of 270 seconds, 680 seconds, and 2970 seconds, corresponding to resolutions of 4.2 ppb, 0.7 ppb, and 2.3 ppb respectively.

Characteristic azimuthally averaged magnetic field interpolation plots for one trolley run pair are shown in Fig. 6.25. The plots have been overlaid with orange points which show the times that are considered good by both the ω_a and ω_p data quality teams. Times corresponding to abnormal magnetic field features caused by such things as misuse of the power supply feedback system and malfunctioning hardware have been cut, as have periods where there were problems with the muon beam or storage systems (ie the accelerator complex wasn't sending muons or the quadrupoles sparked and were recovering).

Diurnal cycles are apparent in the normal quadrupole interpolation plot. The temperature in the $g-2$ experimental hall increases during the day and decreases overnight. The size of the gap between the pole pieces increases/decreases in response to the changing temperature, causing a change in the normal quadrupole magnetic field component. The power supply feedback mitigates this effect for the dipole. However, as can be inferred from the fact that Fig. 6.25a has a downwards slope as opposed to being flat, the subset of fixed probes used as input to the feedback system did not provide a perfect representation of the azimuthally averaged dipole.

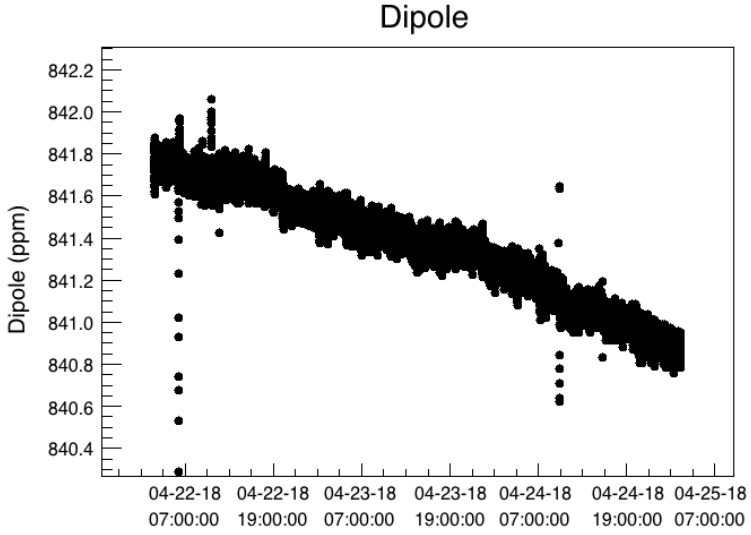

(a) Azimuthally averaged fixed probe dipole.

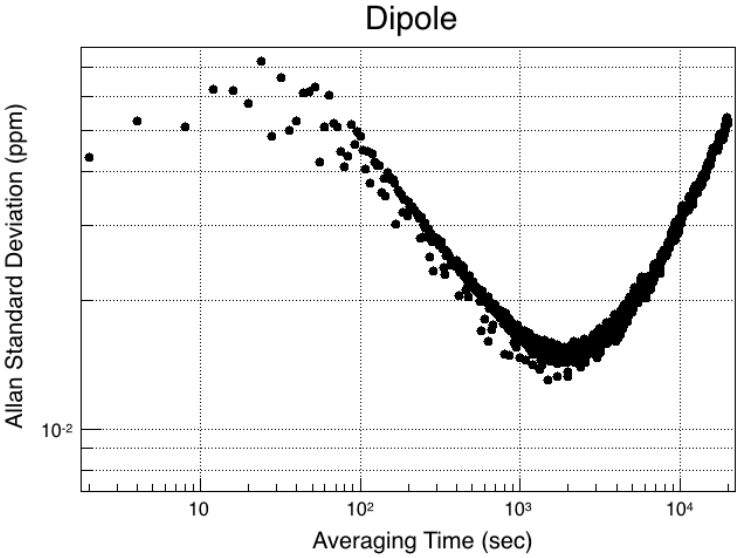

(b) Allan standard deviation.

Figure 6.24 – The Allan standard deviation is used to determine how much to shift the azimuthally average fixed probe multipoles to match the azimuthally averaged trolley multipoles. The azimuthally averaged fixed probe dipole over the course of three days between trolley runs is shown in (a), while the Allan standard deviation of the data is shown as a function of averaging time in (b).

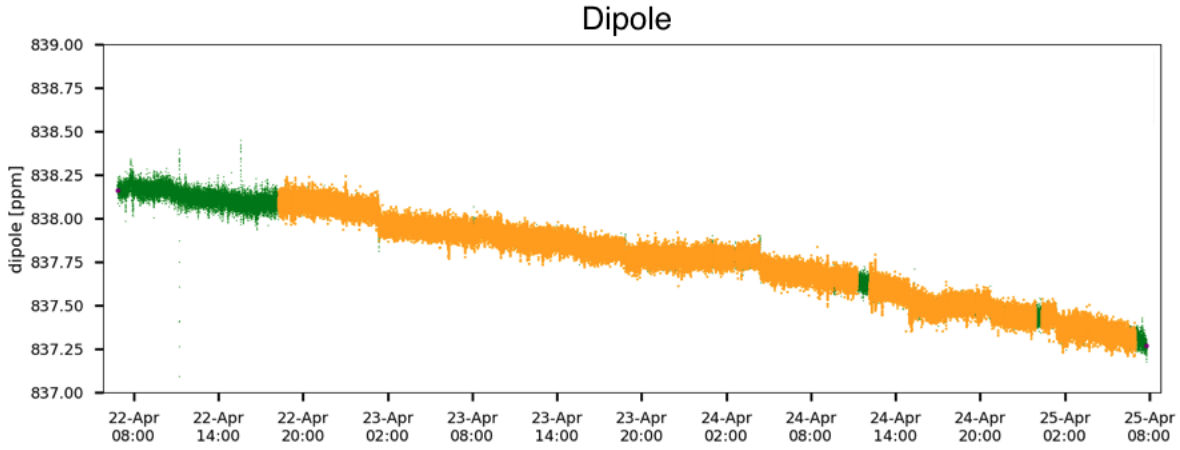

(a) Dipole.

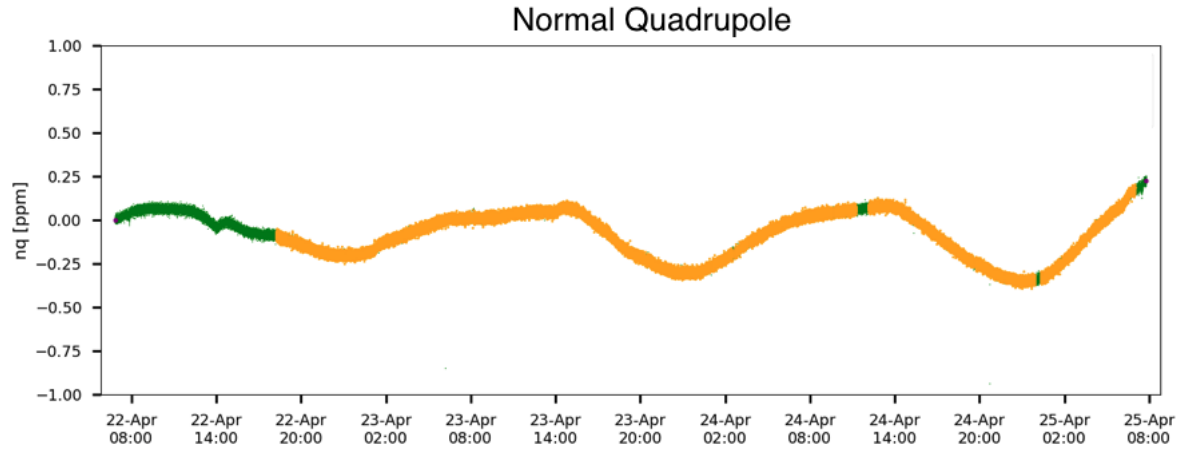

(b) Normal quadrupole.

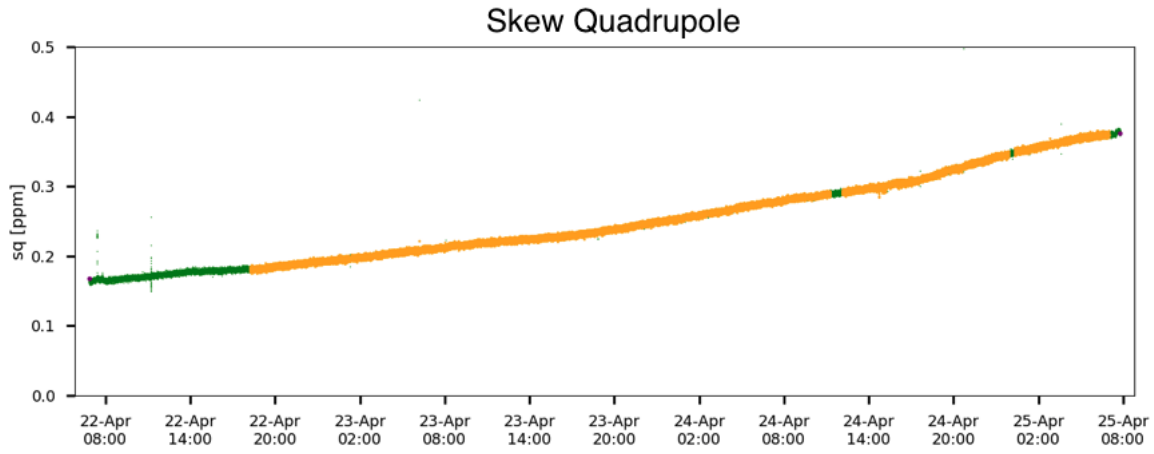

(c) Skew quadrupole.

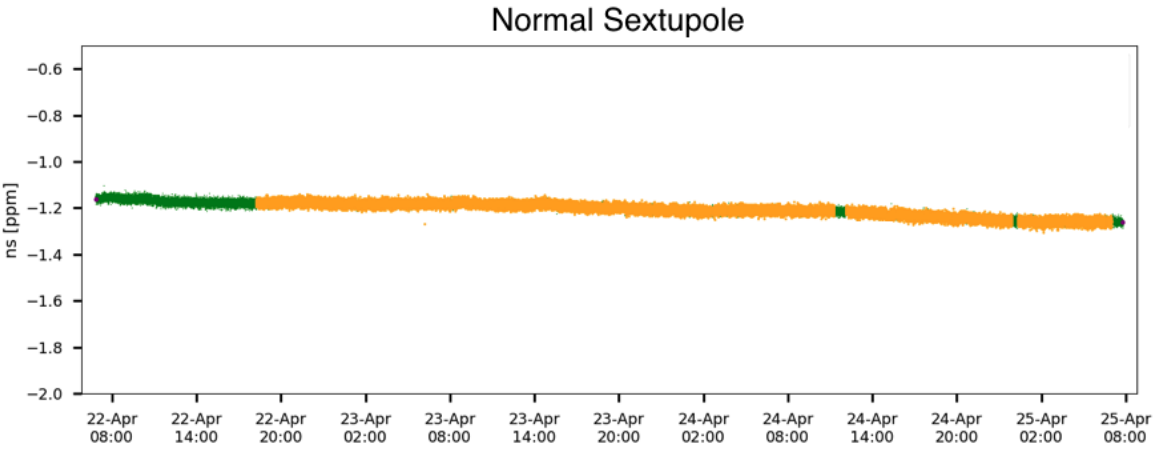

(d) Normal sextupole.

Figure 6.25 – Azimuthally averaged dipole, normal quadrupole, skew quadrupole, and normal sextupole interpolation plots for one trolley run period. Purple points represent trolley azimuthal averages, while green points are the predicted magnetic field evolution. The overlaid orange points show the times which are considered good by both the ω_a and ω_p data quality teams.

6.6 Interpolation Uncertainties

The total uncertainty associated with magnetic field interpolation gets contributions from both the interpolation process just described, as well as from effects not directly related to the interpolation process. The following subsections detail the contributions studied by team Bloch, while additional uncertainties are listed in the tables of Sec. 6.7.

6.6.1 Trolley Position Extraction

The trolley position, crucial in understanding the azimuthal variations of the magnetic field and calibrating the fixed probes to the trolley, can be determined in two ways. One method monitors the motors that control the motion of the trolley. This method's reliability is poor when the trolley is moving through an area where it experiences increased friction. Movement in such regions causes an increased force in the pulling cable. The motor encoders interpret this force as trolley motion, even when the trolley is momentarily stuck and immobile. The other method uses a barcode reader to read unique barcode markings printed on the bottoms of the vacuum chambers. This method, which is used in the Bloch interpolation analysis, is more reliable. Each barcode marking is 2 mm wide, so a conservative estimate for position uncertainty is ± 2 mm, or $\pm 0.016^{\circ}$.

A typical trolley run was used to investigate the effect of the trolley position determination on the calculation of azimuthally averaged trolley multipoles. The trolley position associated with every measurement in a 360° run was "smeared" by adding an offset drawn from Gaussian distributions of varying widths. The azimuthally averaged frequencies measured by each of the 17 trolley pNMR probes were then computed using the Simpson's averaging method. The smearing was tested 50 times for each Gaussian distribution width. Fig. 6.26 shows the mean and RMS of the resultant frequency spreads for one trolley probe. A position uncertainty of ± 2 mm leads to an uncertainty on the azimuthally averaged trolley frequency of 0.16 Hz, or 2.5 ppb.

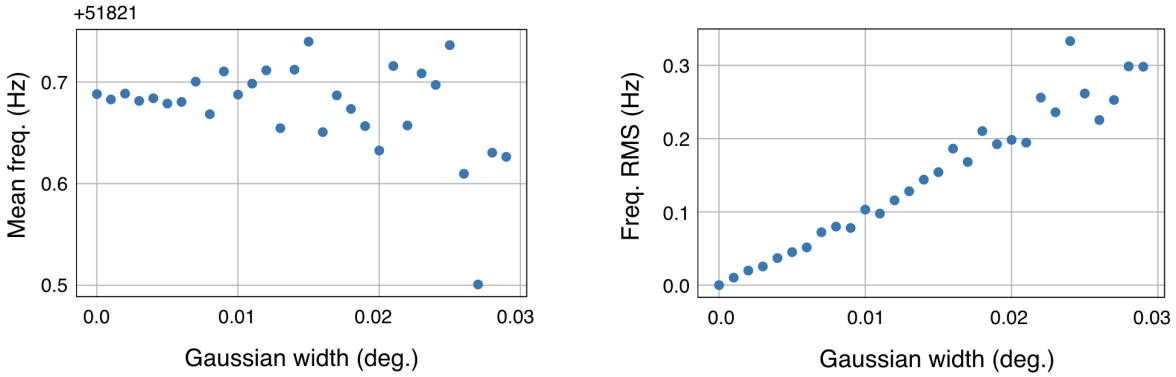

(a) Mean.

(b) RMS.

Figure 6.26 – The trolley positions associated with each measurement in a trolley run were smeared by values drawn from Gaussian distributions of varying widths to study the effect of trolley position determination on the azimuthally averaged trolley magnetic field values. For each Gaussian width, 50 trials were calculated and the mean and RMS values of the resultant frequency spreads were recorded, pictured here for one trolley probe.

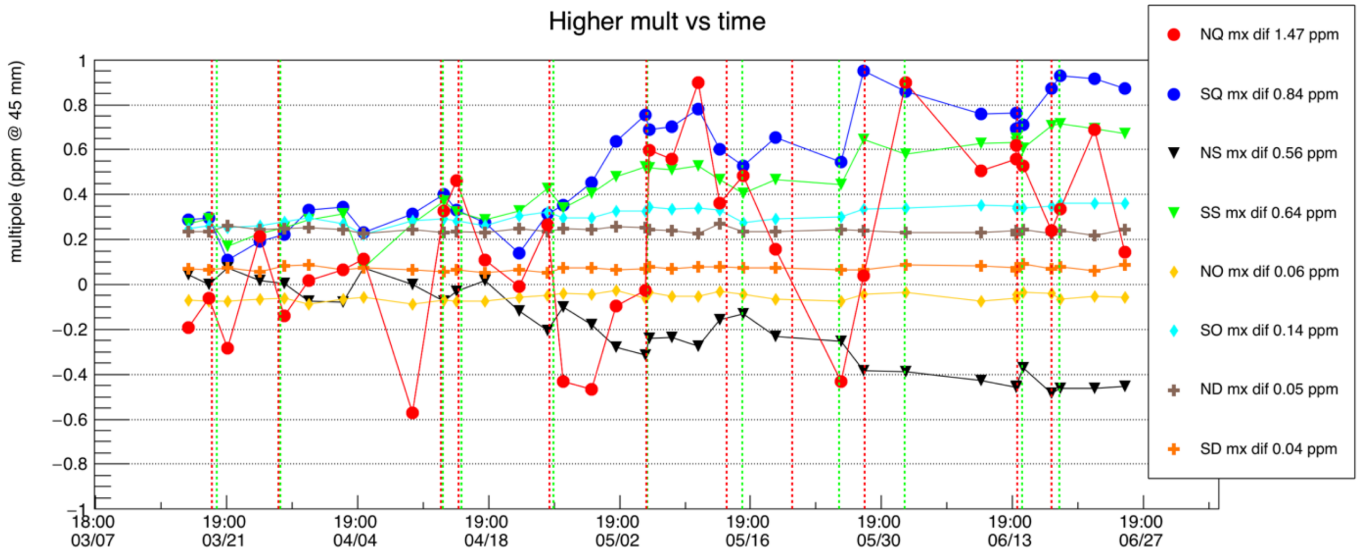

Figure 6.27 – The evolution of the azimuthally averaged trolley multipoles as a function of time during run 1 of the Fermilab $g-2$ experiment. Some multipole moments have been shifted vertically. Image credit: [100]

6.6.2 Higher Order Magnetic Field Moments

The trolley's 17 probes can resolve many more magnetic field multipole moments than the fixed probes. Fig. 6.27 shows the evolution of the azimuthally averaged trolley multipoles for all trolley runs throughout run 1 of the Fermilab $g-2$ experiment. The normal quadrupole shows the most variation, while the other multipoles show smaller, more gradual changes.

Fixed probe tracking of the evolution of the dipole, normal quadrupole, skew quadrupole, and normal sextupole has already been discussed. Tab. 6.3 lists how the azimuthally averaged trolley multipoles, through the normal duodecupole, changed between three pairs of trolley runs, each separated by approximately three days. The dipole, normal quadrupole, and skew quadrupole show the largest changes, although the normal and skew sextupole occasionally show a large change as well.

For the a_μ calculation, the magnetic field is convoluted with the muon beam distribu-

Magnetic Field Multipole Moment	**Runs 3997-3956 (ppb)**	**Runs 4181-4138 (ppb)**	**Runs 4226-4189 (ppb)**
Dipole	-932	-871	-696
Normal Quadrupole	271	58	-53
Skew Quadrupole	216	114	-11
Normal Sextupole	-96	-47	-10
Skew Sextupole	78	42	-17
Normal Octupole	-4	2	0
Skew Octupole	20	22	1
Normal Decapole	2	-7	5
Skew Decapole	14	-3	3
Normal Dodecapole	3	-15	5
Skew Dodecapole	-19	-6	2
Normal Duodecapole	-13	1	5

Table 6.3 – The change in the azimuthally averaged trolley multipoles between three pairs of trolley runs, each separated by approximately three days.

tion, as discussed in Sec. 3.7. A multipole expansion of the run 1 muon beam distribution showed that the most significant muon beam multipole components were the dipole, normal quadrupole, and normal sextupole. All other multipole moments were smaller by a factor of at least three [100].

While the fixed probe array is used to track the evolutions of the magnetic field equivalents of the most prevalent muon beam multipole components, it is also important to quantify how the higher order magnetic field multipoles could be changing. All azimuthally averaged magnetic field multipoles are known at the times of trolley runs. Between trolley runs it is assumed that the magnetic field evolution follows a smooth, pseudo-random walk, as opposed to undergoing large discrete changes, but the allowed magnetic field values at all times between successive trolley runs must be well understood. The normal decupole will be used as an example in the following discussion, but the same process is used for understanding the possible evolution of all magnetic field multipoles not tracked by the fixed probe array.

Fig. 6.28 shows the evolution of the azimuthally averaged trolley normal decupole, plotted as a function of trolley run number. This plot reveals a downwards trend of the pseudo-randomly sampled data points. In order to understand how the normal decupole could have reasonably evolved between these measurements, it is assumed that the spread in measurements that were taken reveals the reasonable spread that could be expected. To investigate this spread, the normal decupole drift per hour, shown in Fig. 6.29a, was studied. A histogram of the drift rate (Fig. 6.29b) has a mean of 0.02 ppb/hr and a width of 0.07 ppb/hr.

A random walk simulation is used to determine the reasonable normal decupole variations between two trolley runs. Starting with a trolley measurement, a step size is drawn from a Gaussian distribution every hour, representing the evolution of the normal decupole. To find the input parameters for the Gaussian distribution, the random walk simulation was run with Gaussian distributions with means of 0 ppb/hr and varying widths. 1,000,000 random walks were simulated per tested width. The difference between the starting and ending normal decupole values were recorded and histogrammed for each trial. An input Gaussian width of 0.7 ppb/hr leads to a histogram of normal decupole change per hour that matches

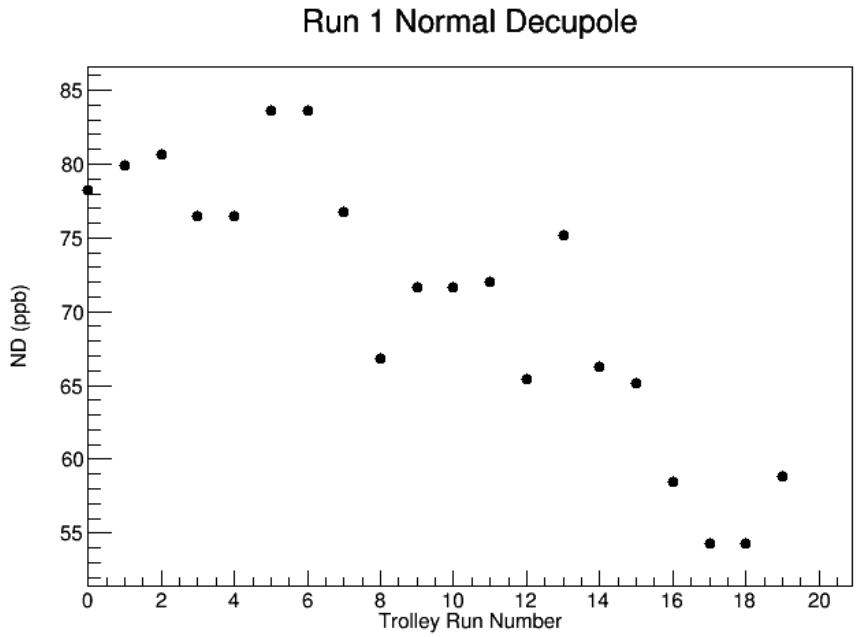

Figure 6.28 – The azimuthally averaged trolley normal decupole as a function of trolley run number.

run 1 observations. This distribution is then used to model the possible evolution of the normal decupole between any pair of trolley runs. Histograms of simulated normal decupole change and drift per hour are shown in Fig. 6.30 for a 100 hour period. The histogram of drift per hour has a mean of 0 ppb/hr and a width of 0.07 ppb/hr, matching experimental observations.

A histogram of the evolutions of the normal decupole from 1,000,000 random walk simulations is shown in Fig. 6.31. The paths are not bounded and are allowed to evolve for 100 hours. The distribution at each time slice is investigated to understand the tracking of the normal decupole at any time. The mean and RMS values are shown as a function of time from the trolley run in Fig. 6.32. To determine the normal decupole strength and associated uncertainty at any time between trolley measurements, values are read from these plots at a time equal to the temporal distance to the nearest trolley run. For a period of time bounded by two trolley runs, the uncertainties are thus symmetric in time. This same simulation is

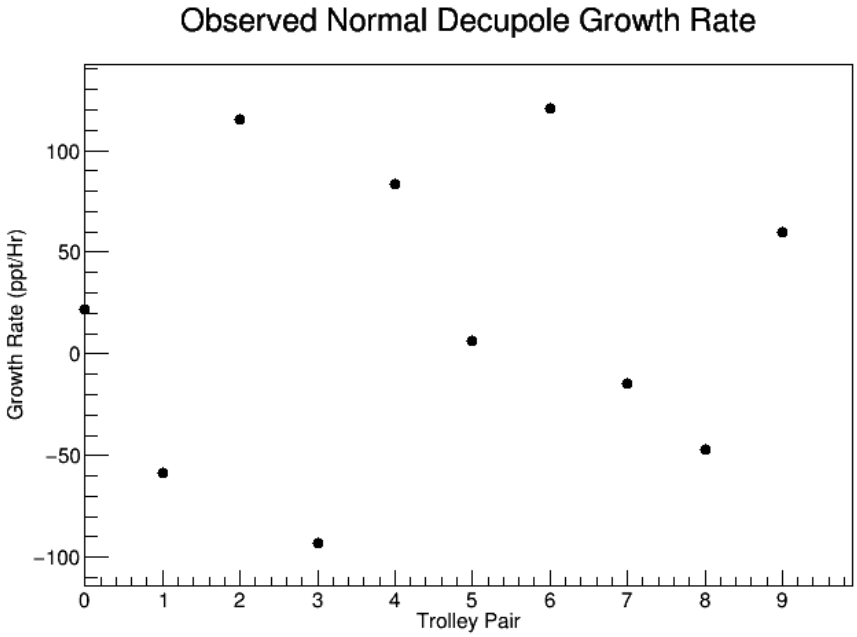

(a) Drift as a function of run number.

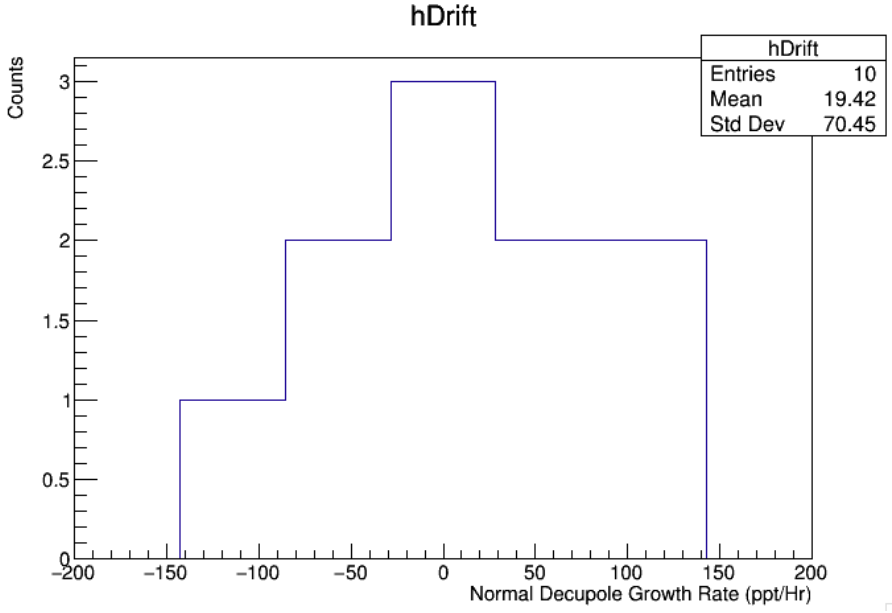

(b) Histogrammed drifts.

Figure 6.29 – Drift of the azimuthally averaged trolley normal decupole, in ppt/hr, is shown as a function of trolley pair number during run 1 in (a) and is histogrammed in (b). The drift rate is characterized as 19.42±70.45 ppt/hr.

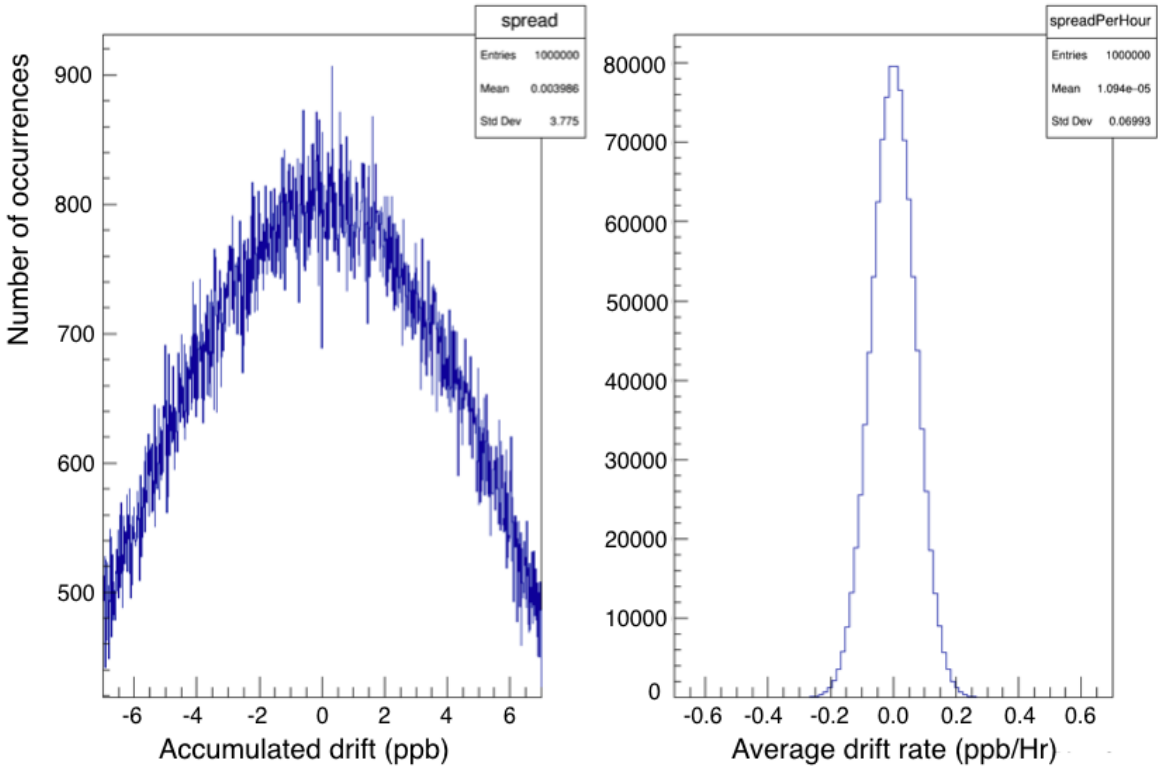

Figure 6.30 – A simulation is used to understand the possible paths that the normal decupole evolution could take between trolley runs. For each hour, the rate of change of the normal decupole is drawn from a Gaussian distribution with a mean of 0 ppb/hr and a width of 0.7 ppb/hr. This simulation was run 1,000,000 times. Histograms of the total normal decupole change over a 100 hour period (the maximum amount of time allowed between trolley runs), as well as a histogram of the change per hour, are shown. The change per hour histogram has a mean of 0 ppb/hr and a width of 0.07 ppb/hr, matching experimental observations (Fig. 6.29). Image credit: [77]

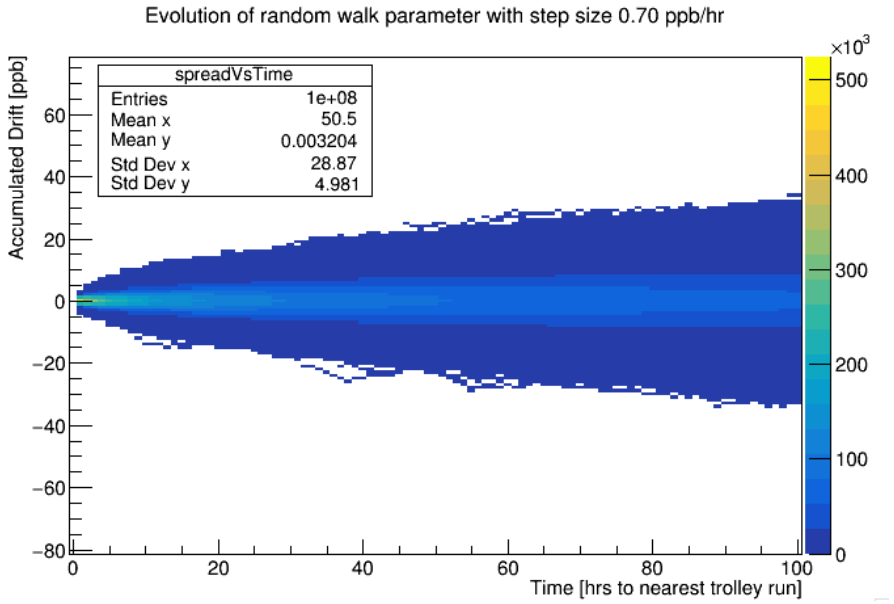

Figure 6.31 – 1,000,000 random walks were simulated to investigate the possible normal decupole evolution between trolley runs. The various paths are pictured as a function of time from the nearest trolley run. The simulation was run for 100 hours and is unbounded. Image credit: [77]

used, with different input parameters, for each magnetic field multipole component which can not be tracked by the fixed probes.

6.6.3 Uncertainty in the Dipole, Normal Quadrupole, Skew Quadrupole, and Normal Sextupole Tracking

Having developed a method for determining the evolution of the untracked magnetic field multipole components, a similar study can be used to determine how the uncertainty on the dipole, normal quadrupole, skew quadrupole, and normal sextupole tracking evolves between trolley runs. Using the same random walk method to study the dipole evolution as was presented for the normal decupole leads to a maximum uncertainty of 590 ppb for an 80 hour period bounded by two trolley runs, with this maximum occurring 40 hours into the

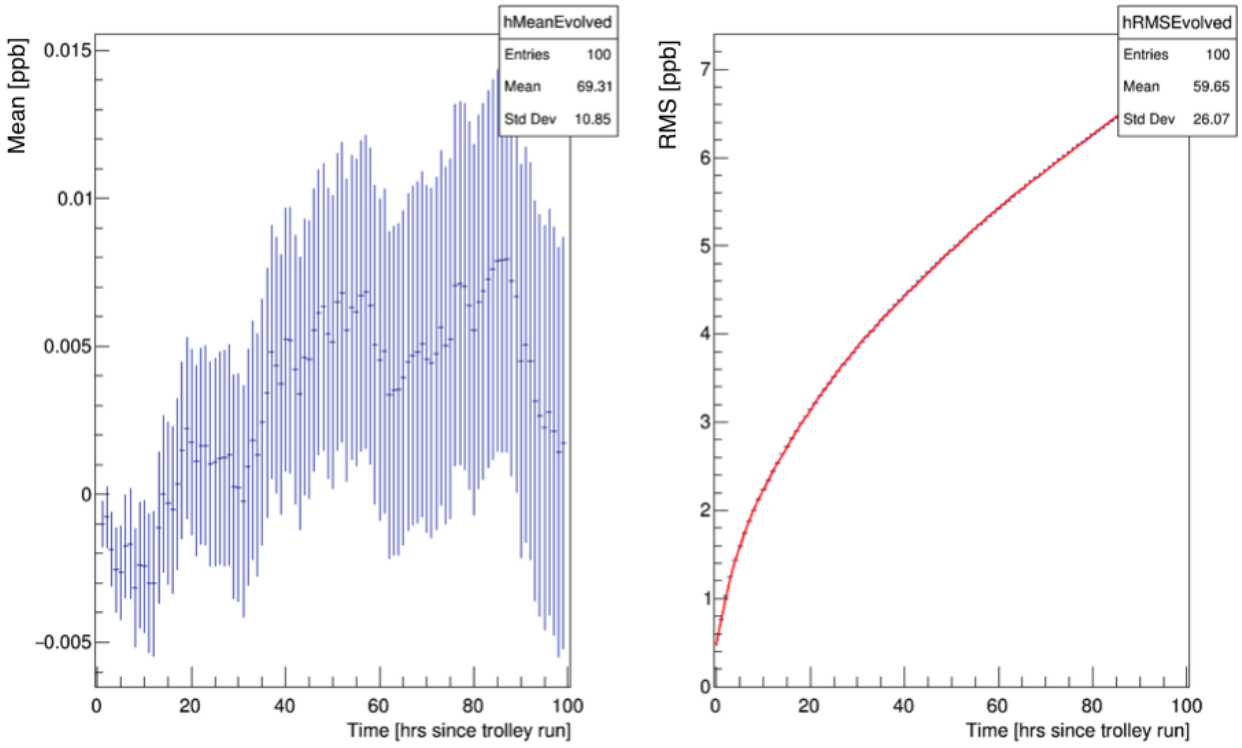

Figure 6.32 – Predictions for the normal decupole evolution and associated uncertainty between trolley runs come from looking at the mean and RMS of the possible magnetic field values at each time slice (the data shown in Fig. 6.31). The value and uncertainty at any time are evaluated from these plots at a time corresponding to the temporal distance to the most recent trolley run. Image credit: [77]

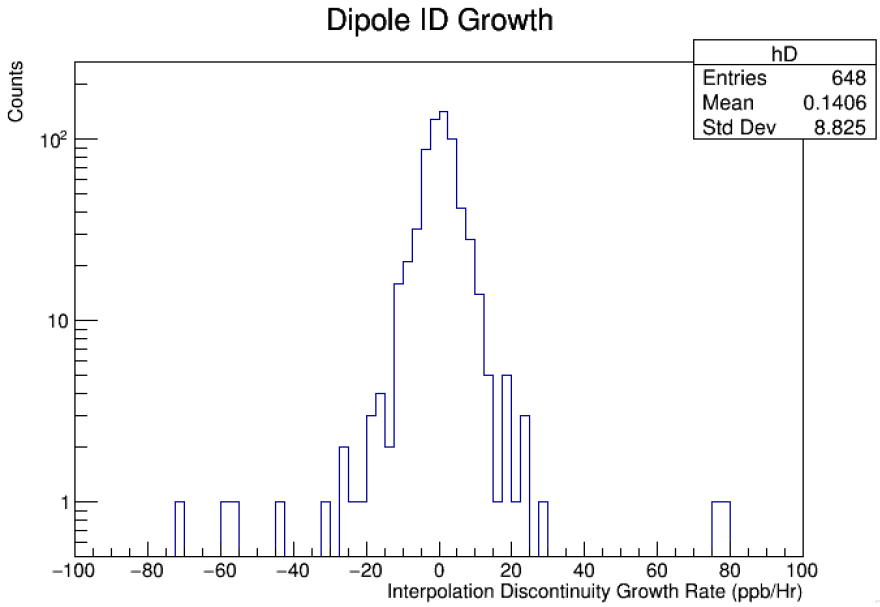

Figure 6.33 – The interpolation discontinuities from all 72 fixed probe stations are used to characterize how well the fixed probes are able to track magnetic field evolution. The dipole interpolation discontinuities from nine trolley run pairs were normalized by the time between trolley runs. A histogram of these values shows a mean interpolation discontinuity growth rate of 0.14 ppb/hr and a width of 8.825 ppb/hr.

period. However, the simulation leading to this result assumes that no information exists about the multipole evolution between trolley measurements. This is not the case for the dipole.

The interpolation discontinuities from all 72 fixed probe stations from nine pairs of trolley runs were used to study how well the fixed probes track the magnetic field evolution. Fig. 6.33 shows a histogram of the dipole interpolation discontinuities normalized by the times between trolley measurements. The distribution has a mean growth rate of 0.14 ppb/hr and a width of 8.825 ppb/hr.

Rather than tracking the evolution of the azimuthally averaged dipole, the simulation is used to track the evolution of the azimuthally averaged interpolation discontinuity. In

practice, this is achieved by drawing 72 values for interpolation discontinuity evolution from a Gaussian distribution every hour, one for each fixed probe station. The azimuthally averaged interpolation discontinuity growth is calculated as the average of these 72 values for each time step. Using a Gaussian distribution with a mean of 0.14 ppb/Hr and a width of 88.25 ppb/hr as input to the random walk simulation results in a final distribution of interpolation discontinuities, over 1,000,000 trials, with a mean of 0.14 ppb/Hr and a width of 8.825 ppb/hr, the same as observed in Fig. 6.33.

Fig. 6.34 shows the paths by which the azimuthally averaged dipole interpolation discontinuity grew in the 1,000,000 random walk simulations. Fig. 6.35 shows the mean and RMS of the distribution at every time slice, where the mean represents the correction that is applied to remove the interpolation discontinuity at the time of the second trolley run and the RMS represents the interpolation uncertainty. For an 80 hour period of time bounded by two trolley runs, the maximum dipole interpolation uncertainty, occurring 40 hours after the first trolley run, is 66 ppb. This can be compared to the 590 ppb uncertainty achieved with no knowledge of the fixed probe tracking.

The same process is used to characterize the uncertainties on the other tracked magnetic field multipole components. The normal quadrupole interpolation discontinuity growth rate is characterized as 0.431±5.054 ppb/hr, while the skew quadrupole and normal sextupole rates are characterized as -0.368±4.505 ppb/hr and 0.260±5.451 ppb/hr respectively. Gaussian distributions with widths of 50.54 ppb/hr, 45.05 ppb/hr, and 54.51 ppb/hr are used as inputs to the simulation, leading to maximum uncertainties of 38 ppb, 34 ppb, and 41 ppb respectively for the normal quadrupole, skew quadrupole, and normal sextupole for an 80 hour period between trolley runs.

6.7 Combined Magnetic Field Interpolation Uncertainties

All uncertainties associated with the team Bloch magnetic field interpolation analysis are presented in the following tables. Tab. 6.4 summarizes uncertainties associated with all magnetic field multipole components, while Tabs. 6.5, 6.6, 6.7, and 6.8 summarize uncertainties

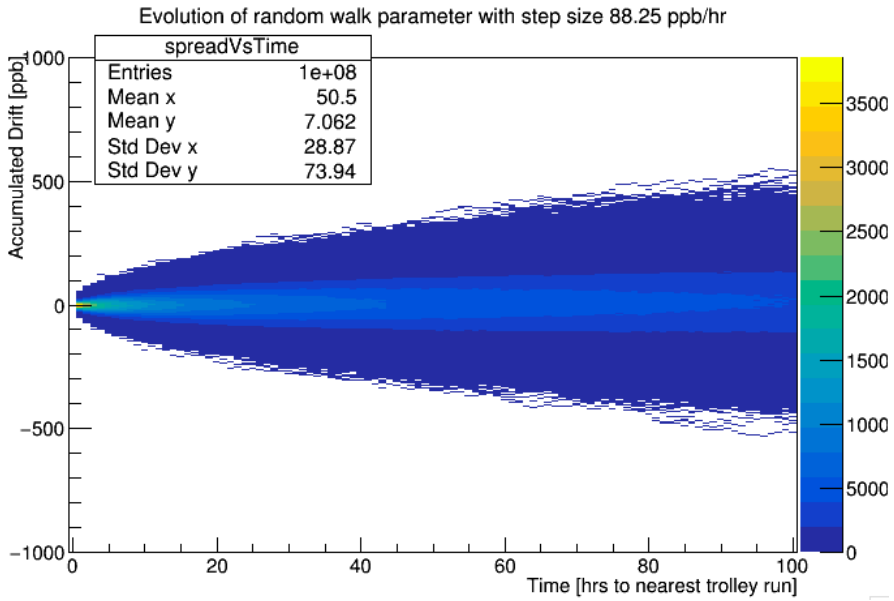

Figure 6.34 – The interpolation discontinuity is a representation of the uncertainty on the interpolation analysis, characterizing how well the fixed probes are able to track the magnetic field evolution. Using the dipole interpolation discontinuities from all 72 fixed probe stations from nine trolley run pairs as input to simulation, the evolution of the azimuthally averaged dipole interpolation discontinuity was studied. 1,000,000 paths that the evolution could take over a 100 hour period are pictured. The width of the distribution increases over time, indicating a greater uncertainty in our understanding of the actual interpolation discontinuity. Image credit: [77]

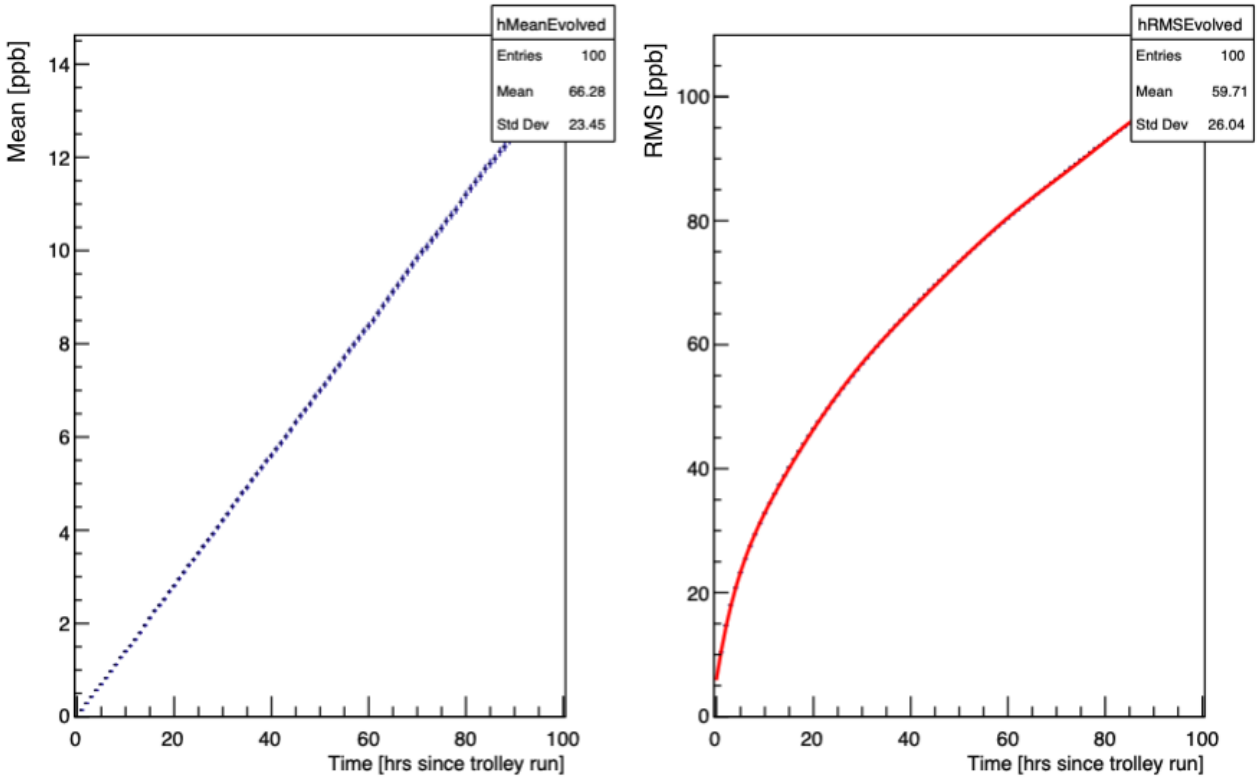

Figure 6.35 – Dipole interpolation uncertainties are based on the possible evolutions of the azimuthally averaged dipole interpolation discontinuity. The mean and RMS values of the distributions of Fig. 6.34 are plotted for every hour, showing how the azimuthally averaged dipole interpolation discontinuity and interpolation uncertainty grow as a function of temporal distance from the nearest trolley run. Image credit: [77]

associated with the dipole, normal quadrupole, skew quadrupole, and normal sextupole respectively. Effects which contribute to the total Bloch interpolation uncertainties, but which have not been studied specifically by the interpolation team, are also included with references provided.

Two of the multipole-specific uncertainties depend on the particular trolley run pair and the time between the trolley runs: the magnetic field drift correction to trolley azimuthal averages, and the general interpolation uncertainty. For the drift correction, typical values are presented. Uncertainties are calculated using the random walk model. For the interpolation uncertainty, an average period of 80 hours is assumed between trolley runs, such that the maximum uncertainty occurs 40 hours from each trolley run. However, for a given trolley run pair, the maximum uncertainty actually occurs at a time $t = T/2$ where T is the time between the trolley runs. If a data period has only one good bookending trolley run, the maximum uncertainty occurs at a time $t = T$ where T represents the length of the period.

Uncertainty Source	**Correction Value (ppb)**	**Uncertainty Value (ppb)**	**Details**
Trolley spikes (Eddy currents)	0	6	Sec. 6.4
Trolley position determination	0	2.5	Sec. 6.6.1
Trolley rail misalignment	0	16	[104]
Trolley azimuthal averaging	0	5	Sec. 6.5.5
Trolley frequency extraction	0	10	[105]
Fixed probe frequency extraction with trolley present	0	32	Sec. 6.5.3

Table 6.4 – Uncertainties associated with the Bloch fixed probe interpolation analysis that affect all magnetic field multipole moments.

Uncertainty Source	**Correction Value (ppb)**	**Uncertainty Value (ppb)**	**Details**
Trolley probe calibration	0	5.1	[63]
Magnetic field drift during trolley run	<50	8.7	Sec. 6.5.5,
Fixed probe dipole resolution	0	13	Sec. 6.5.5
Maximum dipole interpolation uncertainty	0	85	Sec. 6.6.3

Table 6.5 – Uncertainties associated with the Bloch fixed probe interpolation analysis for the dipole magnetic field component.

Uncertainty Source	**Correction Value (ppb)**	**Uncertainty Value (ppb)**	**Details**
Trolley probe calibration	0	8.3	[63]
Magnetic field drift during trolley run	<50	5.0	Sec. 6.5.5,
Fixed probe normal quadrupole resolution	0	4.2	Sec. 6.5.5
Maximum normal quadrupole interpolation uncertainty	0	64	Sec. 6.6.3

Table 6.6 – Uncertainties associated with the Bloch fixed probe interpolation analysis for the normal quadrupole magnetic field component.

Uncertainty Source	**Correction Value (ppb)**	**Uncertainty Value (ppb)**	**Details**
Trolley probe calibration	0	10.8	[63]
Magnetic field drift during trolley run	<50	4.4	Sec. 6.5.5,
Fixed probe skew quadrupole resolution	0	0.7	Sec. 6.5.5
Maximum skew quadrupole interpolation uncertainty	0	61	Sec. 6.6.3

Table 6.7 – Uncertainties associated with the Bloch fixed probe interpolation analysis for the skew quadrupole magnetic field component.

Uncertainty Source	**Correction Value (ppb)**	**Uncertainty Value (ppb)**	**Details**
Trolley probe calibration	0	10.3	[63]
Magnetic field drift during trolley run	<50	5.4	Sec. 6.5.5,
Fixed probe normal sextupole resolution	0	2.3	Sec. 6.5.5
Maixmum normal sextupole interpolation uncertainty	0	65	Sec. 6.6.3

Table 6.8 – Uncertainties associated with the Bloch fixed probe interpolation analysis for the normal sextupole magnetic field component.

Chapter 7

CONCLUSION

At the time of this dissertation (December 2019), the Fermilab muon $g-2$ experiment is beginning run 3 of data collection. During the first two running periods, datasets were collected totaling four times the statistics of the Brookhaven dataset. The progress of data collection is shown in Fig. 7.1. With ω_a and ω_p analyses both maturing, analysis of the run 1 dataset will soon be unblinded. The result will provide a value for a_μ with an uncertainty comparable to that of the Brookhaven result and will give a first glimpse at whether the long-standing discrepancy between theoretical calculation and experimental measurement of a_μ will be confirmed or resolved. Runs 3, 4, and 5 (spanning winter 2019-spring 2022) aim to record enough muon decays to make the combined Fermilab dataset 20 times larger than that of the Brookhaven experiment, imperative in reaching the 140 ppb uncertainty goal.

This dissertation has detailed the determination of the magnetic field for data collected during the first running period of the Fermilab $g-2$ experiment. The author has made significant contributions to both the magnetic field measurement hardware and the magnetic field analysis. On the hardware side, the author contributed to the design and construction of the pulsed nuclear magnetic resonance probes used for measuring the magnetic field magnitude. At Fermilab, the author was a core member of the small team that made the magnetic field in the muon storage region two times more homogeneous than was achieved in the Brookhaven experiment. She also measured the radial and longitudinal magnetic field components at over 100 azimuthal locations in the storage ring using a Hall probe apparatus she co-designed. On the analysis side, she has developed algorithms for tracking the evolution of the magnetic field at the sub-100 ppb level, meeting the run 1 interpolation uncertainty goal and paving the way for future analyses to reach the final 30 ppb magnetic field interpolation uncertainty

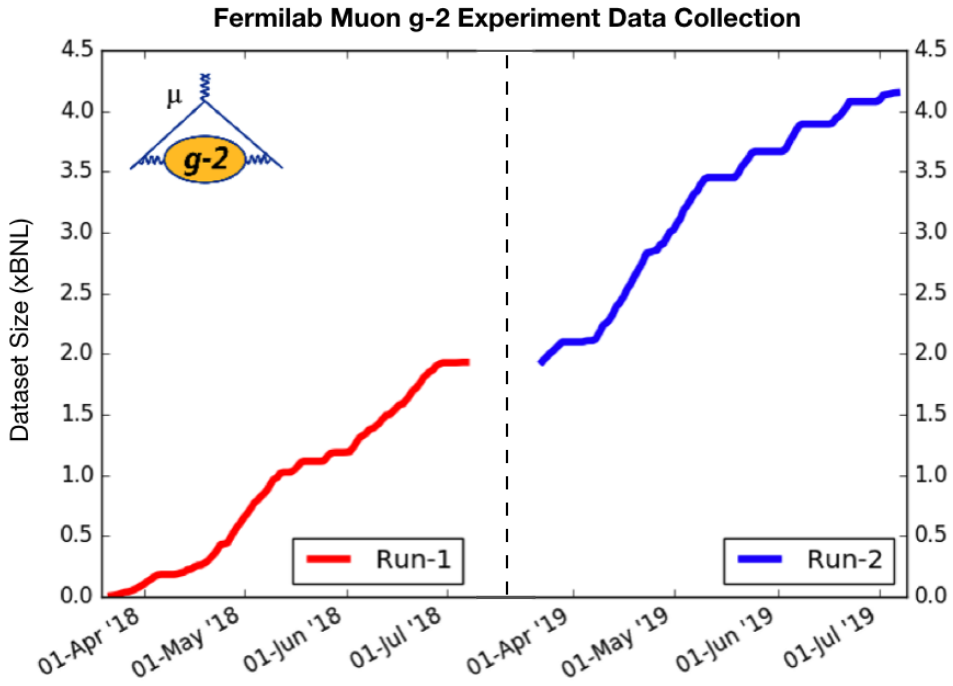

Figure 7.1 – Over the course of two running periods, the Fermilab muon $g-2$ experiment collected a dataset four times larger than the complete Brookhaven dataset. With three more running periods expected, the experiment aims to collect a total dataset in excess of 20x that of the Brookhaven experiment in order to reach the 140 ppb uncertainty goal. Image credit: [106]

goal.

The largest suspected contributor to the current magnetic field interpolation uncertainty is evolving higher order magnetic field multipoles which the fixed probes can not track, but which affect the calculation of fixed probe multipoles. The leading cause of the changes of these multipoles is the changing experimental hall temperature. During run 1, the temperature in the $g-2$ experimental hall increased by almost 6 °C. In summer 2018, before beginning run 2, the storage ring magnet was wrapped in fiberglass insulation to help minimize temperature variations of the magnet steel. A hall cooling system was installed in fall 2019, with the goal that the experimental hall temperature will be stable at the 1 °C level for run 3 and all future running periods.

There also exist improvements which could be made to the Bloch interpolation analysis to further reduce uncertainties and gain a better understanding of the magnetic field evolution. In the current scheme, azimuthal variations of the radial and longitudinal magnetic field components have been ignored. There are discussions underway about the possibility of building a "radial field trolley" which would operate inside of the vacuum chambers to measure the radial magnetic field component at all azimuthal locations. Should such a trolley be built, a three-dimensional multipole expansion could be used to better describe the magnetic field in the muon storage region. Additionally, a study is ongoing to understand the magnetic field evolution at all azimuthal locations, as opposed to just at the azimuthal fixed probe station positions. The method involves using the magnetic field changes at fixed probe locations to evolve 360° trolley measurements in time. The results of this study could be used to construct more accurate fixed probe azimuthal averages.

Overall, the determination of the magnetic field in the Fermilab muon $g-2$ experiment is in good condition, with all run 1 uncertainty goals having been met. Future improvements are expected to reduce all uncertainties to their final goals, which are listed in Tab. 3.1. Run 1 results are expected to be published in early 2020, with the results of later running periods published in subsequent years.

BIBLIOGRAPHY

[1] John David Jackson. *Classical electrodynamics*. John Wiley & Sons, Inc., 1999.

[2] J. J. Sakurai. *Modern quantum mechanics*. Addison-Wesley Publishing Company, 1994.

[3] Peter J. Mohr, David B. Newell, and Barry N. Taylor. CODATA Recommended Values of the Fundamental Physical Constants: 2014. *Journal of Physical and Chemical Reference Data*, 45, 2016.

[4] G.E. Uhlenbeck and S. Goudsmit. *Naturwissenschaften*, 47, 1925.

[5] G.E. Uhlenbeck and S. Goudsmit. Spinning Electrons and the Structure of Spectra. *Nature*, 117, 1926.

[6] P. A. M. Dirac. *The quantum theory of the electron*. 1928.

[7] B. Lee. Roberts and William J. Marciano. *Lepton dipole moments*. World Scientific, 2010.

[8] D. Hanneke, S. Fogwell Hoogerheide, and G. Gabrielse. Cavity control of a single-electron quantum cyclotron: Measuring the electron magnetic moment. *Phys. Rev. A*, 83, 2011.

[9] G.W. Bennett et al. Final report of the E821 muon anomalous magnetic moment measurement at BNL. *Phys. Rev. D*, 73, Apr 2006.

[10] $g-2$ collaboration: J. Grange et al. Muon $(g-2)$ technical design report. 2015.

[11] M. Tanabashi et al. Review of Particle Physics. *Phys. Rev. D*, 98, Aug 2018.

[12] Jonathan L. Rosner and Sheldon Stone. Leptonic decays of charged pseudoscalar mesons - 2012. 2012.

[13] James P. Miller, Eduardo de Rafael, and B. Lee Roberts. Muon $g-2$: Review of Theory and Experiment. *Rept. Prog. Phys.*, 70, 2007.

[14] E.J. Konopinski. The experimental clarification of the laws of β-radioactivity. *Ann. Rev. Nucl. Sci.*, 9, 1959.

[15] F.J.M. Farley and Y.K. Semertzidis. The 47 years of muon $g-2$. *Progress in Particle and Nuclear Physics*, 52, March 2004.

[16] Sergei Redin. *Preparation and first result of BNL experiment E821 "A New Precision Measurement of the Muon ($g-2$) value"*. PhD thesis, Yale University, May 1999.

[17] Alexander Keshavarzi, Daisuke Nomura, and Thomas Teubner. Muon $g-2$ and $\alpha(M_Z^2)$: a new data-based analysis. *Phys. Rev.*, D97, 2018.

[18] Alexander Keshavarzi, Daisuke Nomura, and Thomas Teubner. The $g-2$ of charged leptons, $\alpha(M_Z^2)$ and the hyperfine splitting of muonium. 2019.

[19] Tatsumi Aoyama, Masashi Hayakawa, Toichiro Kinoshita, and Makiko Nio. Complete Tenth-Order QED Contribution to the Muon $g-2$. *Phys. Rev. Lett.*, 109, 2012.

[20] Tatsumi Aoyama, Toichiro Kinoshita, and Makiko Nio. Revised and Improved Value of the QED Tenth-Order Electron Anomalous Magnetic Moment. *Phys. Rev.*, D97, 2018.

[21] Rym Bouchendira et al. New determination of the fine structure constant and test of the quantum electrodynamicsl. *Phys. Rev. Lett.*, 106, 2011.

[22] Richard H. Parker, Chenghui Yu, Weicheng Zhong, Brian Estey, and Holger Muller. Measurement of the fine-structure constant as a test of the Standard Model. *Science*, 360, 2018.

[23] C. Gnendiger, D. Stockinger, and H. Stockinger-Kim. $(g-2)_\mu$ after the Higgs boson mass measurement. *Phys. Rev.*, D88, 2013.

[24] A. Czarnecki, W. Marciano, and A. Vainshtein. Refinements in electroweak contributions to the muon anomalous magnetic moment. *Phys. Rev.*, D67, 2006.

[25] M. Davier, A. Hoecker, B. Malaescu, and Z. Zhang. A new evaluation of the hadronic vacuum polarisation contributions to the muon anomalous magnetic moment and to $\alpha(m_z^2)$, 2019.

[26] F. Jegerlehner and A. Nyffeler. The muon $g-2$. *Physics Reports*, 477, 2009.

[27] Nils Asmussen, Antoine Gerardin, Andreas Nyffeler, and Harvey B. Meyer. Hadronic light-by-light scattering in the anomalous magnetic moment of the muon. *SciPost Physics Proceedings*, 2019.

[28] Joaquim Prades, Eduardo de Rafael, and Arkady Vainshtein. The Hadronic Light-by-Light Scattering Contribution to the Muon and Electron Anomalous Magnetic Moments. *Adv. Ser. Direct. High Energy Phys.*, 20, 2009.

[29] Fred Jegerlehner. Leading-order hadronic contribution to the electron and muon $g-2$. *EPJ Web Conf.*, 118, 2016.

[30] Yutaro Sato. Muon $g-2$/EDM experiment at J-PARC. *PoS*, KMI2017, 2017.

[31] Andrzej Czarnecki and William J. Marciano. The Muon Anomalous Magnetic Moment: A Harbinger for "New Physics". *Phys. Rev.*, D64, 2001.

[32] Kaoru Hagiwara, Kai Ma, and Satyanarayan Mukhopadhyay. Closing in on the chargino contribution to the muon $g-2$ in the MSSM: current LHC constraints. *Phys. Rev.*, D97, 2018.

[33] M. Ablikim et al. Dark Photon Search in the Mass Range Between 1.5 and 3.4 GeV/c^2. *Phys. Lett.*, B774, 2017.

[34] J.R. Batley et al. Search for the dark photon in π^0 decays. *Phys. Lett.*, B746, 2015.

[35] NA64 Collaboration. Search for invisible decays of sub-GeV dark photons in missing-energy events at the CERN SPS. *Phys. Rev. Lett.*, 118, 2017.

[36] BaBar Collaboration. Search for Invisible Decays of a Dark Photon Produced in e^+e^- Collisions at BaBar. *Phys. Rev. Lett.*, 119, 2017.

[37] David Smith and Neal Weiner. Inelastic Dark Matter. *Phys. Rev. D*, 64, 2001.

[38] Gopolang Mohlabeng. Revisiting the Dark Photon Explanation of the Muon Anomalous Magnetic Moment. *Phys. Rev. D*, 99, 2019.

[39] Yu-Dai Tsai, Patrick deNiverville, and Ming Xiong Liu. The High-Energy Frontier of the Intensity Frontier: Closing the Dark Photon, Inelastic Dark Matter, and Muon $g-2$ Windows. 2019.

[40] Kari Swanson. Private Communication.

[41] G. T. Danby et al. The Brookhaven muon storage ring magnet. *Nucl. Instrum. Meth.*, A457, 2001.

[42] Nathan S. Froemming. *Optimization of Muon Injection and Storage in the Fermilab $g-2$ Experiment: From Simulation to Reality*. PhD thesis, University of Washington, 2018.

[43] A. Yamamoto et al. The superconducting inflector for the BNL $g-2$ experiment. *Nucl. Instrum. Meth.*, A491, 2002.

[44] SeungCheon Kim. Development of the fast muon kicker for the muon $g-2$ experiment at Fermilab. *Nuclear and Particle Physics Proceedings*, 2016.

[45] Y. K. Semertzidis et al. The Brookhaven muon $(g-2)$ storage ring high voltage quadrupoles. *Nucl. Instrum. Meth.*, A503, 2003.

[46] Saskia Charity. *Beam profile measurements using the straw tracking detectors at the Fermilab muon $g-2$ experiment, and a study of their sensitivity to a muon electric dipole moment*. PhD thesis, University of Liverpool, 2018.

[47] K. S. Khaw et al. Performance of the Muon $g-2$ calorimeter and readout systems measured with test beam data. *Nucl. Instrum. Meth.*, A945, 2019.

[48] Jason Hempstead. Private Communication.

[49] Aaron Fienberg. *Measuring the Precession Frequency in the E989 Muon $g-2$ Experiment*. PhD thesis, University of Washington, 2019.

[50] D. Flay and D. Kawall. The High-Precision Calibration NMR Magnetometer for the Muon $g-2$ Experiment at Fermilab. 2019.

[51] Midhat Farooq. *Absolute Magnetometry with ^{3}He: Cross Calibration with Protons in Water*. PhD thesis, University of Michigan, 2019.

[52] F. Bloch, W. W. Hansen, and M. Packard. The nuclear induction experiment. *Phys. Rev.*, 70, Oct 1946.

[53] Anatole Abragam. *The principles of nuclear magnetism*. University Press, 1999.

[54] Edwin Becker. A brief history of nuclear magnetic resonance. *Analytical Chemistry*, 65, 1993.

[55] L. D. Landau and E. M. Lifshitz. *Statistical physics, Vol. 5.* Butterworth-Heinemann, 1980.

[56] F. Bloch. Nuclear induction. *Phys. Rev.*, 70, Oct 1946.

[57] R. Prigl et al. A high precision magnetometer based on pulsed NMR. *Nuclear Instruments & Methods in Physics Research, Section A*, 374, 1996.

[58] Matthias Smith. *Developing the Precision Magnetic Field for the E989 Muon $g-2$ Experiment.* PhD thesis, University of Washington, 2017.

[59] Michael Feldman. *Hilbert Transform Applications in Mechanical Vibration.* John Wiley & Sons, 2011.

[60] J. L. Flowers, P. W. Franks, and B. W. Petley. Correcting high precision pulsed NMR flux density measurements for asymmetries in the lineshape. *IEEE Transactions on Instrumentation and Measurement*, 44, 1995.

[61] Martin Fertl. Private Communication.

[62] Martin Fertl and Rachel Osofsky. Assembly instructions for a pNMR probe. 2015.

[63] David Flay. Private Communication.

[64] Xiang Fei, V.W. Hughes, and Ralf Prigl. Precision measurement of the magnetic field in terms of the free-proton NMR frequency. *Nuclear Instruments & Methods in Physics Research, Section A*, 394, 1997.

[65] Y. Neronov and N. Seregin. Determination of the difference in shielding by protons in water and hydrogen and an estimate of the absolute shielding by protons in water. *Metrologia*, 51, Feb. 2014.

[66] William D. Phillips, William E. Cooke, and Daniel Kleppner. Magnetic Moment of the Proton in H_2O in Bohr Magnetons. *Metrologia*, 13, Oct. 1977.

[67] B. H. Blott and G. J. Daniell. The determination of magnetic moments of extended samples in a SQUID magnetometer. *Measurement Science and Technology*, 4, Apr. 1993.

[68] D. Flay. Magnetic Field Calibration Analysis for the Muon $g-2$ Experiment at Fermilab. 2019.

[69] D. Flay. Calibrating the Field. $g-2$ Physics Week, 2018.

[70] M. Fertl, R. Osofsky, and H. E. Swanson. FNAL E989 $g-2$ note 70: A multipole expansion of the magnetic field in three dimensions. *FNAL E989 Internal Notes*, 2015.

[71] Geoffrey T. Bodwin, Hee Sok Chung, and Jose Repond. Implementation of Maxwell's equations in the reconstruction of the magnetic field in the $g-2$ storage ring. *JINST*, 14, 2019.

[72] G. T. Danby et al. The Brookhaven muon storage ring magnet. *Nucl. Instrum. Meth.*, A457, 2001.

[73] G. T. Danby and J. W. Jackson. Ultraprecise Magnet Design and Shimming Studies. *BNL E821 Internal Notes*, 1987.

[74] Kim Woodle. Status of shimming studies using the BNL test magnet. *BNL E821 Internal Notes*, 1990.

[75] G. T. Danby and J. W. Jackson. Shimming Techniques for the Ultraprecise Muon $g-2$ Storage Ring at the AGS. *BNL E821 Internal Notes*, 1993.

[76] Frank Krienen. Some Remarks on the Shimming of the Muon $g-2$ Magnet. *BNL E821 Internal Notes*, 1987.

[77] Brendan Kiburg. Private Communication.

[78] Capacitec Inc. Short form manual for Capacitec 4000 series electronics, probes, and accessories. `http://www.sparkycnc.com/pdfs/CPT.pdf`. Accessed: April 29, 2019.

[79] Fredericks Company. 16-bit RS-232/Analog Signal Conditioner. `https://www.frederickscompany.com/wp-content/uploads/2017/02/1-6200-012_ds.pdf`. Accessed: April 29, 2019.

[80] Frank Krienen, Dinesh Loomba, and Wuzheng Meng. New method and proposal for quadrupole compensation of the muon $g-2$ storage ring. *BNL E821 Internal Notes*, 1990.

[81] Frank Krienen. The folly of the wedge. *BNL E821 Internal Notes*, 1991.

[82] Alex Grossmann. *Magnetic field determination in a superferric storage ring for a precise measurement of the muon magnetic anomaly.* PhD thesis, Heidelberg University, July 1998.

[83] David Kawall. Private Communication.

[84] F. Krienen. Pole face windings. *BNL E821 Internal Notes*, 1985.

[85] W. Morse and K. Woodle. Some Calculations Regarding Current Shims. *BNL E821 Internal Notes*, 1990.

[86] W. Morse. More Calculations Regarding Current Shims. *BNL E821 Internal Notes*, 1991.

[87] Michael Fischer. Pole Face Current Shims. *BNL E821 Internal Notes*, 1992.

[88] P. Hammond. Electric and magnetic images. *Proceedings of the IEE - Part C: Monographs*, 107, Sept. 1960.

[89] J. P. Blewett, M. H. Blewett, W. H. Moore, and L. W. Smith. Pole Face Windings. Part I - Design. *Review of Scientific Instruments*, 24, Sep 1953.

[90] S. I. Redin et al. Radial magnetic field measurements with a Hall probe device in the muon $(g-2)$ storage ring magnet at BNL. *Nucl. Instrum. Meth.*, A473, 2001.

[91] S. Sanfilippo. Hall probes: physics and application to magnetometry. In *Proceedings, 2009 CAS-CERN Accelerator School: Specialised course on Magnets: Bruges, Belgium, June 16 - 25, 2009*, 2011.

[92] Tokihiro Ikeda et al. High-precision magnetic field mapping with a three-dimensional Hall probe for a T-violation experiment in $K_{\mu 3}$ decay. *Nuclear Instruments and Methods in Physics Research Section A: Accelerators, Spectrometers, Detectors and Associated Equipment*, 401, 1997.

[93] M. Fertl. E989 Note 185: Hardware requirements for the Hall probe measurements, March 29, 2016.

[94] Asensor Technology AB. Linear high Precision Analog Hall Sensor HE244. `https://www.asensor.eu/onewebmedia/Datasheet-HE244X.pdf`. Accessed: April 29, 2019.

[95] Proforma. Hex Adjusters, 3/16"-100 Ultra Fine. `https://www.thorlabs.com/newgrouppage9.cfm?objectgroup_id=1205`. Accessed: May 22, 2019.

[96] J. Grange. E989 Note 57: Shift in ω_p due to couplings between longitudinal and transverse magnetic field inhomogeneities (distortion of the closed orbit), 2015.

[97] Rachel Osofsky, Jason Bono, Saskia Charity, Jimin George, Brendan Kiburg, and Erik Swanson. Bloch Interpolation Analysis. 2019.

[98] Alec Tewsley-Booth, Tim Chupp, Joe Grange, and Simon Corrodi. Matrix Method for Trolley-Fixed Probe Interpolation. 2019.

[99] Jason Bono. Private Communication.

[100] Joe Grange. Private Communication.

[101] Simon Corrodi. Private Communication.

[102] Jimin George. Private Communication.

[103] Noah Samuelson. Private Communication.

[104] Bingzhi Li. Private Communication.

[105] Ran Hong. Muon $g-2$ NMR Frequency Extraction. *FNAL E989 Internal Notes*, 2019.

[106] Mark Lancaster. Private Communication.